Doctoral theses at NTNU, 2023:402

Monica Pazos Urrea

Exploring metal-metal and metal-support interactions in Pt-based catalysts for aqueous phase reforming

Doctoral thesis

NTNU
Norwegian University of Science and Technology
Thesis for the Degree of
Philosophiae Doctor
Faculty of Natural Sciences
Department of Chemical Engineering

NTNU
Norwegian University of
Science and Technology

Monica Pazos Urrea

Exploring metal-metal and metal-support interactions in Pt-based catalysts for aqueous phase reforming

Thesis for the Degree of Philosophiae Doctor

Trondheim, December 2023

Norwegian University of Science and Technology
Faculty of Natural Sciences
Department of Chemical Engineering

NTNU
Norwegian University of
Science and Technology

NTNU
Norwegian University of Science and Technology

Thesis for the Degree of Philosophiae Doctor

Faculty of Natural Sciences
Department of Chemical Engineering

ISBN 978-82-326-7502-9 (printed ver.)
ISBN 978-82-326-7501-2 (electronic ver.)
ISSN 1503-8181 (printed ver.)
ISSN 2703-8084 (online ver.)

Doctoral theses at NTNU, 2023:402

Printed by NTNU Grafisk senter

Abstract

The extensive use of fossil fuels is widely recognized as one of the main contributors to global warming. Therefore, finding alternative and sustainable energy sources/carriers is a relevant area of research to address the environmental crisis. Processing biomass—derived feedstocks for producing sustainable fuels and chemicals is a promising source to exploit for production of carbon-neutral fuels.

Aqueous phase reforming (APR) is introduced as a process to valorize aqueous mixtures of oxygenates to produce hydrogen and carbon dioxide at mild temperatures and pressures close to the bubble point of the feed. Challenges associated with the catalyst stability and selectivity and the common use of noble metals limit the use of aqueous phase reforming in an industrial context. The research in this thesis aims to reduce the use of platinum by promoting the catalytic activity of Pt-based catalysts supported on carbon nanofibers. The addition of a second metal and the introduction of heteroatoms to the carbon surface is explored to maximize the interaction of the components in the system to obtain a stable and selective APR catalyst.

An initial screening of catalysts based on Pt and Ni raised interest in examining more closely the bimetallic system Pt-Mn in APR of ethylene glycol. The catalytic APR performance of supported nitrogen-doped carbon nanofibers was evaluated in batch and continuous flow setups, observing a promising activity towards H_2 production. Utilizing characterization techniques such as X-ray photoelectron spectroscopy (XPS), identification of charge transfer from platinum to the nitrogen groups and to manganese revealed metal-metal and metal-support interactions that enhance the catalytic activity. It was observed that a small amount of Mn was sufficient to improve the performance of the catalyst after detecting significant Mn leaching, but without any adverse effects on H_2 production.

The local environment of Pt plays a crucial role in the catalytic activity and selectivity on APR. Therefore, modifications of the carbon support by heteroatom doping were investigated to find correlations between the properties of the catalyst and the activity, selectivity, and stability in APR. Carbon dopants, including O, N, S, P and B, were chosen for their capacity to introduce acidic or basic properties to the carbon support. *In-situ* X-ray absorption spectroscopy (XAS) was employed in combination with multivariate curve resolution alternating least squares analysis (MCR-ALS), to identify the platinum species formed during APR and observing the differences in the catalyst activity. The N-doped Pt-

based catalyst yields high metal dispersion and further promotion of the water-gas shift reaction (WGS). The addition of boron and phosphorus dopants resulted in lower Pt dispersion leading to lower activity. Additionally, phosphorous and sulfur-containing functionalization introduced more acidic groups on the carbon surface, promoting the formation of liquid by-products such as alcohols and organic acids.

Furthermore, a bimetallic PtNi catalyst supported on TiO_2 with low noble metal content (Pt<1%wt) exhibited high activity and stability when subjected to the demanding hydrothermal conditions of aqueous phase reforming. The metal-metal interactions and favorable support characteristics promoting the WGS reaction led to a promising catalyst for APR of ethylene glycol. Additionally, a simplified kinetic model based on the liquid phase concentration of hydrogen and ethylene glycol captures the trend of hydrogen production rate in a semi-continuous setup at 215°C.

The results yield encouraging indications for developing and improving catalysts for APR of water streams containing oxygenates by tuning the electronic properties of Pt. This can be achieved by promoting metal-metal and metal support interactions by adding a second metal or heteroatoms to the catalytic system.

Acknowledgements

I want to express my deepest gratitude to everyone who accompanied, guided, and contributed to the completion of this work over the past few years.

First, I am immensely thankful to my main supervisor, Professor Magnus Rønning, for giving me the opportunity to work on an exciting doctoral topic. Your patience, constructive feedback, and dedication to my development as a researcher allowed me to dive into the catalysis world able to enjoy and overcome the challenges within. Thank you for always keeping your door open and being a huge support even in the most stressful times at ESRF.

Thank you to my co-supervisor, Professor De Chen, for the invaluable discussions that guided my work during demanding phases in the project and for sharing my passion for carbon nanofibers.

I would like to express my gratitude to Dr. Felix Herold for his crucial involvement in the progress of this project and for his research-oriented vision toward carbon materials that opened my field to appealing materials. Additionally, thank you for all the time dedicated to XPS and STEM, which have significantly contributed to this project, and for your helpful research advice.

Thanks to the master student Simon Meilinger who has made valuable contributions to this work with his hard work, creativity, and challenging questions.

Thank you to all the ESRs and BIKE partners for the academic encounters throughout the project, the interesting discussion in beautiful cities across Europe, and the shared educational journey that straightened our friendship. Especially thanks to the institutions that welcomed me as part of their own during my secondments at the Karlsruhe Institute of Technology and Johnson Matthey.

In addition, thanks to the engineering staff in the catalysis group, in particular Estelle, for your enormous help in ensuring I had everything available and functional to keep my project running. You not only provide me with a safe environment in the lab to obtain meaningful data in my research but, as a close friend, make sure to motivate me through the difficult times.

Acknowledgements

Thanks to the workshop staff Ketil and Marius for their constant services and significant advice in upgrading/modifying the experimental rig.

I would like to express my gratitude to all the professors in the catalysis group for encouraging thought-provoking discussions within the group meetings. The excellent atmosphere and dynamics in the research group encourage me to continue every day with my research. It has been an adventure to be part of the 'catalysis family'; I appreciate all the scientific and social events that we shared. All the lab cooperation ensured that everyone was at least surviving the experiments, I would try to name a few: Youri, Tina, Felix, Petter, Kishore, Dumitrita, Ask, Ainara, Oscar, Wei, Zoe, Katarzyna, Björn, Martina, Samuel… thank you. Albert, for the time we shared at the office, thank you for your friendship.

Thanks to Jithin Gopakumar, my 'partner in crime,' you not only made my days more exciting and interesting but also involved me in challenging discussions with fruitful outcomes for developing my experiments. Besides the undoubted support under our endless nights at the beamline. Thank you for being my friend.

Last but not least, I would like to thank my family: my parents, and my brother for their love, encouragement, and invaluable support. Your belief in my abilities has given me the confidence to pursue my dreams, and for that, I am eternally thankful. Without you, I would never have come this far.

Publications associated with this research

Papers:

I. Pazos Urrea, M., Herold, F., Chen, D. & Rønning, M. Nitrogen-containing carbon nanofibers as supports for bimetallic Pt-Mn catalysts in aqueous phase reforming of ethylene glycol. *Catal. Today* **418**, 114066 (2023).

II. Pazos Urrea, M., Meilinger, S, Herold, F., Gopakumar, J., Tusini, E., De Giacinto, A., Zimina, A., Chen, D. , Grunwaldt, J.-D., Rønning, M. Aqueous phase reforming over platinum catalysts on doped carbon supports: Exploring platinum-heteroatom interactions. . *Manuscript in preparation.*

III. Pazos Urrea, M., Duran Martin, J., Bennett, S., Chen, D. & Rønning, M. Bimetallic interactions stabilizing Pt-Ni/TiO2 catalysts in aqueous reforming of ethylene glycol. *Manuscript in preparation.*

Other contributions:

I. Rosmini, C., Pazos Urrea, M., Tusini, E., Indris, S., Kovacheva, D., Karashanova, D., Zimina, A., Grunwaldt, J.-D., Rønning, M., Dimitrov, M., Popova, M. Nickel and Ni_xSn_y intermetallic compounds supported on Ce-Zr mixed-oxides for aqueous phase reforming of ethylene glycol: Influence of the pH and the active phase on the reaction pathways and products. *Applied Catalysis B: Environmental (submitted).*

II. Pazos Urrea, M., Rønning, M., Carbon-supported bimetallic catalysts in sustainable fuel production, in *Frontiers of Nanoscience, Elsevier: Invited contribution submitted to Bimetallic Nanoparticle Catalysts – Science and Applications of Multicomponent Metal Nano Catalysts (2024)*

Presentations:

I. Pazos Urrea, M., Herold, F., Chen, D., Rønning, M. (2022) Aqueous-phase reforming of ethylene glycol over carbon nanofiber-supported catalysts. CSIC, Instituto de Carboquimica 9th International Symposium on Carbon for Catalysis, CarboCat–IX , Zaragoza, Spain. 2022-06-28 - 2022-06-30. *Oral presentation*

II. Pazos Urrea, M., Meilinger, S, Herold, F., Gopakumar, J., Tusini, E., De Giacinto, A., Casapu, M., Zimina, A., Chen, D. , Grunwaldt, J.-D., Rønning, M. (2023) Aqueous-phase reforming of ethylene glycol over platinum-based catalysts supported on functionalized carbon nanofibers. 15th European congress on catalysis, Prague, Czech Republic. 2023-08-27–2023-09-01. *Oral presentation*.

Author contributions

The author has had an active role in all the stages of this thesis. All the experimental work was conducted by the author except for:

- Synthesis of MVS catalyst Pt-Mn on carbon Vulcan series was performed at the National Research Council of Italy by Xuan Trung Nguyen.
- Synthesis of Ni-Sn catalyst supported on mixed oxides Ce-Zr was performed at the Bulgarian Academy of Sciences by Consolato Rosmini.
- Synthesis of PtNi catalyst supported on TiO_2, including temperature programmed reduction, X-ray photoelectron spectroscopy, and transmission electron microscopy characterization, was performed at Johnson Matthey by Jonatan Duran Martin, Riho Green, and Gregory Goodlet.
- Transmission electron microscopy for the carbon-based catalyst was performed by Trung Dung Tran at Johnson Matthey.
- X-ray photoelectron spectroscopy and scanning transmission electron microscopy were conducted by Felix Herold.
- Multivariate curve resolution alternating least squares analysis (MCR-ALS) on the X-ray absorption spectroscopy data was performed by Jithin Gopakumar.
- Sample preparation, initial characterization, and batch testing of the series of Pt-based catalysts in heteroatom-doped carbon nanofibers was conducted by Simon Meilinger.

Table of contents

List of tables

List of figures

List of abbreviations

GHG	Greenhouse gas
IEA	International Energy Agency
MSCA	Marie Skłodowska-Curie Actions
EU	European Union
CCUS	Carbon capture, utilization and storage
PGM	Platinum group metals
APR	Aqueous phase reforming
WGS	Water gas shift reaction
TOC	Total organic carbon
CNF	Carbon nanofiber
OMC	Ordered mesoporous carbon
AC	Activated carbon
CVD	Chemical vapor deposition
GAHD	Gasification-assisted heteroatom-doping method
TOF	Turnover frequency
IWI	Incipient wetness impregnation
TAM	Template-assisted method
FSP	Flame spray Pyrolysis
XRD	X-ray diffraction
XPS	X-ray photoelectron spectroscopy
XAS	X-ray absorption spectroscopy
TEM	Transmission electron microscopy
SR	Steam reforming
AEMWE	Anion exchange membrane water electrolysis

Chapter 1: Introduction

1.1 Environmental challenges

Since the Industrial Revolution in the 18th century, the global consumption of fossil fuels has risen alongside the gross domestic product (GDP), representing around 80% of the total energy usage for decades, with oil and coal having shares close to 28% and natural gas 25% in recent years [1,2]. The global CO_2 emissions from energy combustion and industrial processes reached a value of 36.3 gigatons (Gt) in 2021, representing a 6% increase compared to 2020, driven by a 5.9% growth in the global economy [3]. In 2022, CO_2 emissions reached a new high of 36.8 Gt, increasing by 0.9%. However, emissions increase remained below the 3.2% GDP growth, marking a decoupling of the shared trend of emissions and economic growth observed in the last decades [4].

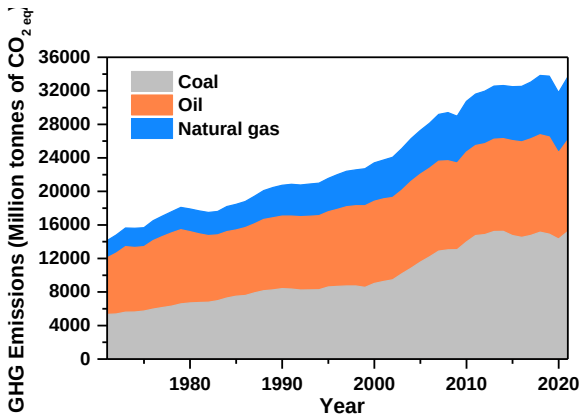

Figure 1-1. Total green house gases emissions from fuel combustion from 1971 to 2021. Adapted from [4]

According to the International Energy Agency (IEA), natural gas emissions decreased by 1.6% due to gas supply disruptions caused by the Russian invasion of Ukraine in 2022. This resulted in a significant European consumption reduction of 12.5%. In contrast, coal emissions increased by 1.6% and reached a value of 15.5 Gt, while oil emissions rose by 2.1% to 11.2 Gt in 2022 (Figure 1-1) [4]. It is estimated that around 50% of the increase in oil emissions can be traced back to transportation, as air travel is gradually resurging from its pandemic-related decrease. On the other hand, a considerable portion of coal

emissions were linked to electricity and heat production resulting from the recent extreme weather conditions.

Due to the significant emission of greenhouse gases associated with the extensive fossil fuel usage, people worldwide are experiencing the consequences of climate change, with extreme weather events becoming more frequent and severe. Hence, countries across the globe have recognized the importance of addressing climate change through actions such as making climate-friendly policies, creating social awareness, implementing sustainable urban planning, shifting from a linear to circular economy, and adopting alternative technologies to reduce greenhouse emissions [5,6].

At the 2021 United Nations Climate Change Conference (COP26), new reinforced commitments were made driving further actions and long-term strategies to move away from coal power, protect and restore ecosystems, reduce greenhouse gas emissions, and accelerate the transition to electric vehicles. In this context, to achieve the target set out in the Paris Agreement of limiting global warming to 1.5°C, a transition towards a low-carbon energy system is necessary, which indicates a substantial reduction in the overall trade of fossil fuels accompanied by a rise in the trade of alternative energy sources and vectors such as biomass and low-carbon hydrogen [2].

As outlined in the European Commission's hydrogen strategy published in 2020, there are plans to implement widespread utilization of hydrogen across challenging industries to decarbonize, starting in 2030. The European Union aims to promote the development of clean and renewable hydrogen, aligning with the EU's long-term goal of achieving climate neutrality [7].

1.2 Hydrogen production

Hydrogen has the potential to contribute to energy security by substituting fossil fuels in end-use applications, shifting hydrogen production to renewable sources, and serving as a clean energy carrier for storing renewable energy [8]. Hydrogen counts with the highest gravimetric energy density, standing at 120 MJ/kg, despite having a relatively low energy density per unit volume (2.36 MJ/L for liquid hydrogen) as compared with other liquid fuels such as ethanol (22 MJ/L), propane (23 MJ/L) and gasoline (32 MJ/L) [9]. Hence, renewable hydrogen can serve as a bridge between renewable energy resources and the modernization of energy supply, transportation, and industry due to its high gravimetric energy density, high conversion efficiency and the potential for storage [10]. Hydrogen produced through industrial processes has various applications in sectors such as

ammonia production, petrochemical refining, iron and steel industry, food processing, power plant cooling for electricity applications, and semiconductor manufacturing [11].

In 2021, global hydrogen production reached 94 million tons (Mt H_2), including natural gas without carbon capture, utilization, and storage (CCUS) as the primary production source, constituting 62% of the total. Another 18% of the hydrogen production was obtained as a by-product of naphtha reforming at refineries, with subsequent utilization in other refinery processes such as hydrocracking and desulfurization. 19% of the total production is attributed to coal-based hydrogen production. Only a small fraction of hydrogen production, approximately 0.7% (1Mt), came from fossil fuels with CCUS and from electricity via water electrolysis (35kt H_2) [8]. Still, the amount of hydrogen generated through water electrolysis, experienced nearly a 20% rise compared to 2020.

Considering the policies and measurements governments implement worldwide, the IEA projects that the demand for hydrogen could reach 115 Mt by 2030 [8]. These forecasts also suggest a rise in hydrogen consumption among emerging users, such as biofuels, which would require increased production capacity in the coming years. Hydrogen production can utilize a diverse range of resources, employing different feedstocks, pathways, and technologies, including fossil fuels and renewable energy resources. Conventional methods for producing hydrogen include reforming of hydrocarbons, gasification, pyrolysis, biomass conversion, and water splitting achieved through electrolysis or photocatalysis [12].

Utilizing biomass for hydrogen production facilitates an increase in production volume, diversifying the source of hydrogen and mitigating greenhouse gas emissions, demonstrating that the CO_2 obtained from biomass-derived hydrogen processes is used during biomass development, and thus closing the natural cycle [13]. Approximately 4.6 billion tons of lignocellulosic agricultural waste are produced annually with only 25% being utilized. Additionally, around 7 billion tons are generated from grass and forested areas, designated for energy production [14]. Thus, the abundance and low cost of biomass render it as a compelling option for utilization in the energy context.

Various technologies are being developed for hydrogen production using lignocellulosic biomass, including thermochemical processes, biological transformations, and electrochemically assisted production. Gasification, thermal liquefaction, and pyrolysis are widely used thermochemical processes that offer higher overall efficiency than biochemical methods, estimated at 52% [15]. These thermochemical routes are designed to facilitate cracking reactions, breaking down biomass molecules into lighter polymers

and a gaseous streams containing hydrogen, carbon monoxide, methane, nitrogen, and carbon dioxide [13].

The main stages in the biomass gasification process are presented in Figure 1-2, including drying, pyrolysis, combustion, and reduction. These technologies generate both liquid and gaseous co-products, such as pyrolysis oils or gases containing hydrogen that can be further processed through steam reforming and the water-gas shift reaction to produce additional hydrogen [16]. Furthermore, biochar, a solid by-product, can be used to improve soil fertility by altering the physical and chemical properties of the soil [17].

Furthermore, the exploitation of these lignocellulosic materials yields water-soluble fractions containing a variety of oxygenated compounds such as carboxylic acids, alcohols, ketones, aromatics, and sugars that can be further exploited for the production of hydrogen [19]. The economic viability and industrialization of the technologies used for biomass conversions relies on the ability to efficiently utilize these streams, which generally exhibit an organic content ranging from 2 g/L to 100 g/L [20].

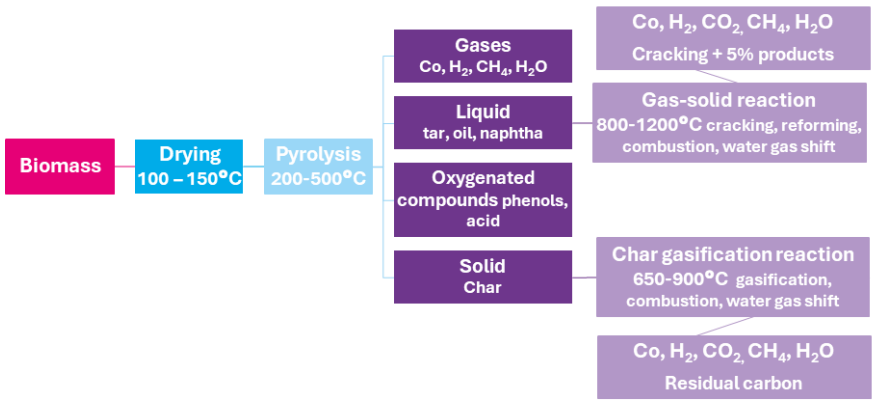

Figure 1-2. Stages and product distribution of pyrolysis and gasification of biomass [18].

Supercritical water reforming [21] or catalytic upgrading of carboxylic acids [22] have been suggested as solutions to deal with the aqueous fractions obtained from bio-oil production, to convert these carbon containing streams into valuable compounds. Aqueous phase reforming (APR) emerge as a promising technology to transform these oxygenated compounds into hydrogen and carbon dioxide at milder temperatures, typically between 220-270°C [23]. APR shows interesting features related to the use of liquid water as reaction medium, such as compatibility with high water content

feedstocks and reduced energy consumption, which is typically high in processes requiring higher temperatures and vaporization of the feedstock [24]. By using APR, the organic content in the aqueous streams can be reduced while also obtaining valuable products, aiding to manage the waste generated during bio-oil production and provide a sustainable solution to upgrade these streams, as presented in Figure 1-3 [19].

Despite its potential, aqueous phase reforming technology has not yet achieved industrial-scale application and remains an alternative validated mainly at laboratory scale [25]. Zoppi *et al.* [26] studied the feasibility of using APR in the water effluent from a Fisher-Tropsch synthesis pilot plant, observing full conversion of most molecules in the aqueous solutions with high hydrogen selectivity, reducing the chemical oxygen demand of the mixture by up to 90% by running the reaction at 270°C for 2 hours.

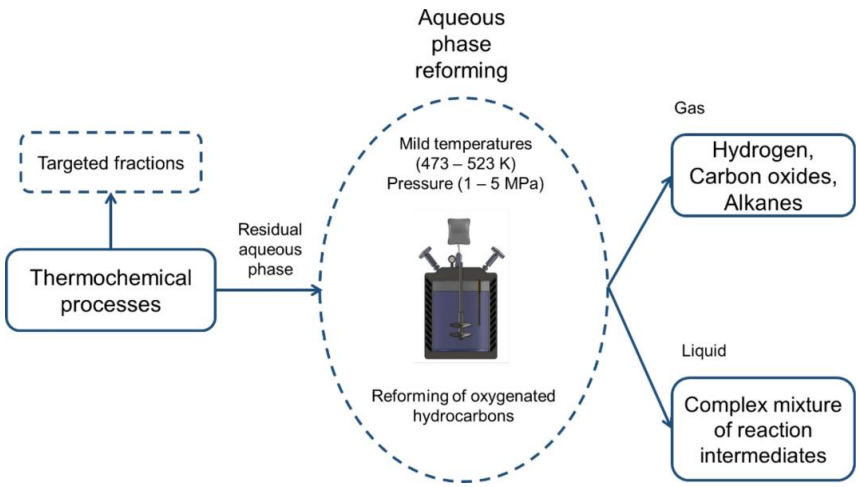

Figure 1-3. Aqueous phase reforming of oxygenated hydrocarbons in the resiudal aqueous phase obtained from thermochemical processes [25]

Regardless of the high variability of the feedstock containing low molecular weight C1-C4 primary alcohols along with their corresponding carboxylic acid and secondary alcohols such as 2-propanol, no deactivation phenomena were observed during the reaction, suggesting promising application of APR for the valorization of wastewater streams containing light oxygenates [26]. Hence, with the appropriate adjustment of the process parameters, it is possible to obtain renewable hydrogen as the main product in APR.

1.3 Valorization of wastewater streams

In the pursuit of sustainable processes, circular economy emerges a crucial strategy to maximize the value of products and raw materials by using waste as a resource in an alternative process to minimize waste generation [27]. Wastewater streams containing high loads of organic compounds are generated in relatively large volumes in the food industry, including sugar refineries, industrial processing of agricultural products, cheese manufacture and even in the brewery industry.

It is widely estimated that in the brewery industry, close to 10 liters of water are used for every liter of beer, associated with processes such as bottle washing, tank cleaning, filtering, and fermentation. In general, this wastewater must be treated or partially treated before it can be discharged into waterways or municipal sewer systems [28]. Similarly, in the fruit juice industry, 10 liters of wastewater is produced per liter of juice. Large fluctuations in the organic load, pH and salinity are observed in the water effluents due to the seasonal characteristics of this particular field, making conventional biological treatments challenging before disposal [29].

In the cheese-making process a large amount of cheese whey is generated, estimated to yield 5 million tons of this effluent a year, containing sugars, organic acids, fats, and proteins. Hence, this by-product must receive appropriate treatment to be discharged [30]. On the other hand, in the agricultural sector, large quantities of starch-rich wastewater from processing rice, potatoes and cassava are obtained. As an example, in Thailand 7L of wastewater are produced by one kilogram of fresh cassava for a total production of 18 million tons of cassava per year [31]. This field generates an effluent with high content of high molecular weight organic polymers, where the starch can be hydrolyzed into smaller sugars followed by biological treatments to produce carbohydrates, organic acids, and subsequently hydrogen [32].

In recent years, researchers have investigated the potential of valorizing these wastewater streams by employing primarily noble metal-based catalysts via aqueous phase reforming, resulting in a significant reduction in the organic matter of these water effluents [25,29,33–35]. Oliveira *et al.* [33] studied the conversion of starch in agricultural wastewater from potato, rice, and cassava using bimetallic catalysts supported on carbon (PtRu, PtPd, PtRe, and PtRh). They reported high total organic carbon (TOC) removal values between 45-85%, with the highest H_2 yield from the rice, processing wastewater of 28.5 mmol H_2/g TOC. Additionally, they emphasized the relevance of the starch

concentration and impact of other components present in the feed on the catalytic activity, suggesting that wastewater streams with high protein content should be pre-treated to achieve good catalyst performance with high stability.

Oliveira *et al.* [34] also explored the treatment of effluents from the fish-canning industry using aqueous phase reforming over a Pt/C catalyst. The results showed that APR, combined with adsorption on the carbon support and hydrothermal carbonization, removed 45-60% of the TOC from the wastewater streams. However, the high chloride, acetate, and phosphate concentrations in the effluents had a negative impact on gas production and could potentially lead to catalyst deactivation. Despite this, the study achieved 18% gas generation towards valuable products such as hydrogen and alkanes.

Although encouraging outcomes have been achieved in laboratory-scale experiments, introducing real waste feedstocks brings new challenges related to the type of wastewater that needs to be treated. If the feed contains high concentrations of proteins or phosphates, it may affect the performance of the catalyst, which could potentially limit the application of APR on such streams. In this sense, to integrate APR into biomass-based processes to generate value from their waste streams, a characterization of the product to be used is essential to determine if the effluent needs to be pretreated before APR to achieve high H_2 yields. Additionally, effective catalyst development promoting the right pathways in the reaction scheme is crucial for the feasibility of the process. The development of the catalyst, the reactor design, and proper process integration are still steppingstones for scaling up APR to industrial applications.

1.4 Resource sustainability of platinum

As part of the group VIII elements in the periodic table, platinum is widely recognized for exceptional catalytic activity in various reactions. It is particularly suitable for hydrogenation reactions, ammonia oxidation, and catalytic conversion to purify harmful emissions from vehicle exhausts due to its oxidation resistance and its effectiveness in petroleum reforming [36].

Global production of platinum is primarily centered in southern Africa, the region with the most extensive known reserves of platinum group metals (PGM) and nearly exclusive supply of osmium, iridium, and ruthenium [37,38]. On a minor scale, platinum is produced in Russia, North America and Canada, as by-products of other metals such as palladium

and nickel/copper (Figure 1-4) [39,40]. The extracted ore usually has a concentration of roughly 4-6 grams of PGMs per metric ton. Of this, around 50-60% is platinum, 20-25% is palladium, and the remaining fraction is made up of other platinum group metals. The next step involves a refining process which separates the PGMs from the base metal and rocks [38].

According to the critical raw materials report provided by the European union (EU) [41], PGMs are considered strategic essential raw materials, defined as materials that will experience an increase in supply while also bearing the potential for supply-related challenges. When we think of the PGMs as a group, the supply risk is not too high. However, only 12% of the demand for PGMs is met through secondary supply, such as recycling. A deeper understanding of the situation can be obtained if platinum is examined independently.

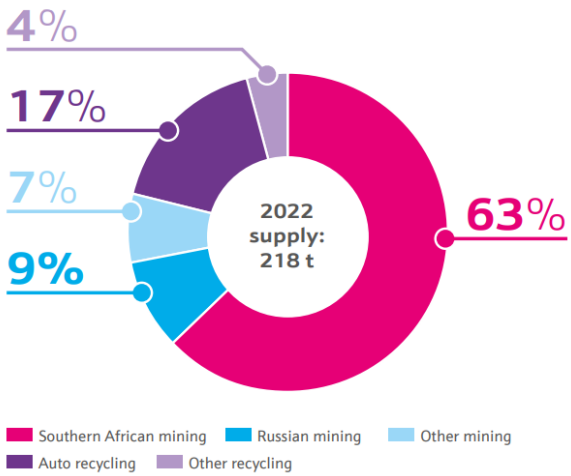

Figure 1-4. Platinum supply in 2022 [40]

Due to the highly centralized production and elevated cost of platinum, ongoing capital investment is needed to access new areas and maintain the infrastructure in the mining zones. Mining companies in South Africa are working towards a sustainable process, investing to meet ambitious targets to decarbonize the system. They seek to reduce their dependency on unreliable energy supply in the country by introducing renewable energy sources, minimizing the overall carbon footprint of platinum [42].

As a valuable metal, the platinum market benefits from a well-established recycling network worldwide. Platinum has the potential for high recyclability; almost all the metal can be reused if it is effectively recovered from its applications [40]. However, some metal losses are associated with collection and handling of the used material [43]. Roughly 10-25% of the platinum in the market originates from recycled sources, mainly from catalytic converters from vehicles but also electronic waste and jewelry [40]. This secondary source of platinum minimizes the environmental impact of the platinum industry compared to the primary mining source. Furthermore, significant amounts of platinum circulate within the system in many industrial applications using platinum catalysts and platinum alloys, such as in chemical and pharmaceutical companies. The catalysts can be internally recycled and reused for the same application, minimizing the demand for new materials.

For the last decade there has been an oversupply of platinum, reflected in a decrease in the price from $1789/troy oz to $1054/troy oz (Figure 1-5)[39]. Despite having more platinum in the marked than actually required, there are continuing efforts to find secondary sources of the metal to avoid any negative impact on the supply chain. Moreover, the demand for platinum is expected to increase in the coming years due to the emergence of new markets such as fuel cells and electrolytic hydrogen generation that are aimed towards energy transition applications [44].

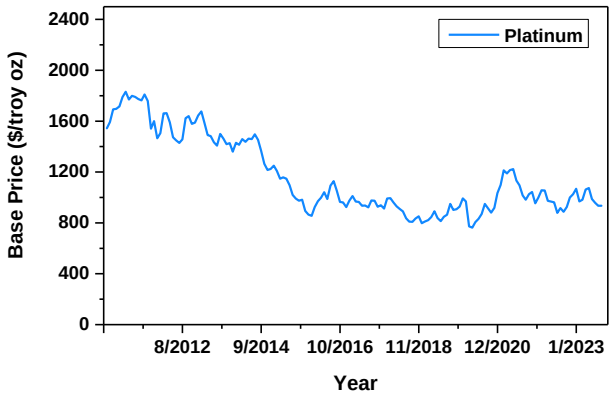

Figure 1-5. Average prices of Pt during 2011–2023 [39]

Platinum is a relatively expensive metal compared to other metals. However, its applications often require significantly less amounts of platinum than base metals, such as in battery applications [45]. Hence, it is recommended to identify intensity of use and

simplicity of use of the metals to make a valid comparison when assessing the use of platinum for new applications [40].

It is estimated that recycled and extracted platinum will be sufficient in the coming decades to meet the increasing demand [40,42]. The PGM deposits in South Africa are estimated to hold vast amounts of platinum that could increase the primary supply with increased investment. Besides, the secondary supply will be sustained to ensure circularity of this valuable resource [44].

1.5 Scope of the thesis

APR has been proposed as an alternative to steam reforming for hydrogen production, avoiding vaporization of the feed, to add value to polyol mixtures in wastewater streams. Over the past years, there has been a surge in the number of studies concerning aqueous phase reforming to produce hydrogen and alkanes. The studies have indicated a relationship between the nature of the support and the active phase of the catalyst translated into catalytic activity. Still, the relatively demanding reaction conditions associated with APR, including hydrothermal environment, acid formations and presence of impurities have thus far prevented the realization of large-scale applications.

Further catalyst design and process intensification developments are necessary to make APR economically feasible to convert organic wastewater streams into sustainable H_2. Thus, alloy formation, strong metal-support interactions, or mesoporous supports with high surface areas are currently being studied to synthesize effective catalysts for aqueous phase reforming applications.

In this context, carbon supports provide the setting to advance in the fundamental understanding of the dynamics of the catalytic APR process, minimizing diffusion limitations, , and allowing exploration into more basic or acidic environments that can promote the activity and selectivity towards H_2 production. Furthermore, the incorporation of bimetallic systems could lead to creation of robust and efficient catalysts capable of withstanding the hydrothermal conditions of APR.

The work in this doctoral thesis concerns evaluation of the potential of platinum-based catalysts supported on carbon nanofibers for hydrogen production by aqueous phase

reforming of polyols. This thesis aims to explore the effects of modifying platinum electron density through the addition of a second metal to the catalytic system or by the introduction of heteroatom dopants to the carbon supports, striving to enhance the metal-support interactions and catalyst activity. These modifications are made with the goal of attaining a stable and selective catalyst for aqueous phase reforming of a polyol feedstock while tuning the reaction conditions to promote high H_2 yields.

Chapter 1 provides the background and motivation for this study. **Chapter 2** presents a literature review summarizing the theoretical background of aqueous-phase reforming including the relevance of carbon nanofibers in catalysis, and the main functionalization of carbon surfaces used in recent studies. The experimental details of catalyst synthesis, characterization and experimental testing are specified in **Chapter 3.** A summary of the results achieved during the development of this work, including research papers and unpublished results is found in **Chapter 4**. This chapter is subdivided into four main sections attributed to the initial catalyst screening, followed by a study that goes deeper into investigating the effect of Mn addition to a Pt-based catalyst (**paper I**). Then, a more comprehensive study of the impact of heteroatom dopants on the carbon supports is explored (**paper II**). Finally, the catalyst stability and effect of the reaction conditions on a promising bimetallic catalyst for aqueous phase reforming applications is evaluated, including a kinetic model of APR of ethylene glycol (**paper III**). Concluding remarks and suggestions for future work are presented in **Chapter 5.**

Chapter 2: Theoretical background

Critical aspects of catalyst design are based on the development of active, stable and selective materials that can withstand demanding operating conditions [46]. In aqueous phase reforming (APR), high feedstock conversion, high selectivity to hydrogen, and stability to hydrothermal conditions are desired. However, the diversity of the feed and presence of water introduce significant challenges to designing a selective and stable catalyst [47]. Thus, various approaches have been explored to try to overcome these barriers.

This chapter provides a description of aqueous phase reforming, including catalytic systems that have been studied to promote APR performance. The discussion explores metals and supports that favor hydrogen production and examines carbon materials, mainly focusing on carbon nanofibers. Additionally, the utilization of dopants to enhance metal-support interactions is included.

2.1 Aqueous phase reforming

Aqueous phase reforming is a catalytic process proposed by Dumesic and co-workers to produce H_2 and carbon dioxide from low-value mixed oxygenated compounds [23]. The conventional approach to aqueous phase reforming of oxygenated hydrocarbons involves operating at low temperatures, around 200-250°C, and pressures near the bubble point of the feedstock (15 -50 bar) [48]. Under these circumstances, the aqueous solution remains in the liquid phase, resulting in a beneficial energy scenario due to the elimination of vaporization, as opposed to steam reforming [49]. Furthermore, these conditions limit the number of decomposition reactions and favor the exothermic water-gas shift reaction, contributing to decreasing CO levels of the final gas mixture. Equation (2-1) illustrates the reforming reaction, succeeded by the water gas-shift reaction (2-2) and the general APR reaction (2-3).

$$C_nH_{2y}O_n \leftrightarrow nCO + yH_2 \quad \textbf{(2-1)}$$

$$CO + H_2O \leftrightarrow CO_2 + H_2 \quad \textbf{(2-2)}$$

$$C_nH_{2y}O_n + nH_2O \leftrightarrow nCO_2 + (y+n)H_2 \quad \textbf{(2-3)}$$

Nonetheless, the promotion of exothermic side reactions at lower temperatures introduces selectivity challenges, leading to the formation of short-chain alkanes [48], as demonstrated in Equation (2-4)

$$CO_2 + 4H_2 \leftrightarrow CH_4 + 2H_2O \quad \textbf{(2-4)}$$

The interactions between the reactant molecule and the active site, as well as the support and metal-support interphase, contribute significantly to the final product distribution in APR, as the reaction mechanism involves different steps [48]. As seen in Figure 2-1, the catalytic pathways responsible for the production of H_2 and CO in APR of oxygenated hydrocarbons involve breaking C-C, C-H, and C-O bonds to obtain adsorbed species on the catalyst surface. Adsorbed CO is removed from the surface by the water-gas -shift reaction, leading to formation of CO_2 and H_2. Consecutive reactions in the gas phase results in alkanes formation through hydrogen consumption. Alternatively, the cleavage of C-O bonds lead to the formation of alcohols by hydrogenation or organic acids involving rearrangement reactions at the expense of H_2 production [50].

APR is susceptible to the reaction conditions, including factors like the composition and concentration of the feedstock, reaction temperature, pressure, type of catalyst and the configuration of the reactor [49]. Hence, the selectivity can be tuned to produce H_2 or alkanes as function of the process parameters [51]. For instance, when using polyols, the selectivity to H_2 usually decreases as the carbon number of the feed increases, due to a rise in undesired side reactions consuming H_2. Additionally, the high functionality of the biomass used as feedstock in the APR process leads to formation of non-desired products that reduce the overall yield and can affect the catalyst stability [52]. Likewise, the acidity of the solution plays a significant role in the outcomes of APR. An acidic solution promotes the formation of alkanes through acid-catalyzed dehydration reactions, while a neutral or basic pH favors the formation of H_2, resulting in high H_2 selectivities [53].

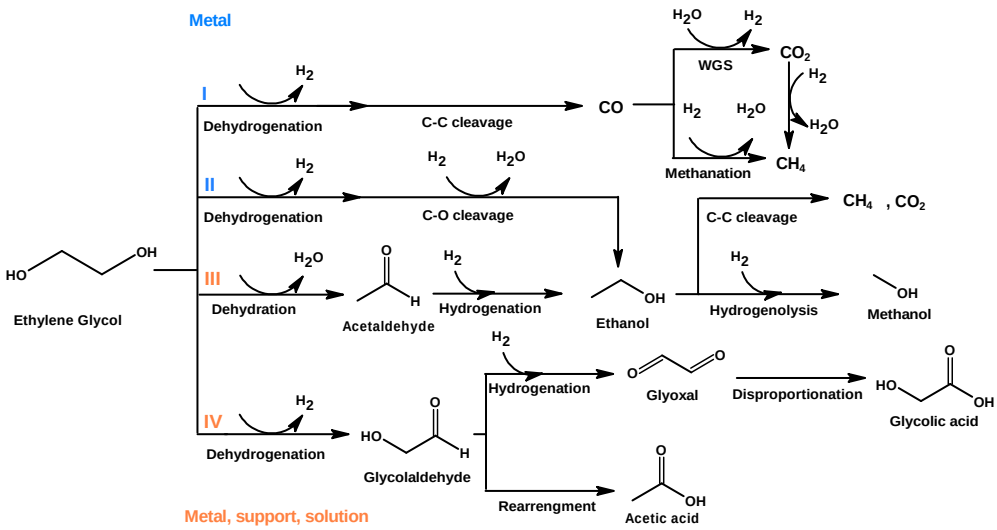

Figure 2-1. Schematic representation of reaction pathways in aqueous phase reforming of polyols, based on previous literature [23,24,54].

2.1.1 Active metals used as catalysts for aqueous phase reforming

The purpose of catalyst development is to facilitate the desired transformations by selectively breaking specific chemical bonds in the feed [55]. As Figure 2-1shows, when C-C bond cleavage and the WGS reaction occur faster than the rate of C-O cleavage and methanation/Fisher-Tropsch reactions, the production of H_2 will dominate in the process. Thus, selecting metals that favor C-C cleavage over C-O cleavage is preferred for APR applications [23].

In general, metals from Group VIII present high activity towards C-C bond cleavage and have been widely studied in APR, highlighting platinum as the most promising metal [24,52]. Within the group of non-noble metals, nickel is renowned for its high activity but is also associated with a significant selectivity towards methane formation. Previous research has identified supported bimetallic catalysts as promising options for APR, exhibiting enhanced catalytic activities compared to their monometallic counterparts [47,56–59]. In the context of APR, bimetallic systems can involve interactions between two metals in their metallic state. Alternatively, one of the metals in the system may be present in an oxidized phase and still have an effect on the overall properties of the catalyst.

The synergistic effects of bimetallic catalysts in APR can enhance a specific desired outcome, such as promoting the rate of C-C bond cleavage and suppress the rate of C-O cleavage or introduce new catalytic pathways. Studies have shown that incorporating metals such as Ni, Co, and Fe into Pt-based catalysts results in higher H_2 turnover frequencies and superior H_2 selectivity compared to monometallic catalysts [60–62]. Huber *et al*. [60] suggested that the enhanced activity of PtNi, PtCo, and PtFe was due to lower heats of adsorption of H_2 and CO than on pure Pt by alloy formation. This leads to a decrease in the surface coverage of H_2 and CO, creating a scenario where a larger number of active sites become accessible to the reactant. Likewise, the addition of Ni or Co to a platinum-based catalyst significantly increased the turnover frequency of H_2 production, maintaining a high H_2 selectivity compared to the monometallic platinum catalyst [57].

Similarly, the introduction of Re as a second metal in aqueous phase reforming has proven to enhance the activity of Pt-based catalysts. The effect is attributed to the synergistic interplay between Re and Pt, which weakens the interaction of CO with the active phase [63]. Furthermore, an increase in the formation of liquid products is observed due to the presence of metal and acid functionalities facilitated by well-dispersed Re oxide species close to platinum, thus decreasing H_2 selectivity [64].

In the case of addition of Mn to Pt-based catalysts, increased conversion and selectivity has been observed when compared to monometallic Pt catalysts [65,66]. According to a study by Bossola *et al*. [65], it has been suggested that Mn forms an alloy with Pt, facilitating the desorption of CO from adjacent Pt sites. Due to a substantial portion of Mn leaching from the catalyst during APR (95%), no direct correlation between the presence of $Mn^{+\delta}$ species that altered the acid-base characteristics of the catalyst and the observed activity enhancement could be established. [65].

New and promising catalyst materials for developing APR are explored, and tungsten appears to be an interesting alternative [35,67–69]. Soták *et al.* [68] studied a tungsten-based catalyst in APR of cellulose, observing significantly higher activities than for a Pt/C catalyst, and stable catalytic performance in the presence of nitrogen and sulfur-containing compounds. It was determined that the presence of the β-W crystalline phase in the catalyst facilitates adsorption of the reactants and subsequent C-C bond cleavage. Furthermore, APR of agricultural waste (steam exploded rice straw hydrolysate) over a tungsten zirconia catalyst resulted in 15% yield towards 5-hydroxymethylfurfural even in the presence of impurities such as acetic acid and xyloses. The catalyst activity was attributed to the presence of Brønsted acidic WO_x clusters on the surface [35].

Bimetallic catalysts can be designed to address typical problems causing catalyst deactivation, such as preventing coke deposition, active metal phase oxidation or sintering of the metal particles, by taking advantage of the positive effects introduced by metal-metal interactions [70]. Under APR conditions, acidic products may lower the pH in the liquid phase, increasing the likelihood of catalyst leaching by oxidation of the metal or formation of organometallic species after being in contact with the feed, as observed for Ni-based catalysts [71–73]. At hydrothermal conditions, reduced nickel particles can oxidize and hydrate to form $Ni(OH)_2$, losing catalytic activity and gaining mobility as they dissolve at acidic conditions [47].

Introducing a second metal can increase the dispersion, suppress the sintering, and prevent dissolution of the metal by improving the corrosion resistance of the metallic surface [72]. Rahman [62] studied the effect of adding Cu and Pt to a Ni-based catalyst supported on MWNT in APR of glycerol. Higher H_2 production and stable catalytic activity for up to 100 hours on stream were observed for both bimetallic catalysts (Pt-Ni, Cu-Ni) compared to the monometallic Ni catalyst. Furthermore, Cu and Pt as promoters were able to minimize Ni oxidation during reaction, with a positive impact on metal dispersion. The characteristic high activity of Cu for the WGS reaction [74] contributed to favorable formation of H_2 in APR of glycerol.

2.1.2 Supports used in aqueous phase reforming

The nature of the support is an additional factor that impacts the selectivity and stability of the catalysts in APR. Properties including surface area, porosity, presence of acidic and basic sites and morphology of the support can affect the overall performance by mitigating transport limitation phenomena or engaging in the catalytic reaction [63]. Supports with high hydrothermal stability and high surface area are preferred for the APR process [49]. Various studies have assessed the influence of acidity of the catalytic system on the selectivity in APR [75,76]. The observations suggested that employing acidic supports such as silica, alumina, and titania leads to faster deactivation and high selectivity to alkanes through promotion of dehydration reactions. On the other hand, hydrogen production is favored by more basic to neutral supports, such as MgO by promotion of the water-gas shift reaction and water activation [48,77].

Alumina is the predominant support in this field, although it has been demonstrated that it is unstable under hydrothermal conditions. During APR, alumina undergoes a phase transition from a metastable phase with a high surface area (γ-alumina) to low surface

area phases like boehmite [78–80]. Similarly, hydrothermal deactivation through pore degradation and phase transformation was observed in supports such as CeO_2, ZnO_2, SiO_2 and TiO_2 [48,63,78].

Carbon-based supports have gained attention due to their hydrothermal stability, tunable chemical properties easily modified by surface functional groups, and resistance under acidic or basic media, making them suitable for APR application [81–83]. Various types of carbon supports have been applied in APR, such as activated carbons, carbon nanotubes, carbon nanofibers, and mesoporous carbon, determining the strong influence of the carbon structure on APR activity [58,63,71,82,84]. It has been observed that catalysts on mesoporous carbon is more favorable for overall catalytic activity. In contrast, irregular pore arrangements, broad pore size distribution, and high microporosity have been shown to negatively affect the catalytic activity in APR [85]. Kim *et al.* [63] studied the effect of the support in APR of various polyols and noted that catalysts supported on carbon, such as ordered mesoporous carbon (OMC) and activated carbon (AC), displayed higher conversion and higher hydrogen yield than silica and alumina-supported catalysts. The improved catalytic activity was attributed to the high surface area and thermal stability of the carbon supports.

2.2 Carbon nanofibers as catalyst supports

Generally, CNF are produced by chemical vapor deposition, although alternative synthesis methods are also employed, including electrospinning with organic polymers, templating, and phase separation [86]. During the synthesis of the CNF, various parameters affect the morphology and properties of the final products, such as type of carbon source, temperature, catalyst, and particle size. Hence, a wide range of carbon structures can be obtained by tuning the synthesis conditions.

CNF can be classified according to the orientation of the graphene layers in relation to the growth axis of the fiber. The types of CNF are referred to as fishbone (or stacked cup), platelet, and tubular. In fishbone CNF, the graphene layers are inclined relative to the central axis. In platelet CNF the layers of graphene are stacked perpendicular to the fiber central axis, while in the tubular type, the graphene layers run parallel to the growth axis [87] as shown in Figure 2-2.

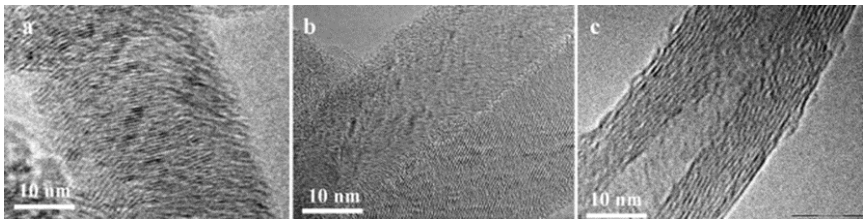

Figure 2-2. TEM images of the different types of CNF (a) platelet, (b) fishbone and (c) tubular[88]

The fishbone and platelet CNF structures provide quite different properties for anchoring of metal nanoparticles. Sanz-Navarro *et al.* demonstrated by using molecular dynamics simulations that metal clusters of Ni are strongly influenced by the curvature of fishbone CNF, introducing strain in the Ni particles whereas Pt where less affected [89].The catalytic performance of Ni clusters can be optimized by tuning the curvature (diameter) of the CNF fibers. However, on platelet CNF also Pt particles are affected by the support due to the mismatch in structure between the platelet edge and the Pt cluster [90]. The Pt particles are being restructured upon adsorption on the CNF as illustrated in Figure 2-3 for a cluster containing 100 Pt atoms, and the average Pt-Pt bond length is enlarged, and the bond order of the platinum atoms are shifted to lower values. The differences in interaction between highly dispersed platinum particles and the platelet and fishbone CNF surfaces are also reflected in the catalytic activity of the materials [91]. It was demonstrated that Pt on platelet CNF exhibits weaker CO adsorption strength than on fishbone CNF, and subsequently higher catalytic activity in oxidation reactions.

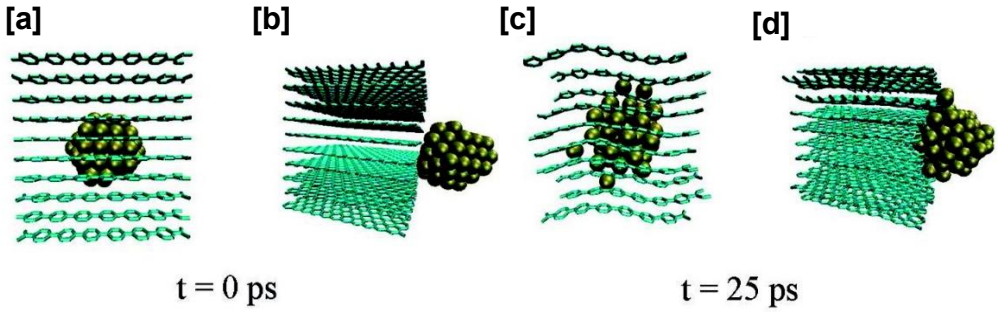

Figure 2-3. Molecular dynamics simulation of a cluster containing 100 Pt atoms interacting with the armchair edge of the platelet CNF without hydrogen termination. (a) and (b) show the initial configuration from two directions. (c) and (d) show a snapshot after 25 ps of equilibration in the simulation [80].

Similar to carbon nanotubes, the CNF exhibit favorable conditions for liquid phase reactions. Not only are they chemically stable in acidic and basic environments, but mass transfer limitations can be avoided by the large pore volumes, open morphology, and high surface areas (100-200 m^3/g) of the CNF [92]. For instance, Santillan-Jimenez *et al*. [93] studied the activity of molybdenum carbide supported on different carbon materials: AC, CNT, and CNF for hydrodeoxygenation of guaiacol where the catalysts supported on CNF and CNT displayed higher phenol yield, and thus superior catalytic activity. The CNF-based catalyst exhibited homogeneously distributed molybdenum carbide nanoparticles with a uniform structural morphology, attributed to the mesopore volume and surface area available for anchoring the metal nanoparticles on the carbon structure.

2.2.1 Carbon surface functionalization by heteroatom doping

The interaction of the support with the active phase directly influences the catalytic activity. Poor interaction can facilitate catalyst deactivation causing the metal particles to diffuse along the surface and sinter. On the other hand, too strong interactions may hinder the interplay between the active phase and the reactants necessary to promote the chemical reaction [94].

In the context of carbon materials, the nature and concentration of chemical species on the surface strongly influence the chemical properties of the material. Different types of heteroatoms or even the same type arranged in a different binding configuration can provide distinct properties to the material [95]. For instance, introducing heteroatoms, such as N, P, and B, into the sp^2 hybridized carbon framework alters the electronic properties of the surface by substituting a carbon atom and transferring more (N) or fewer (P, B) electrons to the material [96]. Thus, modifying these properties by introducing surface functional groups can be tailored to favor interactions between the carbon carrier and supported metal [94,97]. Additionally, these functional groups determine the hydrophilic properties of the carbon surface, influencing the catalyst performance and synthesis dictated by the interaction of the carbon material with the local environment [87].

Diverse applications in catalysis have been explored for carbon surface functionalization, with oxygen and nitrogen functional groups being the most extensively studied [96]. Functionalizing carbon materials typically involves either incorporating functional groups during the direct synthesis of carbon or through post-treatment methods involving heteroatom-containing precursors. Direct synthesis, such as chemical vapor

deposition (CVD) and carbonization, are employed to obtain homogenously distributed heteroatoms throughout the entire carbon matrix [95,98]. In contrast, post-synthesis methods involve introduction of heteroatoms onto the carbon surface, mostly by subjecting the already synthesized carbon material to high-temperature treatment with an impregnated or gaseous heteroatom source [99–101].

Numerous investigations have explored the synthesis and treatments to functionalize carbon supports, emphasizing differences arising from specific heteroatom incorporation [96,98,102,103]. Particularly, the gasification-assisted heteroatom doping method (GAHD) [101] enables the integration of N, S and P into carbon materials while inducing only minor alterations in the texture and structure of the carbon. The approach employs a gasification agent, such as H_2O, CO_2, or H_2, to deliberately induce defects within the carbon material. These defects are subsequently saturated through a simultaneous exposure to a gaseous heteroatom source. As a result, slight changes in the carbon textural properties are achieved, enabling direct comparison of doped carbon materials with various heteroatoms. The following section describes the commonly used heteroatoms for carbon doping, including various functional groups typically encountered and the distinct characteristics they provide to carbon materials.

2.2.1.1 Oxygen functionalization

Among the various surface modification approaches, intentionally introducing oxygen-containing functional groups on the surface of carbon materials is by far the most preferred and versatile strategy for functionalization [87]. The surface oxidation can be applied to add hydrophilicity, increase the reactivity, or create a setting for further modifications of the carbon materials [97].

Oxygen functional groups can be attached to the carbon surface during preparation [104], or functionalities including carboxyl, hydroxyl and carbonyl groups can be introduced on the carbon surface by wet chemical oxidation with strong oxidizing agents such as HNO_3, plasma treatments, photo-oxidation or gas-phase reactions (O_2, CO_2). The method selected determines the final concertation, chemical structure, and distribution of the oxygen functional groups over the carbon surface which ultimately influence the properties of the carbon support [105]. For example, Wepasnick *et al.* [106] reported higher concentrations of carbonyl and hydroxyl functional groups when treating CNT with $(NH_4)_2S_2O_8$, H_2O_2 and O_3 while higher concentrations of carboxyl groups were obtained with HNO_3 and $KMnO_4$ treatments.

Generally, the oxygen functional groups are divided by their acidic or basic properties. When the carbon surface is exposed to oxidative treatments, acidic carbon surfaces with different group distributions are obtained such as carboxylic acids, phenol, and lactone groups. Alternatively, the basic functionalities are obtained after heat treatments in inert atmospheres and exposure to air, where the decomposition of the acidic groups creates defects at the edges of the graphene layers drawing oxygen basic functional groups such as pyrones [102]. In CNT, at the edges of the graphitic planes, hydroxyl groups can be present. Carbonyl groups can be arranged like quinones or pyrones, and ether type of groups can substitute carbon atoms at the edges, as can be seen in Figure 2-4 [107].

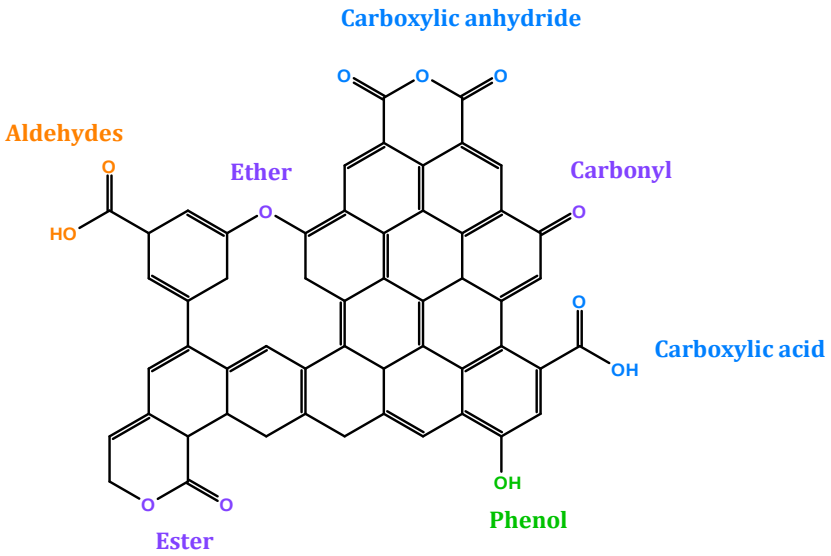

Figure 2-4. Schematic representation of oxygen functional groups on a carbon surface [107]

In catalysis, these oxygen functional groups can serve as attachment points for the metal precursor facilitating controlled synthesis of nanoparticles or enabling a high dispersion of the nanoparticles over the carbon surface [105]. In certain instances, the presence of these oxygen groups can influence the catalytic activity. In APR of ethylene glycol over Pt/CNT [83] and PtCo/CNT [108], the turnover frequency (TOF) was reduced to half when -COOH surface groups were present on the support, even though the dispersion was improved when compared to the original CNT support. The interpretation of this findings relied on the concept of competitive adsorption between water and ethylene glycol on the catalyst surface. Incorporating- COOH groups increases the hydrophilic nature of the support, raising the local concentration of water around the support and decreasing the

concentration of EG, resulting in lower TOF. The catalyst activity was recovered after high-temperature treatments, removing the carboxylic groups on the support.

2.2.1.2 Nitrogen functionalization

Nitrogen, with a stronger electronegativity than carbon, enhances the surface energy and wettability by generating dipoles in the graphitic carbon plane by C-N bonding. Furthermore, the lone pair electrons linked to N dopants add surface reactivity [109]. The most common configurations of N incorporated into graphitic structures are pyridinic, pyrrolic, quaternary and oxidized pyridinic, illustrated in Figure 2-5. Pyridinic nitrogen atoms are located at the edges of the graphene sheet. Pyrrolic nitrogen exists as part of a 5-member ring structure. Quaternary nitrogen resides within the layers substituting a carbon atom. Oxidized pyridinic nitrogen are typically originated at the edges of graphene layers [110,111].

The distribution of these functional groups on the carbon surface strongly influences the catalytic activity of carbon supported catalysts. An abundance of pyridinic nitrogen groups imparts a mild basic nature to the carbon surface, by the presence of lone pair electrons which protonates in aqueous solutions, generating positively charged sites; a feature that can be used to promote condensation reactions [112]. Platinum catalysts supported on CNF have been studied in dehydrogenation of formic acid [113], indicating that the presence of pyridinic surface groups contributes to the formation of electron-deficient Pt sites and C-H bond cleavage in formic acid, leading to enhanced catalytic performance. On the other hand, the presence of quaternary nitrogen species is preferred for the oxygen reduction reaction, as the positive charge of carbon atoms adjacent to nitrogen atoms enhances O_2 adsorption [114].

Experimental and theoretical research have agreed that the use of nitrogen doped carbon materials can promote metal-support interactions enhancing the catalyst stability and modifying the electronic structure of the active phase in the catalyst to improve the activity [109]. Within the context of APR, García-Baldoví *et al.* [115] studied highly loaded Fe-Cu (10-20%wt) catalysts supported on N-doped graphitic carbon in APR of methanol. They emphasized the favored formation of highly active and stable small nanoparticles in the presence of nitrogen atoms as well as a favorable interaction between Fe and Cu by tunning the electron density transfer of the active sites. Additionally, Gogoi *et al.* [116] reported a positive effect of the incorporation of N in the carbon framework of Ru-based catalyst for APR of glycerol. The enhanced catalytic activity was attributed to the

synergistic effects rising from the electronic interactions between nitrogen and Ru. DFT calculations revealed charge transfer from nitrogen to Ru, leading to stabilization of metal nanoparticles and fostering the adsorption of glycerol onto the catalyst surface. Furthermore, the observed higher WGS activity of the catalyst was associated with higher basic strength of the catalyst support, facilitating water dissociation [116].

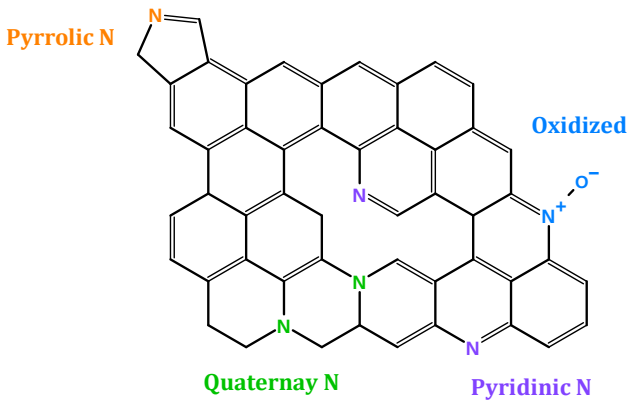

Figure 2-5. Types of nitrogen species found in N-doped carbon: Pyridinic, pyrrolic, quaternary and oxidized pyridinic [111].

2.2.1.3 Sulfur functionalization

In sulfur-doped carbons, sulfur bonds in different configurations including thiophene-S (C-S-C), sulfoxide (C-SO_x-C) sulfone/sulfate groups (SO_x) and sulfonic acid, as illustrated in Figure 2-6. Each of these configurations serves a role in inducing alterations within the carbon structure [117]. Different bond lengths (C-S) in contrast to aromatic carbon bonds (C=C), coupled with a larger atomic radius, introduce stress and nonplanarity within the carbon lattice. Hence, the inclusion of a sulfur atom results in variations in charge distribution, giving rise to the formation of active sites [118].

Carbon materials containing sulfonic groups are characterized by acidic properties, used to promote acid-catalyzed reactions such as esterification/transesterification for biodiesel synthesis [4]. Liu *et al.* [119] synthesized a sulfur-doped carbon with high activity towards esterification of large organic molecules (decanoic acid) due to the high specific surface area and presence of mesopores. However, it was noted that the activity decreased during the reaction due to leaching of SO_3H groups into the solution.

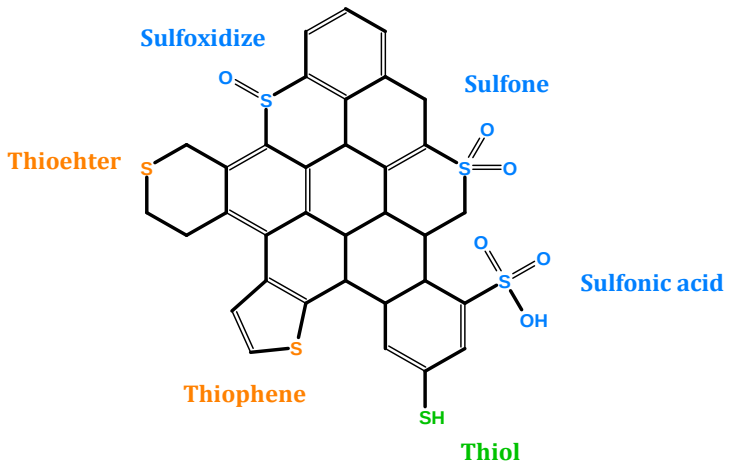

Figure 2-6. Schematic representation of sulfur functional groups on a carbon matrix [100].

Sulfur-based functional groups have gained significant interest due to their strong affinity for noble metals. The strong chemical/electronic interactions between the metal and the S-C support play an important role in the stabilization of Pt nanoparticles, suppressing the sintering of the metal nanoparticles by hindering metal diffusion and nanoparticle migration [120,121]. Yin *et al.* [121] effectively achieved stabilization of 1 nm platinum nanoparticles at elevated temperatures (700°C), preventing sintering.

Furthermore, sulfur, known as a strong catalyst poison [122], selectively adsorbs on metal defect sites. This feature can be employed to tune the catalytic activity by mitigating certain reaction pathways by incorporating small amounts of sulfur in the catalyst structure [123]. Auer *et al.* [123] modified a Pt/Al_2O_3 catalyst with sulfur containing groups, leading to an enhancement in activity and reduction of side products formation. This effect was associated with a gradual blockage of the Pt particles by the sulfur compounds in addition to electronic interactions between P-S that facilitates the desorption of products in the dehydrogenation of perhydro-dibenzyltoluene.

2.2.1.4 Phosphorous functionalization

With the same amount of valence electrons as nitrogen, phosphorous is an interesting choice as a carbon dopant due to its larger atomic radius and higher capacity for electron donation [124]. Similar to sulfur, the introduction of phosphorus into the carbon lattice leads to alterations in the electronic and structural framework of the carbon materials.

Phosphorous can be integrated into the carbon lattice directly or by forming bonds at the surface, leading to the formation of phosphate groups such as PO_4 and their subsequent variations, due to the tendency of phosphorus to bind with oxygen (Figure 2-7).

Introduction of phosphorus leads to a hydrophilic acidic surface and chemical stability to the carbon structure [125]. The phosphorous species with acidic nature enhances carbon reactivity, rendering it active in reactions associated with biomass transformation. The incorporation of C-O-P groups to carbon nanofibers demonstrated high activity in fructose dehydration due to the presence of Brønsted acid sites, such as phosphate groups on the carbon surface, known to be active in this reaction. Nonetheless, at the applied reaction conditions, the functional groups were not stable, leading to phosphate leaching and a subsequent decrease in the catalytic performance [126]. Thermal treatments are suggested to transform C-O-P groups into stable C-P bonds to decrease the tendency of leaching of P species [127].

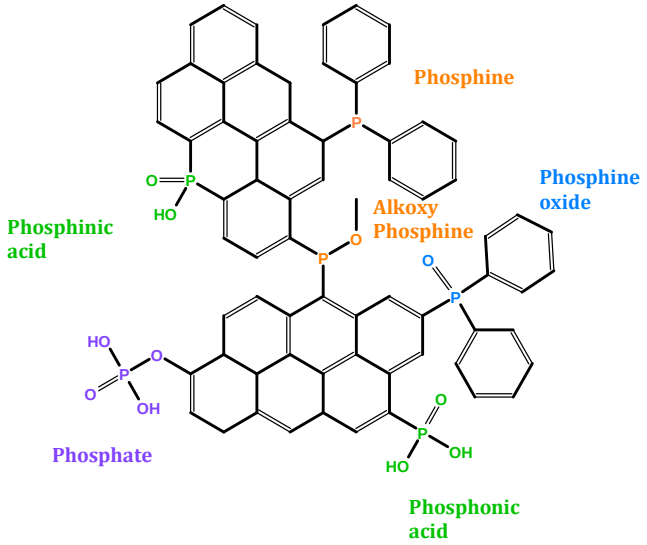

Figure 2-7. Schematic representation of phosphorous functional groups on a carbon matrix [14].

Phosphorus-doped carbons have mostly been studied in electrochemical applications. Long-term stability and high electrocatalytic activity have been observed for Pt-based catalysts supported on phosphorous-doped multiwalled carbon nanotubes. Higher dispersion and better electronic conductivity were observed for the P-containing support in comparison to the P-free support in methanol oxidation reactivity, attributed to the interaction between the Pt nanoparticles and the carbon nanotubes [128].

2.2.1.5 Boron functionalization

Boron, with a similar atomic radius to carbon, introduces defects to the carbon material without damaging the initial structure. By substituting carbon, boron can act as an electron acceptor due to its three valence electrons, modifying the electronic system and promoting charge transfer [129]. Boron can be integrated into the carbon lattice with configurations such as BC_3, B_4C, C-O-B, or it can be present in the surface as various oxygen containing groups, as shown in Figure 2-8.

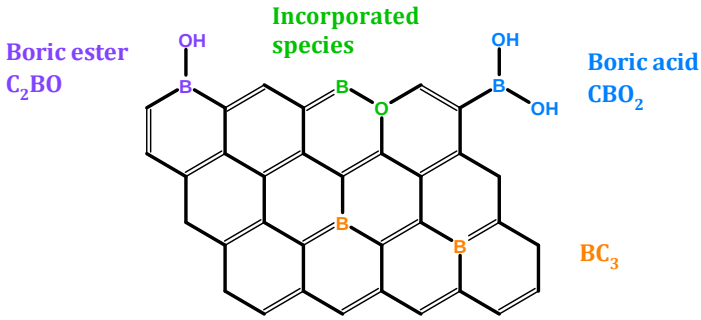

Figure 2-8. Schematic representation of boron functional groups in a carbon matrix [130].

According to DFT studies, the presence of boron defects in carbon supports enhance the adsorption energy of metal atoms in the catalyst, such as Pt and Ru. On the boron-doped carbon, Pt prefers to adsorb on bridge sites common to two aromatic rings, and the adsorption energy increases due to electron transfer from Pt to the support [131]. This interaction has been confirmed by XPS studies, revealing a stronger interaction between Pt nanoparticles and the boron-doped carbon support compared to the Pt interaction with pure carbon [132].

In liquid phase reactions, the effect of boron doping was studied in hydrochlorination of 2,4-dichlorophenol over a Pd-based catalyst. It was found that introducing boron intensifies the metal-support interaction, resulting in increased Pd dispersion and Pd cationization, leading to higher catalytic activity [133]. Furthermore, Esteve-Adell *et al.* [134] studied APR of glycerol over different doped graphenes (N,B,P) as metal-free catalyst. Boron-doped graphene exhibited the highest catalytic activity attributed to formation of frustrated Lewis acid-base pairs in conjunction with negatively charged oxygen groups on the graphene surface. Nonetheless, B-doped graphene produced hydrogen at a rate significantly lower than a Pt-based catalyst.

Chapter 3: Materials and methods

In this section, an overview of the materials, experimental setups and procedures used to conduct the experiments and investigations discussed in this study are presented.

3.1 Carbon nanofiber synthesis

Platelet carbon nanofibers (CNF) were synthesized utilizing chemical vapor deposition, employing Fe_3O_4 as the catalyst and CO/H_2 as gas precursors. Approximately 100 mg of catalyst was reduced at 600°C for 6 hours in a 25% H_2/Ar mixture. Subsequently, the system was purged with Ar for 30 minutes, after which a synthesis gas blend of CO/H_2 in a volumetric ratio 4:1 was fed into the reactor (total flow of 62.5 ml/min) and maintained for 46 hours at 600°C. Following the synthesis, the resultant carbon was gradually cooled to room temperature under a continuous flow of Ar.

3.2 Post-synthesis treatments of the carbon nanofibers

3.2.1 Acid treatment

Two different acid treatments were used in the performance of this thesis: A mild treatment conducted at 90°C for 3 hours was used to compare monometallic and bimetallic catalysts (Paper I). Additionally, a rigorous treatment at 120°C for 24 hours was utilized in experiments investigating the impact of dopants on catalyst activity (as discussed in Paper II). A standardized procedure was applied in both cases, with the objective of eliminating the Fe_3O_4 growth catalyst present within the fibers and introducing oxygen functional groups onto the carbon surface. In short, the CNF were exposed to concentrated nitric acid (65-70%wt) under reflux conditions for the specified duration and temperature. Following this, the resulting suspension was filtered, washed with deionized water until reaching a pH of 7, and dried overnight at 100°C. The carbon nanofibers subjected to acid treatment are referred to as CNF-ox.

3.2.2 Heat treatment

The heat treatment of CNF-ox was conducted in a vertical tubular furnace using a quartz reactor. The CNF-ox was exposed to an argon atmosphere (100 mL/min) at 700°C for 2 hours. This process aims to eliminate unstable oxygen groups introduced in the carbon surface during the acid treatment. The carbon nanofibers subjected to heat treatment are designated as CNF-HT.

3.2.3 Carbon surface heteroatom functionalization

The gasification-assisted heteroatom doping method [101] was used to functionalize the CNF with nitrogen, sulfur, and phosphorous. This approach involves using a gasification agent such as H_2, CO_2, or H_2 to introduce defects into a carbon material. Simultaneously, these newly formed chemisorption sites are exposed and saturated with a gaseous source of heteroatoms containing N, S, or P. Briefly, the carrier gas is saturated with a heteroatom precursor solution and put into contact with the CNF-ox at a specified temperature and reaction time using a saturator upstream of the reactor. During the heating and cooling phases, the carrier gas is directly channeled into the reactor, bypassing the saturator. 350 mg of CNF-ox was used in each doping experiment .

3.2.3.1 N-doped carbon nanofibers (N-CFN)

Ethylene diamine (Sigma Aldrich, ≥ 99.5 %) was used as the nitrogen source, and water as the gasification agent. The CNF-ox was placed in a quartz reactor and heated to 875°C at a rate of 10°C/min in 250 mL/min of N_2. Once the desired temperature was reached, a solution consisting of a 1:1.5 molar ratio of ethylene diamine to water was fed into the reactor from the N_2 flow through a saturator containing the solution. After an hour of exposure, the system was cooled down in N_2 atmosphere.

3.2.3.2 S-doped carbon nanofibers (S-CNF)

During the CNF-ox heating process in the reactor, a mixed carrier gas consisting of 10% CO_2/N_2 at 100 mL/min was utilized. At a temperature of 825°C, carbon disulfide (Sigma-Aldrich, ≥ 99.9 %) was introduced to the reactor using 2mL/min of N_2 through the saturator containing the sulfur source. The exposure time was 11 min. Subsequently, the

reactor was cooled down in 90 mL/min N_2 flow. Due to the high volatility of CS_2, the saturator was kept cool with a mixture of ice and NaCl (10:1 g/g) during the experiments. To remove unstable sulfur-containing groups in H_2 atmosphere, the freshly doped CNF were exposed to H_2 at 450°C for 30 min with a heating rate of 10°C/min.

3.2.3.3 P-doped carbon nanofibers (P-CNF)

The reactor containing CNF-ox was heated to 825°C at 10°C/min in 50 mL/min of H_2. Once the desired temperature was reached, the carrier gas flow was directed through the saturator filled with trimethyl phosphite (Sigma-Aldrich, ≥ 99%) to feed into the rector for a 3-hour exposure. Afterwards, the system was cooled down in N_2 atmosphere. Synthetic air was supplied to the system starting from 80°C during the cooling step to oxidize any possible white phosphorous formed.

3.2.3.4 B- doped carbon nanofibers (B-CNF)

The wet impregnation method proposed by Chiang *et al*. [135] was used to functionalize CNF with boron. In short, for 3%wt boron loading, 2.5 g of CNF-ox and 0.23 g of B_2O_3 were suspended in 250 mL DI water in a 500 mL round-bottom flask. The mixture was sonicated for 25 minutes in an ultrasonic bath at 25°C. Afterwards, the suspension was heated to 80°C in an oil bath and mixed with a magnetic stirrer. After 2 hours, the mixture was dried for 24 hours at 60°C in an oven, followed by heat treatment at 1000°C in argon atmosphere for 8 hours.

A washing procedure was required to eliminate the excess of boron oxide in the produced B-CNF. The B-CNF were immersed in DI water and subjected to an ultrasonic bath for 25 minutes. Next, they were heated with constant stirring to 80°C in an oil bath. After 2 hours, the hot mixture was filtered and dried for 14 hours in an oven at 60°C.

3.3 Catalyst synthesis

3.3.1 Incipient wetness impregnation

Chloroplatinic acid hexahydrate H_2PtCl_6 x $6H_2O$ (Sigma-Aldrich, > 37 % Pt basis) was used as metal precursor and acetone (Sigma Aldrich, 99.9 %) as solvent. The Pt solution was

gradually mixed with the support and kept at room temperature overnight, followed by drying at 100°C for a duration of 20 hours. Subsequently, the prepared catalyst underwent a heat treatment under nitrogen atmosphere (100 mL/min) at 320°C (heating rate of 3°C/min) for a duration of 2 hours, aiming to decompose the precursors from the synthesis.

For the PtMn catalyst synthesis a similar procedure was followed. Manganese (II) nitrate hydrate $Mn(NO_3)_2{\cdot}xH_2O$ (Sigma Aldrich, 98%) was used as Mn precursor and acetone as solvent. The metal precursor solutions were added to the CNF by co-impregnation, followed by a drying and heat treatment step under the same conditions as established for the monometallic catalyst.

$PtWO_3$/CNF-ox was prepared by co-impregnation of CNF-ox with an aqueous solution of ammonium tungsten oxide hydrate $(NH_4)_6W_{12}O_{39}xH_2O$ (Sigma-Aldrich, 99.99%) and chloroplatinic acid hexahydrate. Typically, the loading was 3%wt Pt and 0.7% W. After the impregnation, the catalyst was kept at room temperature to dry overnight, followed by a drying step at 200°C for 12 hours. Subsequently, the catalyst was heat treated at 400°C for 2 hours in inert atmosphere.

PtWC/CNF-ox was prepared by sequential impregnation. Initially, an aqueous solution of ammonium tungsten oxide hydrate was gradually added to the support and left to dry at room temperature overnight. The resulting tungsten-containing CNF-ox was loaded into a quartz reactor to reduce the catalyst at 400°C for 1 hour under a 50%H_2/Ar flow. After reduction, a heat treatment in Ar atmosphere at 1000°C for 1 hour was conducted. Then, an aqueous solution of chloroplatinic acid hexahydrate was used to impregnate WC/CNF-ox, following the same conditions as the monometallic Pt-based catalyst.

3.3.2 Flame spray pyrolysis

The catalysts were synthesized employing a double flame configuration in a flame-spray pyrolysis process. The setup included five primary components as presented in Figure 3-1: The filter located at the culmination of a collection chamber positioned above the burner heads, a vacuum pump utilized to gather particles by sustaining a continuous gas flow through the filter, gas valves responsible for regulating the gas flow rate and fuel concentration within the flame, and a dosing pump that controlled the rate at which precursor solutions were sprayed into the flame.

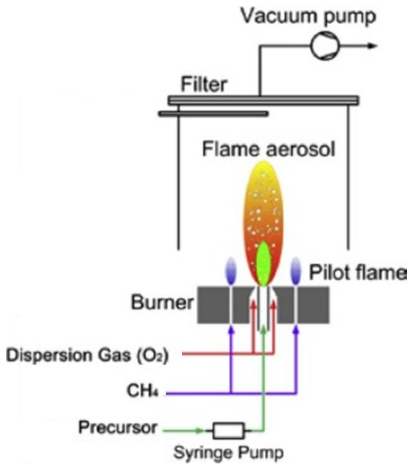

Figure 3-1. Flame Spray Pyrolysis System schematic [136].

Detailed information about the synthesis by flame spray pyrolysis can be found elsewhere [137–139]. In short, a solution dissolving aluminum (III) acetylacetonate $Al(acac)_3$ (Merk, >99%) and magnesium acetate tetrahydrate $(CH_3COO)_2Mg{\cdot}4H_2O$ in a Mg:Al molar ratio of 2.3 was prepared in a mixture of methanol and acetic acid in ratio 1:1 %v (200 mL). A second solution with platinum(II) acetylacetonate $Pt(acac)_2$ for the monometallic catalyst and adding manganese (II) acetylacetonate $Mn(acac)_2$ for the bimetallic catalyst (molar ratio Pt:Mn 3:1 and 1:1) in a mixture of methanol and acetic acid in ratio 1:1 %v (200mL) was prepared.

The solutions were sprayed simultaneously with a constant flow rate of 5mL/min and the particles were collected in a glass wool filter. The yielded nanoparticles were calcined at 350°C for 5 hours to fully oxidize the carbon-containing remains of the sprayed solutions.

3.4 Catalyst characterization

3.4.1 N_2 physisorption

The textural properties of the catalysts were measured by N_2 physisorption at -196 °C using a Micromeritics Tristar 3000 instrument. Before the analysis, the samples were degassed overnight under vacuum at 200°C. About 100 mg of the samples was used for

the measurements. The specific surface area was calculated by the Brunauer-Emmet-Teller (BET) method [140].

3.4.2 Chemisorption

CO chemisorption was used to estimate the Pt dispersion of the catalysts assuming a Pt/CO adsorption stoichiometry of 1:1 [141]. About 100 mg of the sample was reduced *in-situ* for 1 hour in H_2 flow at 300°C with a heating rate of 5°C/min. Following the reduction step, the setup was purged with helium at 120°C for 30 minutes and cooled to 35°C to perform the chemisorption analysis in a Micromeritics ASAP 2020 instrument. From recurrent experiments, a standard deviation of +/-1 in dispersion values was determined, meaning that the estimated error in chemisorption measurements falls within the range of 1-2.5%.

3.4.3 X-ray diffraction

X-ray diffraction (XRD) patterns were measured on a Bruker D8 A25 DaVinci X-ray diffractometer using Cu Kα radiation (λ = 1.5406 Å) and a LynxEye detector. Diffractograms were acquired in the 2θ range 10-80° with a fixed divergence slit of 0.2. The acquisition time for all measurements was 60 min. Peak identification was conducted using the information provided from the crystallography open database [142]. The Pt average crystallite size was estimated from the XRD pattern utilizing the Scherrer equation, taking a value of 0.89 for the Scherrer constant [143].

3.4.4 X-ray photoelectron spectroscopy

X-ray photoelectron spectroscopy (XPS) was conducted in a Kratos Analytical Axis Ultra DLD spectrometer using monochromatic Al Kα radiation (1486.6 eV) operating the anode at 10 kV with an aperture of 700 x 300 μm. The measurements were performed at ambient temperature under ultra-high vacuum. Survey spectrums were acquired with a pass energy of 160 eV, while high-resolution spectra were recorded with a pass energy of 20 eV. The energy axis was calibrated to the C 1s contribution of sp2 carbon at 284.6 eV.

Following Shirley background subtraction [144], the peaks were deconvoluted and fitted to linear combinations of Gaussian and Lorentzian functions (pseudo-Voigt-profiles). For comprehensive details on the fitting procedures, refer to papers I and II in the appendices.

3.4.5 Scanning transmission electron microscopy and energy-dispersive X-ray spectroscopy

Scanning transmission electron microscopy (STEM) micrographs were obtained on a Hitachi SU9000 electron microscope operating at an accelerating voltage of 30 kV with a beam emission current of 10 μA. Energy dispersive X-ray spectroscopy (EDS) maps were recorded at an accelerating voltage of 30 kV using an Oxford Ultim Extreme 100 mm^2 detector and a pixel dwell time of 400 μs. Before the analysis, the samples were dispersed in n-hexane using an ultrasonic bath and deposited on carbon coated copper grids using a drop-casting technique.

3.4.6 Raman spectroscopy

Raman spectroscopy was conducted using a Horiba Jobin Yvon LabRAM HR800 Raman microscope, utilizing a HeNe laser operating at a wavelength of 633 nm. The spectra were recorded in the range from 750 cm^{-1} to 3250 cm^{-1} with an acquisition time of 30 s. The methodology outlined by Mallet-Ladeira *et al.* [145] was followed to fit the Raman spectra and retrieve information about the G and D bands of the samples (I_D/I_G ratio). A minimum of five spectra from distinct locations on each sample were recorded and analyzed.

3.4.7 Microwave plasma atomic emission spectroscopy

Microwave plasma atomic emission spectroscopy was used to determine the metal loading in an Agilent 4210 MP-AES optical emission spectrometer. Before the analysis, the samples were prepared through a microwave-assisted acid digestion method, utilizing the Speedwave XPERT instrument from Berghof. The process was divided into two steps to carry out the acid digestion. Initially, the temperature was raised to 170°C for 10 minutes, then increased to 210°C for 20 minutes using a power of 2x800 W in a mixture

of HCl/HNO_3 (1:4, vol: vol). Then, the samples were diluted to 100 mL in a volumetric flask with milli-Q water and filtered using a syringe filter with a pore size of 0.2 μm. External calibration for the metals Pt, Mn, W, and Ni was performed before each measurement, using commonly available ICP standards (Sigma Aldrich, 1000 mg/L).

3.5 Experimental APR setups

3.5.1 Batch reactor system

A mini bench batch reactor (Parr 4592) equipped with a magnetic stirrer and PI temperature controller was employed to carry out the APR screening experiments at various temperatures ranging from 225-270°C. The reactor vessel was loaded with the pre-reduced catalyst (100-500 mg) and 30 mL of 6%wt aqueous solution of ethylene glycol. The setup was leak-tested at 120 bars before each reaction. The system was purged and pressurized with N_2 to 20-26 bars. The mixture was stirred and heated to the desired temperature during two hours of reaction. Subsequently, the reaction was quenched to room temperature using an ice bath.

The gaseous products were collected in a gas sampling bag and analyzed by gas chromatography (Agilent 7820A) equipped with a thermal conductivity detector (TCD) and flame ionization detector (FID) employing Agilent Porapak-Q GS-Q, CP-Molsieve 5Å, and J&W HP-PLOT Al_2O_3 KCl columns for the separation of the gases. N_2 was employed as an internal standard for the quantification of the products present in the gas phase. The liquid phase was filtered using a 0.2 μm PTFE filter and analyzed using high-performance liquid chromatography (1260 Infinity II LC System, Agilent technologies) equipped with refractive index detector (RID). The separation of the components was executed at 60°C with a constant flow rate of 0.6 mL/min of 5 mM H_2SO_4 aqueous solution in an Agilent Hi-Plex column (300 mm x 7.7 mm). An external calibration was used to precisely quantify the reaction products, employing expected reaction products as references.

3.5.2 Semi-batch reactor system

A semi-batch rector system was used in the kinetic measurements. It consisted of a 300 mL stainless-steel benchtop Parr reactor (Parr 4560 model) equipped with a back-pressure regulator. About 200 mg of catalyst inside a sealed glass capillary was loaded

into the reactor with 60 mL of 1-20%wt aqueous solution of ethylene glycol. The reactor was pressurized with He to 40 bars and the pressure was maintained constant during the experiment by the back-pressure regulator.

The reactions were carried out in the temperature range of 215-235°C for 4 hours. Once the reactor reached the desired temperature, the agitation of the systems started breaking the glass capillary containing the catalyst, allowing it to come into contact with the liquid phase. This marked the starting point of the reaction, considered as time zero. The gas phase products were analyzed by an online micro-GC (3000A Agilent) equipped with a TCD. Agilent J&W CP-Molsieve 5Å column and HP-PLOT U column were used for the analysis of H_2, CO_2, CO and CH_4. The liquid phase products were analyzed off-line using a GC-FID ALS (Agilent 7820A) equipped with an Agilent J&W VF-Xms column.

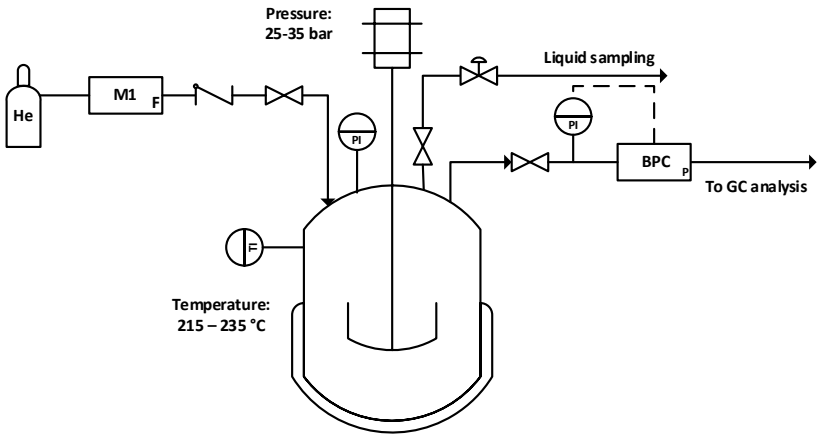

Figure 3-2. Semi-continuous setup utilized for the kinetic studies of aqueous phase reforming of ethylene glycol

3.5.3 Continuous-flow reactor system

Figure 3-3 illustrates a schematic of the experimental setup used for the continuous-flow APR testing. The reaction was carried out in up-flow configuration to ensure total wettability of the catalyst bed. A stainless-steel tubular reactor (15 mm internal diameter, 385 mm length) was loaded with approximately 0.3 g of catalyst (125–250 μm) mixed with SiC (125–250 μm) in a 1:1 mass ratio. The catalyst was reduced *in-situ* at 300°C (heating rate 5°C/min) in 10% H_2/N_2 flow (100 mL/min) for 1h. The system was then pressurized to 30 bars, and the pressure regulated with a back-pressure regulator using

25 mL/min N_2 and heated up to 225°C to carry out the reaction. An aqueous ethylene glycol solution (6%wt) was supplied into the reactor at 2 h^{-1} weight hourly space velocity (WHSV). The online gas chromatograph (Agilent 8890) equipped with TCD and FID detectors is used to monitor the gas phase reaction products. For component separation, CP-Sil 5 CB, CP-Molsieve 5Å, and Haysep-A columns were employed. Liquid phase samples were collected hourly and subjected to analysis using an offline HPLC, as outlined in section 3.5.1.

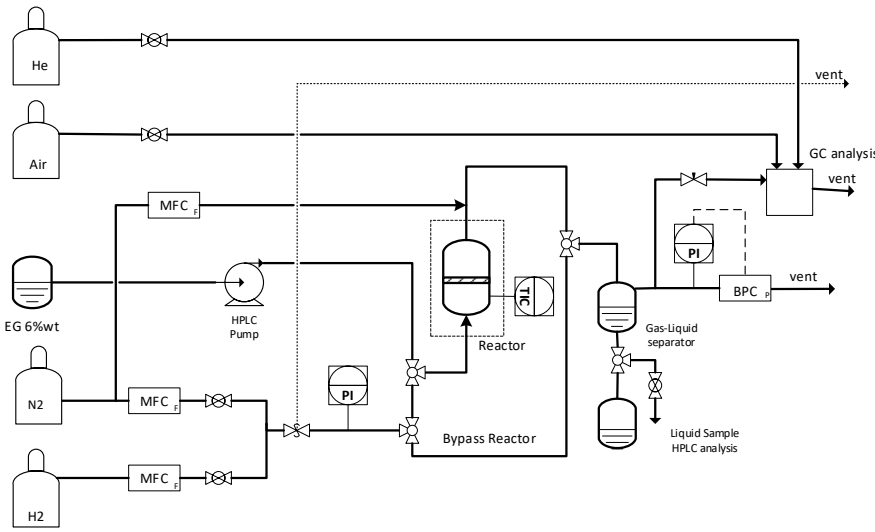

Figure 3-3. Continuous-flow setup utilized for aqueous phase reforming of ethylene glycol.

3.6 *In-situ* XAS-XRD characterization

In-situ powder XAS-XRD experiments were conducted at BM31 of the Swiss-Norwegian Beamlines (SNBL) at the European Synchrotron Radiation Facility (ESRF) located in France. The experimental setup used for the *in-situ* experiments is similar to a continuous-flow reactor system (Figure 3-3), including a dedicated mass flow controller for H_2 and N_2 feed, a back pressure regulator to maintain the pressure in the system and a HPLC pump to feed the ethylene glycol aqueous solution. Catalyst samples (8 mg) of 120-200 µm sieve fraction were placed into a quartz capillary tube with internal diameter of 2.0 mm and wall thickness of 0.02 mm. To secure the catalyst within the catalytic bed, quartz wool

plugs and Kapton polyamide tube pieces (microlumen) were positioned at both ends of the bed. The capillary reactor assembly was mounted in a custom-designed cell and exposed to X-rays. The temperature of the capillary was controlled using a hot air blower during the experiments.

X-ray patterns were acquired employing a Pilatus3 2M detector (Dectris) using monochromatic radiation (wavelength λ = 0.255 Å). To ensure accurate measurements, corrections for the instrumental peak broadening, wavelength calibration and detector distances were conducted using a NIST 660 LaB_6 standard. X-ray absorption spectra were recorded at the Pt L_3 edge (11.564 keV), employing transmission mode for data collection. X-ray absorption near edge structure (XANES) profiles were obtained during reduction of the catalyst (300°C, 5%H_2/He flow, 1 hour) and during aqueous phase reforming of EG at 225°C, 30 bars and 9 h^{-1} WHSV (0.02 mL/min) for 2 hours. Extended X-ray absorption fine structure (EXAFS) measurements were conducted before and after reduction and aqueous phase reforming at 50°C. Platinum standards involving EXAFS measurements of platinum foil (Pt^0) and PtO_2 (Pt^{4+}) were collected *ex-situ* in transmission mode.

The phyton-based multivariate curve-resolution-alternating least squares (MCR-ALS) package (3.10) was used to analyze the acquired XANES data during TPR and APR experiments on the catalyst [146]. For the EXAFS data analysis, the Demeter software package components Athena and Artemis, were utilized [147]. Detailed information about the fitting parameters used in the applied data treatment techniques is presented in paper II. In short, the data analysis of the platinum-based catalyst supported on CNF-HT, N-CNF, and S-CNF involves multiple shells fitting in k space with k2-weighting. Attempting to fit the EXAFS data from platinum catalysts supported on P-CNF and B-CNF in k space did not result in an adequate fit. Hence, these samples were fitting in R-space. The range used for the fit is f $3 < k < 12$ $Å^{-2}$ and $1.1 < R < 4$ Å. The number of floating parameters employed in the analyses meets the Nyquist criterion.

Additional *in-situ* XAS experiments were conducted at the CAT-ACT beamline at the Karlsruhe Institute of Technology (KIT) light source [148]. The experimental setup used for these experiments was explicitly designed at KIT for high-pressure applications, including a stainless-steel cell with large solid angle openings that facilitates XRD-XAS measurements at the challenging conditions of APR. Detailed information about the setup is presented in the work by Loewert *et al.* [149].

3.7 APR activity and selectivity calculations

For the activity and selectivity calculations, nitrogen served as an internal standard in all of the employed experimental setups. In the case of the continuous and semi-continuous setups, a nitrogen flow rate of 25 mL/min was used to determine the flow rate of gaseous products, based on chromatography-measured composition of each component. The estimation of the gas phase flow rate was conducted through the application of the ideal gas law, with a reference to room temperature (25°C or 298.15 K). In the batch reaction setup, the total moles of N_2 in the system were estimated using the actual initial temperature and pressure of the system.

Furthermore, given that the continuous-flow APR experiments were conducted in an up-flow configuration, with a diluted ethylene glycol (EG) feed and operating at moderate conversion levels, it was assumed that the outlet liquid flow rate equaled the inlet flow rate. The key parameters considered for evaluating the performance of the studied catalysts in aqueous phase reforming are presented in Table 3-1.

Table 3-1. Parameters and equations applied to evaluate APR performance

Parameter		Batch	Continuous
Conversion	$X_{EG}(\%)$	$\frac{mol_{EG\ initial} - mol_{EG\ final}}{mol_{EG\ initial}}$	$\frac{F_{EGin}(mol/min) - F_{EGout}\ (mol/min)}{F_{EGin}\ (mol/min)}$
Hydrogen selectivity – Carbon based	$S_{H2}(\%)$	$\frac{mol\ H_{2\ produced}}{{C_{total,g}}^{a}}\ x\ \frac{1}{R^b} x100$	$\frac{F_{H2\ produced}\ (mol/min)}{{FC_{total,g}}^{a}}\ x\ \frac{1}{R^b} x100$
Carbon based selectivity	$S_{i,g}\ (\%)$	$\frac{{C_{i,g}}^{c}}{{C_{total,g}}^{a}}\ x\ 100$	$\frac{{FC_{i,g}}^{c}}{{FC_{total,g}}^{a}}\ x\ 100$
Hydrogen site time yield	$STY_{H2}(min^{-1}$	$\frac{{H_{2\ production\ rate}}^{d}\ {Mw_{Pt}}^{e}}{{D_{Pt}}^{f}{W_{cat}}^{g}{X_m}^{h}}$	$\frac{F_{H2produced}\ (mol/min)\ \ {Mw_{Pt}}^{e}}{{D_{Pt}}^{f}{W_{cat}}^{g}\ {X_m}^{h}}$
Carbon yield to liquid products	$C_{i,L}\ (\%)$	$\frac{{C_{i,L}}^{j}}{{C_{EG\ inital}}^{k}}\ x\ 100$	$\frac{{FC_{i,L}}^{j}}{{FC_{EGin}}^{k}}\ x\ 100$
Carbon yield to gaseous products	$C_{i,g}\ (\%)$	$\frac{{C_{i,g}}^{c}}{{C_{EG\ inital}}^{k}}\ x\ 100$	$\frac{{FC_{i,g}}^{c}}{{FC_{EGin}}^{k}}\ x\ 100$

[a] Total carbon present in the gas phase

[b] Stoichiometric reforming ratio for EG $R = H_2/CO_2 = 5/2$

[c] Total carbon in each gaseous product (i)/ Total flow of carbon in each gaseous product (i) (mol/min)

[d] Moles of H_2 produced divided by the duration of the experiment (120 min)

[e] Molecular weight of Pt

[f] Pt dispersion estimated by CO chemisorption (%)

[g] Amount of catalyst (g)

[h] Weight fraction of Pt in the catalyst (%wt)

[j] Total carbon in each liquid product (i) / Total flow of carbon present in each liquid product (i)

[k] Total carbon contained in the feed stream / Total inlet flow of carbon contained in the feed stream

Chapter 4: Results and discussion

This chapter provides summaries of the work detailed in the research papers included in the thesis, along with discussions about preliminary findings related to catalyst screening (section 4.1). The content in this section is structured around relevant themes connected to the papers.

4.1 Screening of bimetallic catalyst for hydrogen production via aqueous phase reforming

In the search for a suitable catalyst for aqueous phase reforming, some crucial aspects must be fulfilled in terms of performance. The catalyst should demonstrate high activity for both the reforming and water-gas shift reactions, while remaining stable under the challenging conditions of aqueous phase reforming. Furthermore, it is desirable to obtain a catalyst highly selective towards H_2. The catalyst should favor C-C bond cleavage over C-O bond cleavage and prevent hydrogenation of CO or CO_2 into methane [23].

Several researchers have studied aqueous phase reforming of polyols, emphasizing the relevance of various factors such as the synthesis method, the selection of the active metal in conjunction with potential promoters, the nature of the support and other factors that significantly contribute to the catalyst performance. Within this segment, the catalyst screening involves evaluating the influence of various metals and supports on the activity, selectivity, and stability of Ni and Pt-based catalysts in aqueous phase reforming of ethylene glycol.

This section includes a brief introduction of the project that triggered this research, followed by the results of the catalyst screening.

4.1.1 BIKE project: Bimetallic catalysts in knowledge-based development for energy applications

The BIKE project is a Marie Skłodowska-Curie Actions (MSCA) doctoral network formed to advance the development of cutting-edge bimetallic catalysts for the energy sector, primarily emphasizing the H_2 field. The project explores various technologies, including

steam reforming (SR), aqueous phase reforming (APR), and anion exchange membrane water electrolysis (AEMWE), all aimed at enhancing the conversion of raw materials into H_2 and syngas.

The project consists of 10 beneficiaries, including 8 from academia and 2 from the industrial sector, along with 4 partners from both the public and private sectors. The beneficiaries are the National Research Council of Italy (CNR), Bulgarian Academy of Science (BAS), Technical University of Catalonia (UPC), Agencia Estatal Consejo Superior de Investigaciones Científicas (CSIC), Durham University (UDUR), Karlsruhe Institute of Technology (KIT), Technical University of Denmark (DTU), Norwegian University of Science and Technology (NTNU), and industrial partners Johnson Matthey (JM) and ICI CALDAIE SPA (ICI). Their collaborative efforts involve expertise in various areas of heterogeneous catalysis such as metal nanoparticle synthesis, support preparation, catalyst development, characterization, and testing.

Hence, through the integration of diverse multidisciplinary and complementary expertise, the project aims to explore unified strategies for enhancing catalytic activity, selectivity, and stability, by introducing a second metal into a monometallic catalyst and studying the synergistic effects arising from the possible interaction between the two metals.

The contribution of NTNU to the project is in the research line dedicated to aqueous phase reforming. Within this context, NTNU was responsible for screening catalysts developed by various project partners. The evaluation process involved assessment of different materials at low temperatures (225-270°C) in the presence of pressurized liquid water. This section provides an overview of the APR activity screening outcomes for the catalysts developed by the other BIKE partners.

4.1.2 Studied catalyst systems within the BIKE framework

During the early development stage of the project, a range of bimetallic catalysts were investigated for their potential in hydrogen production through aqueous phase reforming (APR) of ethylene glycol. The evaluation process involved testing the catalysts under milder operating conditions, with low temperatures (225-270°C) and pressures (20-50 bar) in a batch reactor.

For fundamental studies, ethylene glycol is widely explored in the literature in the APR context, and it is selected due to its simplicity. Ethylene glycol facilitates the

understanding of the chemistry in the APR process, containing the same functional groups as larger polyols but producing fewer by-products [150] .

The catalytic features of the bimetallic catalysts, including activity and selectivity, were examined using a lab-scale testing set-up. The screening focuses on two key performance indicators (KPIs) addressing the selectivity and stability challenges encountered in APR operating conditions, looking for a catalyst that displays high hydrogen yield with a low degree of metal leaching. Once the initial screening is completed, the selection of promising bimetallic catalysts will enable delving into further studies gaining a deeper understanding of their kinetic behavior and how they may be affected by deactivation.

To achieve high H_2 selectivity under APR conditions, the catalyst needs to promote the cleavage of C-C bonds over C-O bonds while facilitating the water-gas shift reaction to effectively eliminate adsorbed CO from the surface. Platinum and nickel have been recognized as highly active metals for reforming of oxygenates [78,151]. In this project, they have served as the primary elements for catalyst development, creating two main groups: Pt-based catalysts and Ni-based catalysts. To establish a basis for comparison, a benchmark catalyst provided by JM was included: Pt/C with 4.3%wt Pt loading, allowing for a thorough evaluation of the catalytic activity and being able to cross-reference the experimental results across the experimental facilities operating within the BIKE project (NTNU, JM and UDUR). The studied samples vary in metal loading and type of support utilized. Their activity was tested and evaluated through a feedback loop for potential changes that could improve their conversion to H_2. Factors such as synthesis methods, metal dispersion, molar ratios, particle size, and surface properties of the support were considered.

4.1.2.1 Ni-based catalyst

At BAS, Ni-based catalyst were developed in order to substitute noble metals and leverage the properties of nickel. Nickel is renowned for its high activity in aqueous phase reforming but is also associated with a significant selectivity towards methane formation [73]. To reduce the rate of methane production while preserving a high rate of C-C cleavage, the addition of Sn as a second metal in the system has been explored. Previous studies by Huber *et al*. [151,152] have demonstrated that the addition of Sn significantly decreases the rate of methane formation without hindering the production of H_2.

When subjected to the hydrothermal APR conditions, Ni-based catalysts are susceptible to particle growth [73] and metal oxidation, which can lead to loss of active metal sites

through leaching. The introduction of Sn to the catalyst system has the potential to enhance catalyst stability by forming Ni-Sn alloys, which may improve corrosion resistance [72].

This study involved investigating monometallic and bimetallic samples supported on $Ce(Zr)O_2$, with variations in Sn loading. A preliminary evaluation was conducted to choose a suitable catalyst support for the Ni-based catalysts. The activity of a catalyst during APR is intricately affected by both the metal and the inherent properties of the support [78]. Thus, after a careful consideration within the BIKE consortium, mixed oxide supports were selected. Catalysts supported on ZrO_2, Fe_3O_4 and CeO_2 has shown favorable activity in APR of ethylene glycol and methanol thanks to the promotion of the water-gas shift reaction, as one of the main reactions taking place during APR [153,154]. Mixtures of these supports have shown high stability and resistance towards coke formation, a desirable characteristic for the harsh conditions of APR. Hence, 27 %wt Ni catalysts supported on Ce-Fe and Zr-Fe mixed oxides were evaluated.

The Ce-Fe catalyst presents high EG conversion of 75.5%, but with only 4.6% selectivity towards H_2, with methane being the main component in the gas phase (51.3% mol). In the case of Zr-Fe, the catalyst shows lower conversion (15.3%) with higher selectivity towards H_2 (19.0%) and low methane production, with a methane yield below 0.8%. In the case of both catalysts, the solution after reaction had a reddish hue, possibly associated with Fe leaching into the aqueous solution, as has been observed also in previous research [155]. Hence, to take advantage of the promoting activity of Ce in Ni-based catalysts with the slightly higher selectivity of Zr, a mixed-oxide of Ce-Zr was selected as support to continue the screening process.

Once the $Ce(Zr)O_2$ support was selected, a comparison was conducted between two catalyst synthesis methods: Incipient wetness impregnation (IWI) and a template-assisted method (TAM). The catalysts synthesized using both methods contained 10%wt Ni and 5%wt Sn. No significant differences were observed between the two catalysts based solely on their catalytic activity. The IWI catalyst achieved 38.2% ethylene glycol conversion, while the TAM catalyst achieved a slightly lower conversion of 36.2%. Both catalysts showed methane selectivities of 5.5% and 4.1%, respectively, and identical H_2 selectivities of 26.3%. Due to its simplicity, the incipient wetness impregnation method was selected for the subsequent screening process.

Figure 4-1 provides an overview of the catalytic performance during APR of ethylene glycol at 270°C using catalysts with varying Sn loadings (ranging from 2.5%wt to 10%wt)

while maintaining a fixed 10%wt Ni content. The presence of Sn in the catalysts is observed to considerably suppress methane formation, with at least three times lower selectivity to methane. Furthermore, as the Sn loading increases, there is a noticeable decrease in ethylene glycol conversion. However, at a Sn loading of 5%wt, a higher selectivity towards H_2 is observed. This specific catalyst exhibits a significantly higher conversion to gas phase products than the other samples in the series, resulting in a higher yield of H_2.

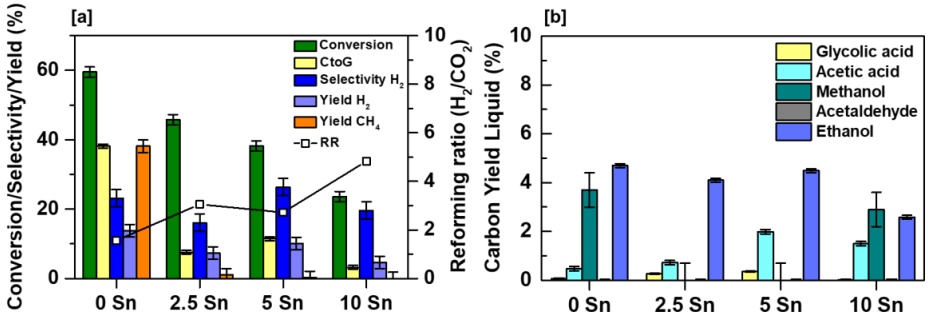

Figure 4-1. NiSn series - APR of 6 %wt ethylene glycol aqueous solution at 270 °C and 20 bar initial pressure in batch reactor (2 hours) [a] Conversion (%), H_2 selectivity (%) , H_2 yield (%), CH_4 yield (%) and reforming ratio (RR) [b] Carbon yield to liquid phase products (%).

In the liquid phase, the primary products observed are glycolic acid, acetic acid, methanol, and ethanol. The introduction of Sn led to a moderate decrease in the carbon yield towards liquid products (approximately 2-3% points less), while simultaneously increasing the formation of organic acids. However, the production of alcohols remained consistently similar among all the samples.

Although the catalysts are active under the evaluated conditions with EG conversion in the range of 60-23%, the total H_2 yield remains low (14-5%). Previous studies have explored the effect of addition of KOH in APR using Ni-based catalysts [73,156,157]. All these studies consistently demonstrate that the addition of KOH leads to an increase in APR activity of various polyols, such as glycerol, ethylene glycol, and sorbitol. Hence, KOH was added to the liquid feed (0.35M) to boost the H_2 production in APR of ethylene glycol.

Figure 4-2 illustrates a significant enhancement in H_2 yield, showing an increase of up to 4.9 times higher yield compared to the experiments conducted at an initial pH of 7. Additionally, the catalysts containing Sn exhibits a higher total carbon yield to the gas phase. The selectivities to CO and alkanes decrease considerably, while CO_2 becomes the

predominant carbon-based product in the gas phase, with selectivities exceeding 95% for the Sn-containing catalysts.

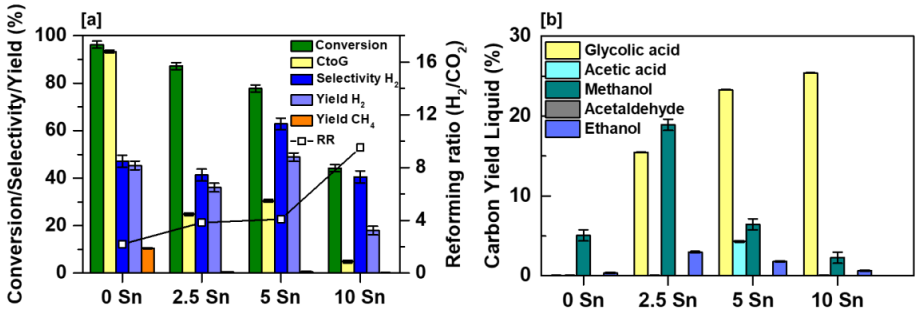

Figure 4-2. NiSn catalyst series - APR of 6 %wt ethylene glycol aqueous solution at 270 °C and 20 bar initial pressure including KOH (0.35M) in batch reactor (2 hours) [a] Conversion (%), H_2 selectivity (%) , H_2 yield (%), CH_4 yield (%)and reforming ratio [b] Carbon yield to liquid phase products (%).

The enhancement of the catalytic activity in presence of KOH is most likely related to an increase in the pH. As the pH of the solution increases, it creates an environment in which oxidation of Ni is less likely to occur. Thus, a larger fraction of metallic nickel is present at these alkaline conditions [73]. Additionally, KOH could inhibit CO methanation while facilitating the WGS reaction. Potassium could block the active sites (step sites) for methanation while KOH may induce dissociation of water necessary for WGS [156]. Finally, adding a base could lead to capture of CO_2, which may be reflected in the higher reforming ratios (H_2/CO_2) seen in experiments conducted with KOH present. The reforming ratio increases by roughly one third compared to those conducted at pH 7.

The carbon yield towards liquid products is higher in the presence of KOH by up to a factor of 7 for the samples containing Sn, while a slight reduction was observed for the monometallic Ni catalyst. The product distribution of the liquid phase for these experiments is rather complex, including a significant fraction of C1-C5 alcohols, aldehydes (isobutyl aldehyde), ketones (2-propanone, 3-butanone), and organic acids (acetic acid, glycolic acid). In Figure 4-2 [b], the most representative components present in the liquid phase are shown, where the production of glycolic acid becomes predominant, followed by methanol and ethanol.

Therefore, it can be suggested that the presence of KOH promotes reactions within the liquid phase, thereby providing diverse pathways in the APR mechanisms at high pH. These pathways may involve processes like dehydrogenation of ethylene glycol,

potentially triggering a rearrangement of the adsorbed species leading to the formation of organic acids. This notion aligns with the observations made by Zope *et al.* [158], who observed that selective oxidation of alcohols is facilitated in the presence of supported gold and platinum catalysts at high pH conditions. Their observations suggest a mechanism involving steps mediated by the solution and steps catalyzed by the metal.

Introducing Sn into a Ni-based catalyst reduced methane formation, leaving H_2 production unaffected, whereas added KOH augmented the activity of all catalysts within the series. The stability of the catalyst was assessed by metal leaching based on the nickel loading of the samples before and after the reaction. As seen in Table 4-1, the catalyst with 5% Sn loading is the most stable regarding Ni leaching during the aqueous phase reforming of ethylene glycol. Only 0.3% of nickel leached under standard conditions, while 9.3% leached under alkaline conditions, most likely due to alloy formation that stabilizes nickel. In contrast, the leaching for the other samples was more significant. The increased leaching at higher pH could be associated with the higher production of organic acids, leading to oxidation and leaching.

Table 4-1. Metal loading and metal leaching of the SnNi based catalyst before and after APR at 270°C and 20 bar initial pressure

Metal loading	**2.510 SnNi**	**510 SnNi**	**1010 SnNi**
Element	**Ni (%wt)**	**Ni (%wt)**	**Ni (%wt)**
Initial	10.6	8.5	9.8
Final pH7	9.3	8.5	8.8
Final pH14	9.9	7.7	7.4
Metal leaching [%] pH7	**12.9**	**0.3**	**9.9**
Metal leaching [%] pH14	**6.8**	**9.3**	**24.8**

Further investigations are underway at the Bulgarian Academy of Sciences (BAS), including comprehensive catalyst characterization. The objective is to gain deeper insights into the elements contributing to enhanced catalytic performance in aqueous phase reforming of ethylene glycol.

4.1.2.2 Pt-based catalysts

Previous studies have indicated that breaking C-C bonds on platinum surfaces is more readily than C-O bond cleavage following dehydrogenation steps of polyols in APR. This phenomenon contributes to platinum catalysts having notable selectivity to H_2 and high catalytic activity [53,159]. In this project, Pt-based catalysts were developed

collaboratively by NTNU and CNR, with the objective of enhancing catalyst activity by introducing a second metal while upholding the high H_2 selectivity.

Carbon materials as catalyst supports were selected as the focal point in the BIKE project for investigating Pt-based catalysts in APR. These materials are considered suitable supports for APR applications due to their hydrothermal stability, high specific surface area, resistance to acidic and basic environments and the potential to readily adjust their chemical properties through surface functionalization [81–83].

For the first evaluation phase in this project, Pt-based catalysts containing 3%wt Pt supported on carbon nanofibers (CNF-ox) were investigated. These catalysts were further modified by the addition of Mn (0.8%wt) and W (0.8%wt), including tungsten oxide (WO_3) and tungsten carbide (WC). The performance of these modified catalysts was compared with that of the monometallic Pt catalyst supported on CNF-ox and the benchmark catalyst supplied by JM consisting of 4.3 wt% Pt supported on a commercial carbon material derived from coconut shells. A summary of the APR results from these catalysts is outlined in Figure 4-3.

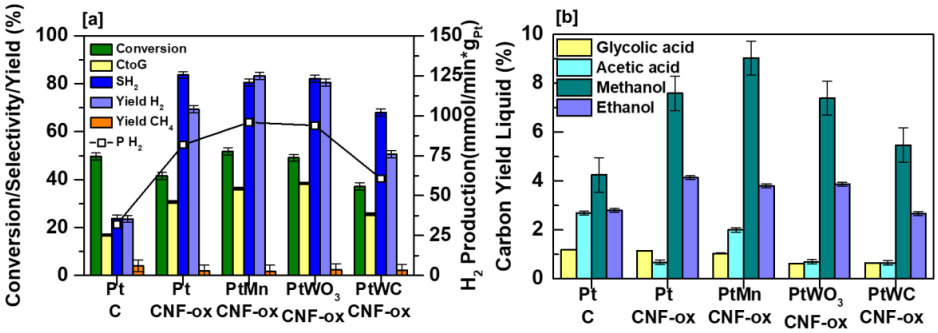

Figure 4-3. Pt-CNF series - APR of 6 %wt ethylene glycol aqueous solution at 270°C and 20 bar initial pressure in batch reactor (2 hours) [a] Conversion (%), H_2 selectivity (%) , H_2 yield (%), CH_4 yield (%) and H_2 production (mmol/min*g_{Pt}) [b] Carbon yield to liquid phase products (%).

The monometallic Pt-CNF-ox catalyst exhibited a relatively lower H_2 yield (69.3%) at 270°C, with the Mn-containing (83.3%) and WO_3-containing (80.5%) samples surpassing its performance. The bimetallic catalyst containing Mn showed the least methane yield overall, with particularly low selectivity towards alkanes in the gas phase (6.8%). Comparable patterns were observed among the studied catalysts regarding liquid-phase products, with methanol emerging as the predominant liquid by-product, followed by ethanol, acetic acid, and glycolic acid. The most significant formation of organic acids was

observed for the Pt/C and PtMn/CNF-ox samples, while the lowest carbon yield to liquid products was detected for the catalyst containing WC.

After the initial screening, a study into the Pt-Mn ratio was conducted using samples provided by CNR. These samples were supported on carbon black (Cvxc) and synthesized through the metal vapor synthesis (MVS) method [160]. This technique facilitates the creation of small and uniform particle sizes (1-2nm), thereby yielding a catalyst characterized by high Pt dispersion. The Pt loading was fixed to 2%wt while the Mn loading was varied based on the Pt:Mn molar ratio, including ratios of 3:1, 1:1, and 1:2. The APR results are presented in Figure 4-4.

The catalysts were examined for their performance in APR, and the catalyst with the lowest Mn content, represented by the Pt:Mn ratio of 3:1, exhibited highest activity with a hydrogen yield of 52.8%. As the amount of Mn increases, the hydrogen yield decreases, while the production of glycolic acid in the liquid phase increases from a carbon yield of 0.04% to 0.38%, as the Pt:Mn ratio changed from 3:1 to 1:2. This pattern reinforces findings from our earlier screening, suggesting that the presence of Mn plays a role in facilitating the dehydrogenation reaction and subsequent rearrangement of adsorbed species, leading to the formation of organic acids in APR. Moreover, Mn might also influence the C-O cleavage pathway, promoting the generation of liquid products to a certain extent. Previous studies have shown that adding Mn increases the concentration of Lewis acid sites, which is a catalyst feature promoting C-O bond cleavage in reforming of polyols [65].

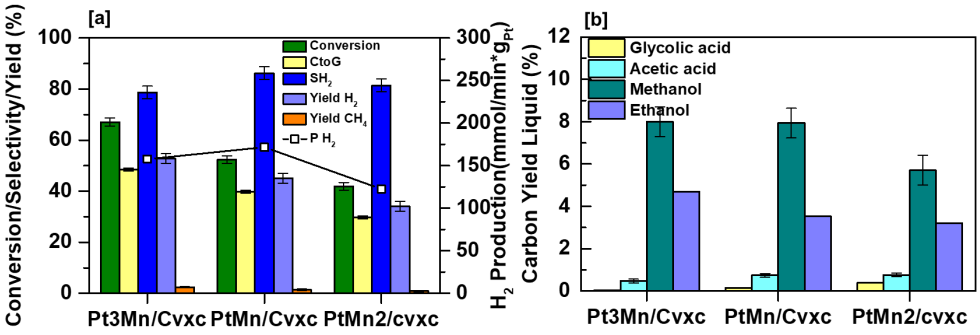

Figure 4-4. PtMn Cvxc series - APR of 6 %wt ethylene glycol aqueous solution at 270 °C and 20 bar initial pressure in batch reactor (2 hours) [a] Conversion (%), H_2 selectivity (%) , H_2 yield (%), CH_4 yield (%) and H_2 production (mmol/min*gPt) [b] Carbon yield to liquid phase products (%).

During this phase, an examination of catalyst deactivation was conducted. In the context of APR, a prevalent cause of catalyst deactivation arises from the oxidation of the active phase, subsequently leading to metal leaching due to the low pH developed in the reaction mixture by the presence of organic acids [54]. The metal loading of the catalyst series (PtMn/Cvxc) was measured before and after APR. Notably, only negligible quantities of Mn were observed in all catalysts post-reaction, indicating significant leaching of Mn into the liquid phase (~ 97%) during the two-hours of aqueous phase reforming of ethylene glycol. In contrast, the stability of Pt within the catalysts is evident, as it is retained throughout the experiments, with less than 1% metal leaching for all the catalyst in the series.

Another aspect evaluated in this preliminary test is the nature of the carbon support. In this case, two different carbon materials were evaluated as supports for bimetallic catalysts with a Pt:Mn molar ratio of 3:1. The catalyst supports were carbon black (CVXC) and carbon nanofibers (CNF). A lower catalyst loading of 160 mg was employed in the batch APR experiments, in contrast to 200 mg used in prior studies. The catalyst supported on carbon nanofibers (CNF) demonstrated superior performance under the investigated conditions (270°C). This specific catalyst achieved a hydrogen yield of 53.8%, accompanied by an EG conversion of 57.8% and a methane yield of 0.66%. Conversely, the catalyst supported on carbon black displayed slightly lower values, with a hydrogen yield of 43.4%, EG conversion of 49.8%, and methane yield of 1.1%.

In liquid-phase reactions, the influence of mass transfer limitations tends to be more significant compared to gas-phase reactions. Within this context, the pore structure of the support has an important role in APR, as it facilitates the diffusion of reactants and products across the catalyst matrix [61]. Thus, the observed outcomes can be attributed, at least in part, to the structural differences of the carbon materials. Carbon black exhibiting a higher micro-pore volume (0.028 cm^3/g) compared to CNF (0.006 cm^3/g) might affect the diffusion of ethylene glycol towards the active sites situated within the micropores of the carbon support, or it might constrain the diffusion of liquid byproducts. The liquid products may undergo subsequent reactions leading to the formation of alkanes, as seen in the higher production of methane for the Cvxc catalyst.

An additional important aspect of the CNF, particularly platelet CNF, is the presence of edges in the graphite planes. These edges can serve as suitable sites for anchoring and stabilizing platinum nanoparticles and favor metal-support interactions involving electron transfer between platinum and the carbon support [161]. Such interactions

typically improve the catalytic activity, contributing to the overall performance of the catalyst.

Within this framework, further investigation was directed towards Mn, chosen as the secondary metal alongside Pt, with CNF as the selected support. The challenges associated with Mn leaching under APR conditions will be addressed in section 4.2, where modifications of the support were explored to enhance the stability of nanoparticles while upholding a high level of activity and selectivity towards hydrogen production.

4.1.3 Aqueous phase reforming over non-carbon-supported catalysts

This section presents a study on an alternative kind of support, acknowledging the limitations that arise when using carbon materials as catalyst supports. The relatively low density and insufficient mechanical strength constraint the application of pelletized carbon-based catalyst at industrial scale. Typically, carbon supports experience fragmentation, resulting in creation of fines that increase pressure drop when utilized in a fixed-bed reactor [162,163].

Various supports have been investigated in the context of APR, considering the required stability under hydrothermal conditions. Guo *et al.* [164] studied the effect of the basic properties of supports on hydrogen production in APR. Different mixed-oxides were evaluated: MgO, Al_2O_3, CeO_2, TiO_2 and SiO_2, observing that APR of glycerol was more favorable over more basic supports such as MgO and Al_2O_3 for Pt-based catalysts. However, poor stability of MgO was observed due to the formation of magnesium hydrate and carbonate, causing fragmentation and subsequent increase in pressure drop.

In the search for a basic support suitable for APR conditions, mixed oxides of magnesium and alumina (MgO-$MgAl_2O_4$) were synthesized by flame spray pyrolysis (FSP) with an excess of MgO (Mg/Al ratio of 3) and studied in APR of ethylene glycol, including Pt and Mn. Incorporating alkaline earth metals or metal oxides, like MgO and CaO, onto an Al_2O_3 support is a commonly utilized strategy to enhance the basicity of catalysts [165,166], a desired property in APR to enhance the H_2 formation through the WGS reaction. In the synthesized catalyst, the molar ratio of Pt and Mn was varied while maintaining a constant loading of 1%wt platinum. In Figure 4-5 the XRD patterns of the samples are presented, where the reflections characteristic of the MgO, $MgAl_2O_4$ and platinum are observed.

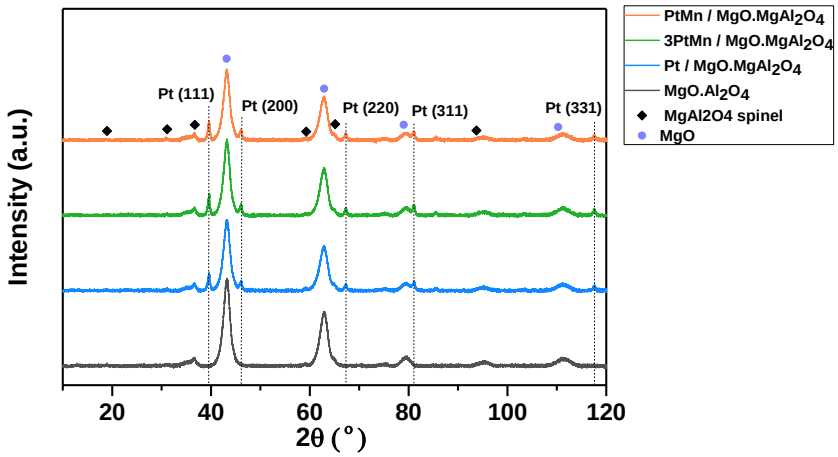

Figure 4-5. X-ray diffraction patterns of the catalysts supported on MgO-$MgAl_2O_4$ syntheiszed by FSP.

The average Pt crystallite size estimated from the diffraction patterns of PtMn/MgO-$MgAl_2O_4$ catalysts with different Mn content are summarized in Table 4-2. The crystallite size is relatively comparable among the synthesized samples. However, considering the low Pt loading, a smaller crystallite size was anticipated. This might result from the synthesis method used, since the composition and properties of the materials obtained by double flame spray pyrolysis are susceptible to the intersection distance of the flames. The distance depends on the space between the burner nozzles and the angles at which they are arranged. Hence, if the distance is not optimized, lower temperatures at the intersection of the flames due to a longer distance could promote aggregation between the formed particles [138].

Table 4-2. Average crystallite size, metal loading, and metal leaching of catalysts synthesized by FSP.

Catalyst	Av crystallite size (nm)	Metal loading (%wt)		Metal leaching (%)	
		Pt	Mn	Pt	Mn
Pt/MgO-$MgAl_2O_4$	14	0.96	-	-	-
3PtMn/MgO-$MgAl_2O_4$	15	0.99	0.15	-	-
PtMn/MgO-$MgAl_2O_4$	13	0.91	0.43	-	-
Pt/MgO-$MgAl_2O_4$ spent	-	0.69	-	28.0	-
3PtMn/MgO-$MgAl_2O_4$ spent	-	0.72	0.07	27.3	58.4
PtMn/MgO-$MgAl_2O_4$ spent	-	0.74	0.18	18.2	49.7

The catalysts were tested in the context of aqueous phase reforming of ethylene glycol at 270°C. A summary of the results is presented in Figure 4-6. The catalysts containing Mn exhibit superior activity compared to the monometallic Pt catalyst. No significant

differences are observed in the gas phase product distribution across the range of Mn loading, reflecting high H_2 yields for both catalysts studied (~70%). Similarly, the liquid phase product distribution is comparable for the catalyst series, exhibiting methanol as the main product followed by ethanol, acetic acid, and glycolic acid.

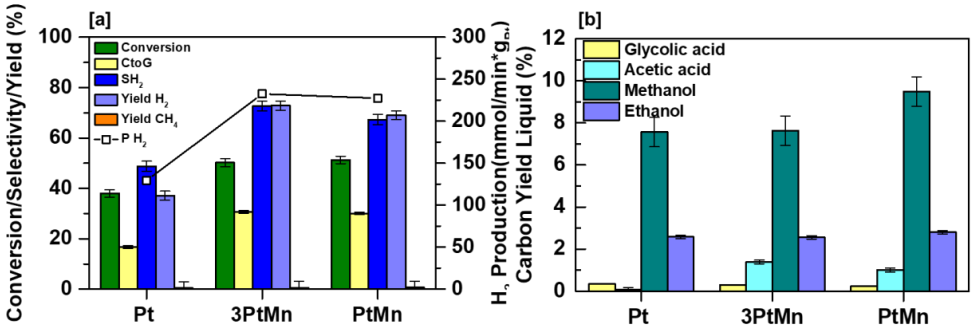

Figure 4-6. MgO-$MgAl_2O_3$ series - APR of 6 %wt ethylene glycol aqueous solution at 270°C and 20 bar initial pressure in batch reactor (2 hours) [a] Conversion (%), H_2 selectivity (%) , H_2 yield (%), CH_4 yield (%) and H_2 production (mmol/min*g_{Pt}) [b] Carbon yield to liquid phase products (%).

Increasing the Mn loading for the Pt-based catalysts seems to promote H_2 production. Moreover, the presence of Mn correlates with a rise in the concentration of acetic acid in the liquid phase. This suggests that Mn influences certain reaction pathways that facilitates the formation of organic acids, such as the dehydrogenation of EG and the subsequent rearrangement of adsorbed species. Regarding the basic support used for this catalyst series, trace levels of CO were identified in the gas phase, with molar concentrations remaining below 0.066%. These outcomes can be attributed to the pronounced water-gas shift activity, which effectively converts CO generated from ethylene glycol reforming into hydrogen and CO_2. Furthermore, relative to the series using CNF-ox as support, less formation of organic acids and methane is observed. The CNF-ox are known to contain acidic groups on the carbon surface after the treatment with nitric acid [167]. Hence, these acidic sites could promote the formation of methane and organic acids during aqueous phase reforming [53].

Based on the evaluation of the catalysts after the APR reaction (Figure 4-6), Pt and Mn leached out from the MgO-$MgAl_2O_4$ support. the leaching is more pronounced for Mn, with 50-58% leaching out and less for Pt with 18-28%. The interactions between the support and the metal particles seem not strong enough to stabilize the particles at the demanding hydrothermal conditions characteristic of aqueous phase reforming. Therefore, despite

presenting high activity at the examined conditions, the catalysts are susceptible to deactivation by metal leaching during aqueous phase reforming of ethylene glycol.

4.1.4 Key findings

In the screening section, it was observed that the introduction of Sn to a Ni-based catalyst hinders methane formation and enhances the activity in aqueous phase reforming of ethylene glycol. The optimal loading of 5% Sn and 10% Ni was found to enhance hydrogen selectivity when supported on ceria-zirconia mixed oxides. Even though SnNi-based catalysts displayed activity at a pH of 7 during APR (with conversions ranging from 30% to 60%), the selectivity towards H_2 remained modest, favoring the formation of liquid phase products. The incorporation of KOH boosted the catalyst activity, resulting in a significantly higher H_2 yield. For Pt, it was noted that the addition of Mn improves the catalytic activity, contributing to a higher hydrogen yield. The optimum molar ratio between Pt and Mn has been established at 3:1. However, minimal difference was observed for the catalyst having a Pt:Mn ratio of 1:1.

Noticeable differences between the metals were observed: The catalysts containing Pt displayed high selectivity towards H_2 (>80%), while the nickel-based catalysts exhibited high activity along with a moderate H_2 selectivity (ranging from 40% to 60%). These distinctions emphasized the capacity of Pt to favor C-C bond cleavage and the notable high activity of Ni, favoring side reactions that consume H_2, such as methanation.

The selection of the supports mainly influenced the dispersion, diffusion of reactants and products across the catalyst structure and either facilitated or hindered acid-catalyzed dehydration reactions. Hence, both the texture and morphology of the support play a role in the catalyst activity, along with the chemical properties. The basic nature of the supports could be associated with enhancement of the WGS reaction activity leading to an increase in hydrogen production. Additionally, challenges from hydrothermal conditions were particularly visible in the case of MgO-$MgAl_2O_4$ and Fe-containing Zr-Ce supports, where severe metal leaching was observed during the rection. Therefore, to address these issues, supports such as carbons and ceria-zirconia mixed-oxides seem to demonstrate better stability at the demanding reaction conditions. The following section presents a more in-depth study of the interaction between Pt and Mn on CNF as the support material.

4.2 Nitrogen-containing carbon nanofibers as supports for bimetallic Pt-Mn catalysts in aqueous phase reforming of ethylene glycol.

The work presented in this section involves studies into the addition of Mn as a second metal in Pt-based catalysts supported on CNF. This includes findings discussed in Paper I, which involve nitrogen-doped carbon nanofibers. Additionally, a separate segment explores the in-situ XAS characterization of Pt-Mn bimetallic catalysts during aqueous phase reforming of ethylene glycol.

Paper I delve into the influence of incorporating Mn into Pt-based catalysts and comparing the performance with corresponding monometallic Pt catalysts. In addition, the effect of nitrogen surface functionalization of platelet CNF is explored, relying on characterization techniques to understand and identify the interactions between the elements in the catalytic system. Mn recognized as an unstable promoter under APR conditions, was selected to investigate whether modifying the support surface coupled with its interaction with Pt could effectively enhance the stability of Mn at APR reaction conditions.

The paper is divided into the following sections:

1. Catalyst synthesis and characterization
2. Aqueous phase reforming at batch reaction conditions
3. Aqueous phase reforming at continuous flow conditions
4. Characterization of spent catalysts

4.2.1 Catalyst synthesis and characterization

The surface of the CNF was modified by post-treatments: Acid, heat or gasification-assisted heteroatom doping [101] as described in section 3.2 to introduce oxygen functional groups (CNF-ox), remove unstable oxygen groups produced by the acid treatments (CNF-HT) such as carboxylic acids and anhydrides [168] or introduce nitrogen functional groups on the surface of the carbon nanofibers (N-CNF).

Characterization by BET and XPS of the platelet CNF aided in determining the textural properties of the carbon materials and identifying the surface functional groups contained in the carbon support. The CNFs primarily exhibit mesoporous characteristics, with only slight variations in surface area, with a 15% decrease after the nitrogen

functionalization. The nitrogen content in N-CNF is 1.9%at, while the oxygen content for CNF-ox and CNF-HT is 3.5%at and 1.7%at, respectively.

Following the deposition of platinum and manganese through incipient wetness impregnation, an assessment was conducted on Pt dispersion, particle size, and metal loading. An overview of the results from various characterization techniques is displayed in Table 4-3. From the table, it is noted that the introduction of Mn leads to a reduction in the CO uptake of the catalysts, resulting in a decrease in platinum dispersion. This phenomenon has been observed in previous studied by Jain *et al.* [169] , attributing the decline in CO uptake to a physical obstruction caused by Mn covering Pt atoms.

Table 4-3. Pt dispersion, metal loading and average particle size determined by CO chemisorption, MP-AES and XRD.

Catalyst	CO uptake ($\mu mol\ g^{-1}$) [a]	Pt dispersion (+/- 1) [a]	Metal loading (±0.1 %)[b]		Pt particle size (nm) [a]	Crystallite size (nm)[c]
			Pt	Mn		
Pt/CNF-ox	48.5	39	2.9		3	27
Pt/CNF-HT	72.4	50	2.8	-	2	7
Pt/N-CNF	52.1	40	2.5	-	3	-
PtMn/CNF-ox	47.3	37	2.9	0.8	3	22
PtMn/CNF-HT	45.9	34	2.6	0.8	3	16
PtMn/N-CNF	46.0	35	2.6	0.8	3	-

[a] CO chemisorption

[b] MP-AES

[c] XRD using the Scherrer equation

Similarly, the presence of oxygen containing-groups on the carbon surface facilitated aggregation of Pt when employing an anionic precursor such as $Pt(Cl_6)^{-2}$, leading to a reduction in the CO uptake of the catalyst. This effect is more pronounced on the support featuring a higher oxygen content (CNF-ox). Consequently, this led to a catalyst composition where a significant fraction of Pt nanoparticles displayed fine dispersion on the surface, alongside another fraction of larger particles observed in STEM images and XRD patterns. Conversely, it was suggested that the presence of nitrogen functional groups, such as pyridinic groups, serve as anchoring points for the Pt nanoparticles, resulting in finely dispersed Pt nanoparticles on the surface of the supports, as observed in previous studies [170,171].

To closely examine the intricate interactions between the metal particles and the carbon supports, XPS analysis was conducted focusing on the Pt $4f_{7/2}$ region, presented in Figure 4-7. Previous research has established that electron-withdrawing nitrogen species cause a strong donor-acceptor interaction with Pt nanoparticles. This interaction leads to a

decrease in the Pt electron density resulting in a positive shift in Pt binding energy [113,172,173].

In the case of the monometallic catalyst investigated in this study, no apparent shift in the binding energy of Pt was observed. The nitrogen content on the support (1.9% at) is most likely too low to give a significant effect on the electron density of platinum. Nonetheless, when Mn was present in the samples, a significant shift to higher binding energy for the Pt species was observed for the PtMn/CNF-HT and PtMn/N-CNF catalysts, with a larger shift in the sample containing N species (+ 1.5 eV).

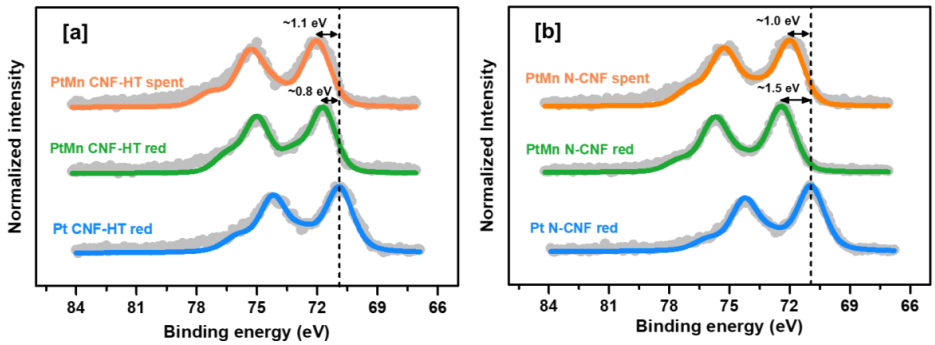

Figure 4-7. Pt 4f7/2 spectra of [a] Pt CNF-HT , PtMn CNF-HT catalysts after reduction ex-situ and spent PtMn CNF-HT after APR [b] Pt N-CNF, and PtMn N-CNF catalysts after reduction ex situ and spent PtMn N-CNF-HT after APR.

These findings suggest that the effect on the electronic state of Pt is not solely due to the presence of Mn [174] as seen in the PtMn/CNF-HT catalyst, but also arises from the nitrogen groups located on the surface of the carbon support, leading to a further decrease in the electron density of Pt.

4.2.2 Aqueous phase reforming at batch reaction conditions

An evaluation of the synthetized catalyst in ARP of ethylene glycol was carried out at 225°C in a batch reactor. The catalytic activity and carbon yield to the liquid products are presented in Figure 4-8 and Figure 4-9. In the gas phase, the primary products were H_2, CO_2, and CH_4. Meanwhile, the liquid phase was dominated by methanol, ethanol, acetic acid, and glycolic acid.

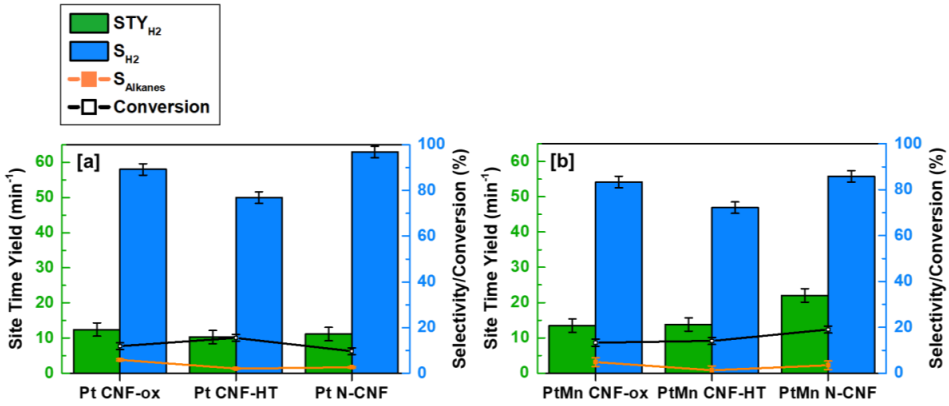

Figure 4-8. APR of 6 %wt ethylene glycol aqueous solution at 225°C and 20 bar initial pressure in batch reactor. Catalytic conversion of EG, H_2 site time yield (STY_{H2}), H_2 and alkane selectivities for the [a] monometallic Pt catalysts. [b] bimetallic PtMn catalysts. The error bars represent the standard deviation of the experiments.

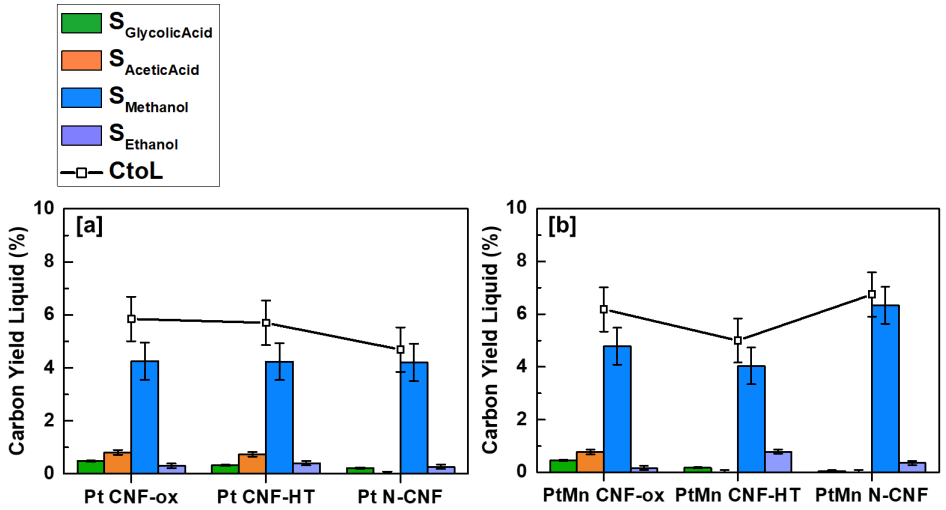

Figure 4-9. APR in batch reactor of 6 %wt ethylene glycol aqueous solution at 225°C and 20 bar initial pressure. Carbon yield to main liquid products and total conversion of carbon to liquids (CtoL) of the [a] monometallic Pt catalysts [b] bimetallic PtMn catalysts. The error bars represent the standard deviation of the experiments.

A prevalent patter observed among the studied catalysts is the high H_2 selectivity (>80 %) coupled with minimal alkane formation (<5%). Minor deviations in activity and selectivities was observed for the various surface functionalization of the CNF in the monometallic samples. A reduction in the formation of acetic acid was noted for the catalyst containing N species. This implies that the likelihood of dehydrogenation and

subsequent rearrangement of adsorbed species, leading to the formation of minor organic acids during APR [53], is less favorable in the presence of N species on the carbon surface

With the introduction of Mn, an increase in H_2 site time yield can be seen for all the catalysts, as suggested in previous studies that Mn facilitates the activation of polyols, such as glycerol, leading to higher H_2 production rates [65]. However, clear indications of the positive impact of N-doping can be seen in the bimetallic samples, resulting in a high H_2 selectivity of 95.8% and a H_2 site time yield of 22 min^{-1} for PtMn N-CNF. Based on these results, it appears that there is a correlation between the increased activity and the strong interaction between Pt-Mn and the N species on the surface of the CNF. This was observed through XPS analysis, which showed a shift in the Pt binding energy, signaling a charge transfer from Pt to Mn and nitrogen species on the CNF. Therefore, the increased catalytic activity of PtMn/N-CNF can be attributed to the presence of electron-deficient Pt on the CNF surface.

To assess the stability of the catalyst under the harsh hydrothermal APR conditions and when exposed to organic acids that decreased the pH of the solution from nearly neutral to pH 3-4 during APR, the metal leaching from the catalysts was evaluated. A comparison of the metal loading of the reduced and spent catalysts demonstrated that approximately 95-97% of Mn leached out during 2 hours of APR, demonstrating that the functionalization of the carbon support was not sufficient to stabilize the Mn species. Pt demonstrated a stable behavior with no significant leaching observed (<1%).

4.2.3 Aqueous phase reforming at continuous flow conditions

The most active catalysts were evaluated under continuous flow conditions. This eliminates any issues that might arise from using batch processes, such as the accumulation of products in a closed system that can detriment the stability of the catalyst, mainly when organic acids are produced. In addition, the accumulation of gas-phase products increases the total pressure in the system, which can have a negative effect on the APR activity [175].

The catalysts were tested at 225°C and 30 bars for 20 hours on stream to reach steady-state conditions. An overview of the catalytic activity of the catalysts supported on CNF-HT and N-CNF is presented in Figure 4-10. Consistent with the outcomes of the batch experiments, the bimetallic catalysts present higher catalytic activity. Among the catalysts studied, PtMn/N-CNF shows the highest H_2 site time yield (15.8 min^{-1}) with lowest production of alkanes. These findings align with comparable studies conducted on Pt-

based catalysts. Huber *et al.* [60] reported TOF_{H2} values in the range of 7-11 min^{-1} in APR of ethylene glycol for bimetallic catalysts such as PtNi, PtCo and PtFe exhibiting higher activity than their monometallic counterparts.

The carbon yield towards liquid products is relatively low, within a range of 3% to 6% of the total carbon converted (Figure 4-10 [d]). The liquid phase mainly consisted of methanol and ethanol as by-products, without any presence of organic acids. Adding Mn and nitrogen species to the catalytic system enhanced the catalyst performance with a minor impact on the distribution of the products, observing similar trends in selectivities towards gas and liquid by-products. The product distribution correlates with the reaction pathways initially reported by Dumesic *et al.* [23], favoring C-C bond cleavage over C-O bond cleavage, resulting in high H_2 selectivities [23,53,175,176].

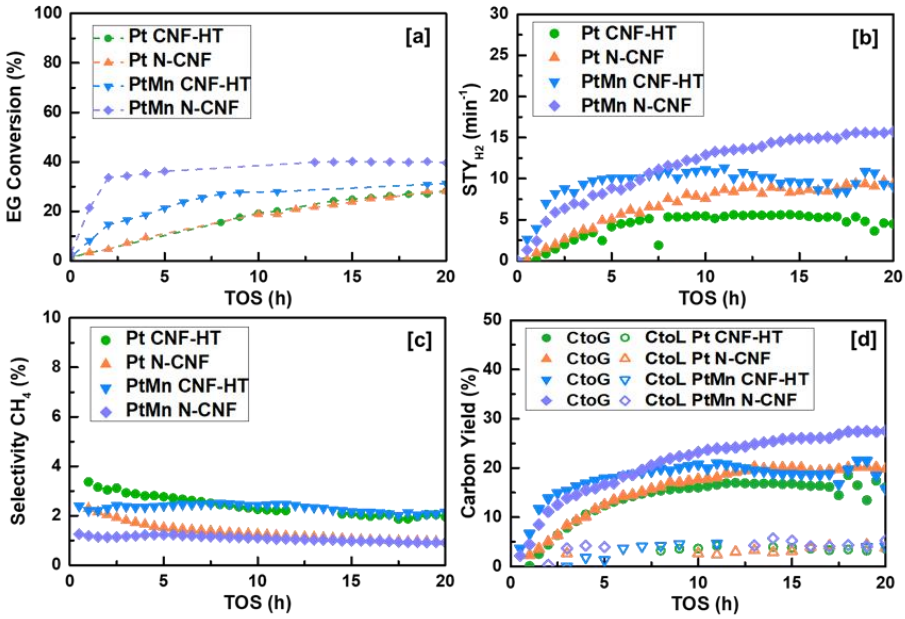

Figure 4-10. APR of ethylene glycol (6%wt) at 225°C, 30 bar and WHSV=$2h^{-1}$. Evolution of [a] Ethylene glycol conversion (%) [b] H_2 site time yield (min^{-1}) [c] Selectivity to CH_4 [d] Carbon yield to liquid phase and gas phase (%) with time on stream (TOS).

4.2.4 Characterization of spent catalysts

Evaluation of the spent catalysts after 20 hours on stream was conducted to identify potential causes of deactivation of the catalysts. A slight degree of sintering was detected, observed by the decrease in the platinum dispersion measured by CO chemisorption. The

decrease was more pronounced in the catalyst supported on CNF-HT, with approximately 5% reduction in the Pt dispersion for both mono and bimetallic catalysts. The decline was almost negligible (1% -3%) for the catalysts supported on N-CNF, highlighting the ability of nitrogen-doped supports to stabilize the Pt nanoparticles even at harsh hydrothermal conditions, as presented in Figure 4-11.

Significant Mn leaching was detected in the case of Mn-containing samples, with a slightly lower degree of leaching for PtMn/N-CNF estimated at 89± 0.1% in comparison to PtMn CNF-HT with 97.1± 0.1%. No significant leaching was detected for Pt, with typical leaching values lower than 0.01%.

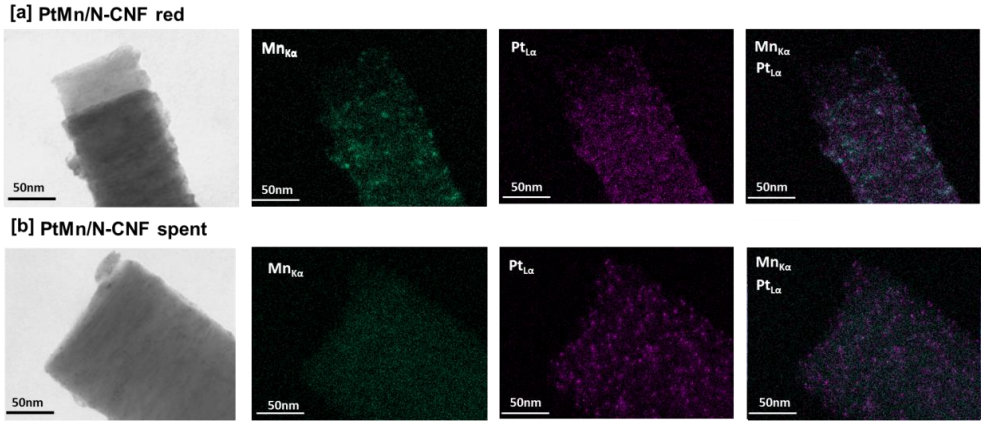

Figure 4-11. STEM images and EDX elemental maps of [a] PtMn/N-CNF reduced and [b] PtMn/N-CNF after 20 hours of APR at 225°C. EDX maps of Mn, Pt and the overlay of both element signals.

Even with the substantial loss of Mn during the reaction, the catalytic activity remains stable, as shown in Figure 4-10. Additionally, from the Pt 4f $_{7/2}$ XPS spectra of the spent bimetallic catalyst (Figure 4-7 [b]), a shift to higher binding energies of 1eV is still noticeable in comparison to the monometallic catalyst. Previous studies suggest that a minor amount of Mn in the catalyst plays a role in its catalytic activity [65]. Hence, after Mn leaching, the remaining Pt particles expose low coordinated surface atoms that may act as preferential sites for aqueous phase reforming of ethylene glycol.

4.2.5 In-situ XAS studies of PtMn catalysts

In order to gain a better understanding of the condition of the catalyst throughout the reaction, the progression of the PtMn/CNF-HT catalyst was followed by conducting *in-situ* XAS studies at the Pt L_3 edge and Mn K edge during aqueous phase reforming of ethylene glycol. Detailed comparison of the Pt L_3 edge XANES spectra of PtMn CNF-HT before and

after catalyst reduction at 300°C and after APR is shown in Figure 4-12 [a]. In the initial stages, the catalyst is partially oxidized, but after reduction, the spectrum closely resembles that of the Pt foil. This observation serves as a clear indicator that Pt becomes fully reduced in the presence of H_2 at high temperatures. Additionally, there are no noticeable variations observed directly from XANES spectra before and after aqueous phase reforming.

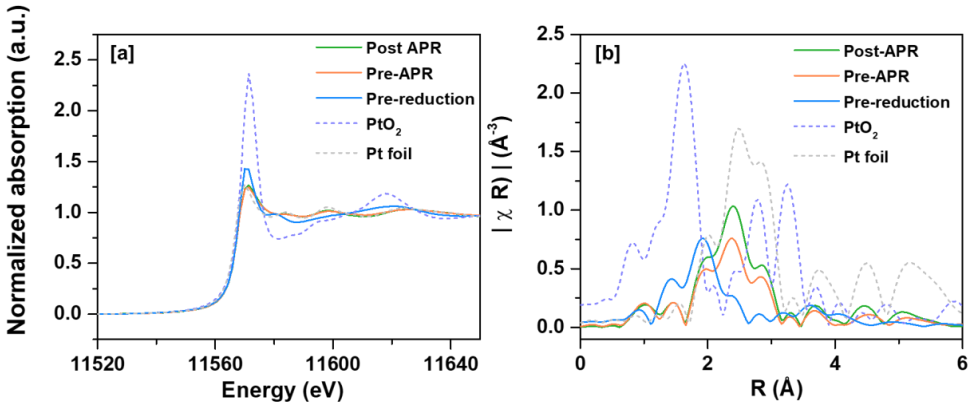

Figure 4-12. XAS results at Pt L_3 edge of PtMn CNF-HT after reduction, before and after APR at 225°C and 30 bar (WHSV = $2h^{-1}$). (a) XANES spectra; (b) Fourier transforms of the EXAFS spectra (R space).

The Fourier transforms of the XAS spectra (R space) are shown in Figure 4-12 [b], in which the nearest Pt-Pt peak position of the reduced and spent catalysts shifts to a shorter radial distance in comparison to the Pt foil (2.77 Å), which is consistent with the formation of bimetallic Pt-Mn bonds. Hence, EXAFS fitting of the Pt L_3 edge in k space was employed to determine whether there is a close proximity of Mn to Pt atoms.

The EXAFS fitting results of the Pt L_3 edge data from before and after the reaction are shown in Table 4-4 and Figure 4-13. Following the APR reaction, a slight increase in the Pt-Pt coordination number is observed, aligning with a decrease in dispersion as indicated by CO chemisorption (Table 4-3). This trend indicates a minor level of sintering of the metal particles. A small coordination number is estimated for Pt-Mn before the reaction, which after the reaction becomes almost negligible by the large uncertainty of the obtained value. However, upon analyzing the radial distances between the metals, it was observed that the Pt-Pt distance was shorter before the reaction compared to after. After APR, the Pt-Pt bond distance closely approximates that of the Pt foil, suggesting a change in the local environment of Pt attributed to Mn leaching. Thus, the initially present shorter radial distances and larger Debye-Waller type factor could be associated with Mn closely

located to Pt. In contrast, larger Pt-Pt bond distances reflect a decrease in the presence of Mn after APR.

Table 4-4. EXAFS fitting results for the PtMn CNF-HT catalyst at the Pt L_3 Edge[a]

Catalyst	Shell	ΔEo (eV)	CN	R (Å)	σ2 (Å)	R-factor
PtMn CNF-HT red	Pt-Pt	4.33 ± 1.55	8.42	2.695	0.0106	0.049
	Pt-Mn		0.78	2.711	0.0013	
PtMn CNF-HT spent	Pt-Pt	7.47 ± 1.13	9.87	2.755	0.0089	0.056
	Pt-Mn		0.92	2.696	0.0082	
	Pt - Pt		4.25	3.892	0.0104	

[a] Reaction conditions: APR of ethylene glycol at 225 °C and 30bar, WHSV = $2h^{-1}$. The fitting was conducted in k space (3<k<12).
Estimated accuracy in coordination numbers, CN: ± 10-20%. Interatomic distance R: ± 0.02Å.

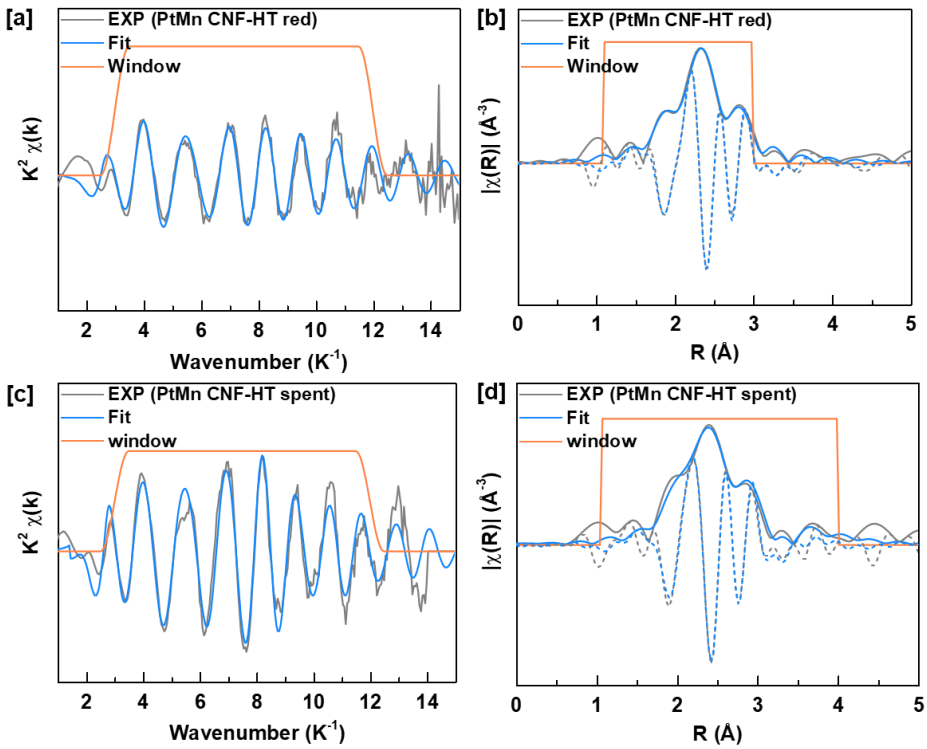

Figure 4-13. Pt L_3-edge EXAFS [a] Fit of the k^2 weighted EXAFS spectra and [b] corresponding Fourier transforms of PtMn/CNF-HT after catalyst reduction. [c] Fit of the k^2 weighted EXAFS spectra and [c] corresponding Fourier transforms of PtMn/CNF-HT after APR of ethylene glycol at 225°C and 30 bars (WHSV = $9h^{-1}$)

In order to provide a visual indication of the Mn leaching during APR, the PtMn CNF-HT catalyst was monitored by collecting Mn K edge XANES data during aqueous phase

reforming of ethylene glycol. The *in-situ* XANES spectra at the start and end of the reaction are shown in Figure 4-14. Given the low Mn concentration, the measurements were conducted in fluorescence mode. From the spectra, a decrease in the edge step of Mn can be observed, which is linked to a decrease in the Mn content in the catalyst. This finding is consistent with metal leaching analysis and the Pt L_3 EXAFS data interpretation. Hence, after aqueous phase reforming, only a minor fraction of the initial content of Mn remains in the catalyst (~5%).

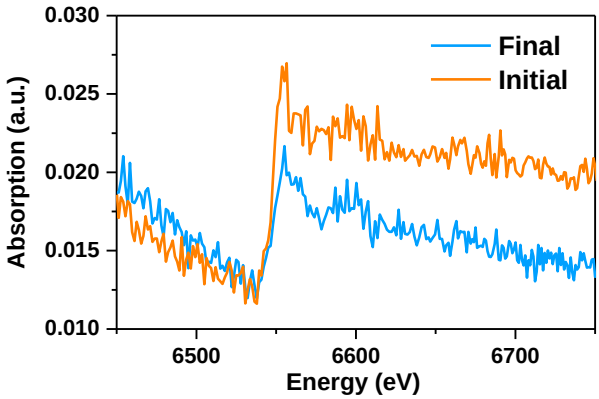

Figure 4-14. Mn K edge XANES spectra of PtMn/CNF-HT at start and end of APR of ethylene glycol at 225°C, 30 bar and $2h^{-1}$ WHSV.

4.2.6 Key findings

In this section, the interactions between the Pt-based catalysts with the addition of Mn as the second metal, and with the N and O surface functional groups on the carbon supports were studied in the context of aqueous phase reforming. PtMn bimetallic catalysts supported on N-doped carbon nanofibers exhibited good performance in aqueous phase reforming of ethylene glycol, with H_2 site time yield of 15.8 min^{-1} at 225°C and 30 bar pressure. It was concluded that both surface nitrogen species on the CNF support and manganese loading influenced catalytic activity. This activity enhancement is attributed to metal-support and metal-metal interactions, decreasing Pt electron density, and promoting H_2 formation.

Significant Mn leaching (up to 97±0.1%) was detected after 20 hours of continuous-flow APR. However, no significant impact was observed on the catalyst performance, indicating that a small fraction of Mn effectively enhances the catalytic activity of Pt.

The next section moves on to consider the impact of various dopants of the carbon nanofibers on Pt-based catalysts. The distinct characteristics of each heteroatom introduce novel features to the catalytic system, which could either strengthen or hinder the activity in aqueous phase reforming of ethylene glycol.

4.3 Aqueous phase reforming over platinum catalysts on doped carbon supports: Exploring platinum-heteroatom interactions

This research aims to investigate the impact of the local platinum environment in Pt-based catalysts on the catalytic activity in aqueous phase reforming of ethylene glycol. Modification of the platinum environment is achieved by introducing heteroatoms such as oxygen, nitrogen, sulfur, phosphorous, and boron into the carbon support. The heteroatoms induce changes in the electronic and physical interactions between the carbon matrix and the supported metal, subsequently leading to observable variations in catalytic activity and selectivity.

To gain deeper understanding of these interactions, a combination of in-situ X-ray absorption spectroscopy (XAS) and multivariate curve resolution alternating least squares analysis (MCR-ALS) was employed. These studies provided insight into the platinum oxidation states and the specific platinum species that evolve throughout the course of the aqueous phase reforming of ethylene glycol. This section relates to the content covered in Paper II and is subdivided into the following topics:

1. Catalyst synthesis and characterization
2. Aqueous phase reforming of ethylene glycol
3. *In-situ* characterization during aqueous phase reforming of ethylene glycol
4. Effect of carbon doping

4.3.1 Catalyst synthesis and characterization

The carbon nanofibers were synthesized by chemical vapor deposition as exemplified in section 3.1. Afterward, a nitric acid treatment was employed to eliminate the synthesis catalyst from the carbon structure and introduce oxygen functional groups on the surface (CNF-ox). This was followed by various additional treatment to incorporate desired heteroatoms in the carbon surface.

Inert atmosphere was utilized for a high-temperature treatment to lower the oxygen content of the support and remove unstable oxygen functional groups, resulting in CNF-HT [177]. To incorporate N, P, and S functional groups, the gasification-assisted heteroatom doping method (GAHD) [15] was employed. This involved subjecting CNF-ox

to a gasification agent at elevated temperatures in the presence of a gaseous source of heteroatoms (refer to section 3.3). The synthesis of B-CNF was achieved through wet-impregnation [135], involving a two-hour contact between the CNF-ox and a boron precursor solution at moderate temperatures (80°C). After successfully synthesizing the doped support, the catalysts were prepared using incipient wetness impregnation.

Characterization of the doped CNF by nitrogen physisorption and Raman spectroscopy demonstrated limited impact on the carbon texture and structure, with a heteroatom doping level of approximately 2%at (Figure 4-15 [f]). A decrease in the specific surface area was noticed in N-CNF , B-CNF, and P-CNF supports. In the case of N-CNF, the decrease could be attributed to the presence of water during the doping treatment, leading to decomposition of amorphous carbon within the CNF structure. In the case of P-CNF, the deposition of P species on the carbon surface could be responsible of blocking micropores, as previously reported [178].

The supports displayed an I_D/I_G intensity ratio of approximately 2, indicating the presence of a high concentration of edge sites, a feature commonly observed in platelet CNF [145]. Structural descriptors such as changes in the G band or I_D/I_G intensity ratios did not reveal differences among the doped CNF, suggesting that the structural defects present within the bulk CNF predominate over the alterations caused by the substitution of carbon sites with heteroatoms on the surface.

The catalyst characterization revealed significant variations among the catalysts featuring different surface functionalization, particularly evident in Pt dispersion and average particle size. Pt/CNF-HT and Pt/N-CNF exhibited high platinum dispersions of 47% and 43%, respectively. In contrast, Pt/S-CNF (26%) and Pt/B-CNF (19%) displayed lower dispersion levels. Although STEM images revealed the presence of dispersed platinum particles in the case of Pt/P-CNF, a different behavior was observed, resulting in suppression of amount of chemisorbed CO. This inhibition was attributed to the presence of phosphorus atoms on the carbon structure, leading to a change in the adsorption strength of CO as observed in previous studies [179].

Based on the analysis of heteroatom content and their distribution in various molecular structures, conducted through XPS and complemented by zeta potential measurements (Figure 4-15), it was evident that the surface charge density was influenced not only by the quantity of heteroatoms but also by the pH and nature of functional groups present on the carbon surface [180,181]. Pt/N-CNF and Pt/S-CNF showed a positive zeta potential attributed to the presence of weakly acidic or basic groups like pyrrolic, quaternary, and

pyridinic nitrogen. Conversely, samples with higher levels of acidic groups, such as hydroxyl (OH-) and carboxyl (COOH-) groups, exhibited a negative zeta potential (HT, P, B).

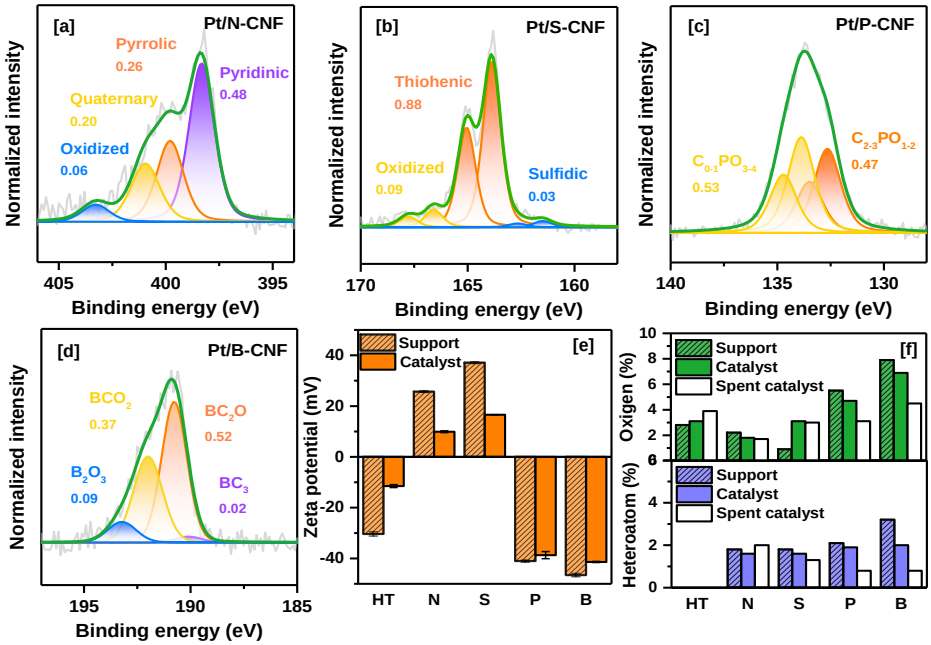

Figure 4-15. High-resolution XPS of [a] N 1s of Pt/ N-CNF, [b] S 2p of Pt/S-CNF [c] P 2p of Pt/P-CNF [d] B 1s of Pt/B-CNF reduced catalysts. [e] Zeta potential (mV) [f] oxygen and heteroatom content (at%) of the X-CNF supports and Pt-based reduced and spent catalysts.

A positive shift in Pt^0 biding energy (0.3 eV) was observed for Pt/CNF-HT, P/N-CNF, and Pt/S-CNF, relative to the binding energy of bulk Pt (71.7.eV). This shift indicates the presence of electronic interactions between Pt and the support. On the other hand, larger particles present in Pt/P-CNF and Pt/B-CNF could potentially mitigate the impact of dopants on the electronic structure of Pt, leading to no significant alteration in binding energy. These findings align with previous studies that have shown the dependence of metal-support interactions on particle size, exhibiting a more pronounced effect for nanoparticles smaller than 4 nm [96]

4.3.2 Aqueous phase reforming of ethylene glycol

The results from the batch APR experiments using Pt-based catalysts supported on heteroatom-doped CNF are shown in Figure 4-16. The catalysts ranked in descending order of EG conversion were as follows: Pt/N-CNF exhibited the highest conversion, followed by Pt/CNF-HT, Pt/P-CNF, Pt/B-CNF, and Pt/S-CNF. The predominant components in the gas phase were H_2 and CO_2, accompanied by minor quantities of methane (<3.4% mol) and ethane (<2.6% mol).

The liquid phase includes glycolic acid, acetic acid, ethanol, and methanol, with a higher production of alcohols compared to organic acids. The total carbon yield to the liquid phase remained below 15% of the initial carbon content for all the studied catalysts, with Pt/P-CNF displaying the highest liquid product yield among the catalysts

This observation implies that, except for Pt/P-CNF, the evaluated catalyst series did not substantially contribute to H_2 consumption via secondary reactions. The Pt/P-CNF catalyst, however, displayed a potential to facilitate the hydrogenation of unsaturated intermediates, resulting in the utilization of generated H_2 for the formation of methane and liquid by-products.

Following APR of ethylene glycol, the XPS of the catalysts exhibited Pt binding energy values that were consistent, closely resembling bulk platinum at approximately 71.7 eV. Additionally, while N-CNF and CNF-HT maintain their heteroatom content during APR, P-CNF and B-CNF experience a reduction of P, B and O content at the carbon surface, with a loss of up to 40% (Figure 4-15 [f]). This loss indicates that they are susceptible to leaching under demanding hydrothermal APR conditions [126]. Comparable findings were observed regarding Pt dispersion. The catalyst supported on N-CNF, and CNF-HT exhibited a relatively modest reduction in dispersion (30-40%), whereas B-CNF and S-CNF experienced a more pronounced decline in dispersion, ranging from a 55% to 60% decrease. The decrease in Pt dispersion, coupled with a reduction in heteroatom content on the carbon surface, most likely contribute to the weakened effect of neighboring species on the electronic properties of platinum.

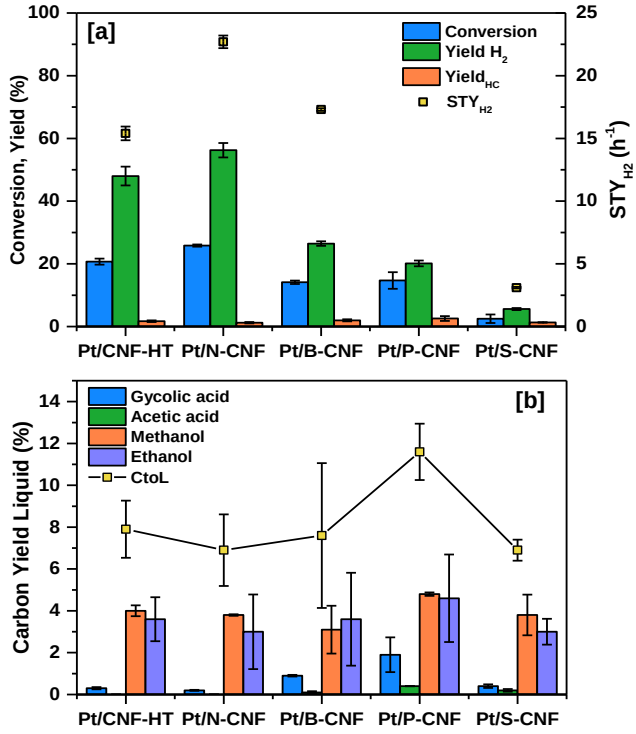

Figure 4-16. APR of 6 %wt ethylene glycol (EG) aqueous solution at 250 °C and 26 bar initial pressure in the batch reactor. [a] Catalytic conversion of EG, yields towards hydrogen and hydrocarbons, H_2 site time yield. [b] Carbon yield to main liquid products and total conversion of carbon to liquids (CtoL). The error bars represent the standard deviation in the experiments.

4.3.3 *In-situ* XAS characterization during aqueous phase reforming of ethylene glycol

To achieve a more comprehensive understanding of the local environment and oxidation state of platinum during APR, *in-situ* XAS experiments were conducted. In this section, cautious interpretation of the data analysis is necessary due to the EXAFS limitations in differentiating Pt-N, Pt-O, and Pt-C coordination due to the closely matched scattering amplitudes of C, N, and O.

The MCR-ALS analysis performed on the XANES spectra (Figure 4-17) revealed the presence of two main platinum species in each catalyst, in agreement with the EXAFS data fitting. Presence of a large fraction of Pt^0 was identified, exhibiting a slight increase during APR that aligns with XPS findings of the used catalysts, with a higher fraction of metallic

platinum (>65%). Pt species directly coordinated to heteroatoms N, S and P on Pt/N-CNF, Pt/S-CNF and Pt/P-CNF were detected. Additionally, no contributions of boron species directly bonded to platinum were observed.

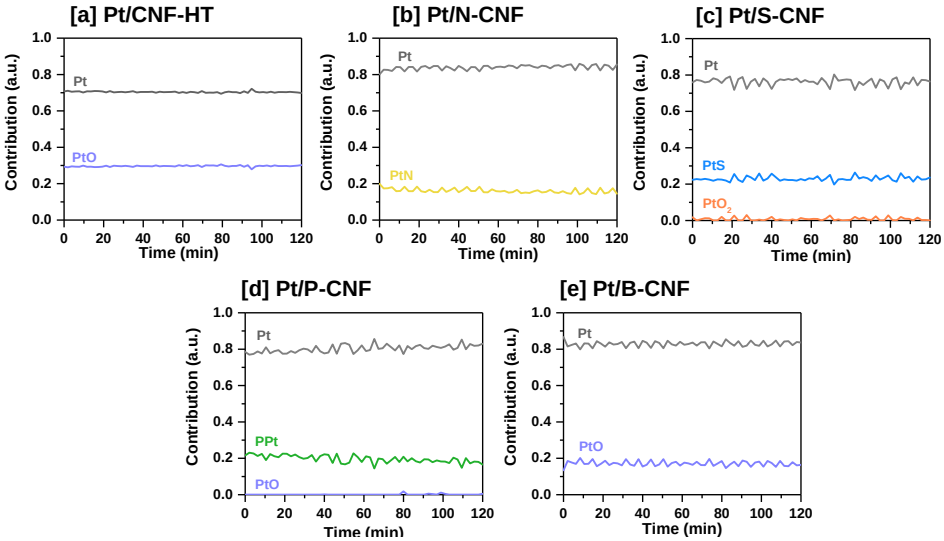

Figure 4-17. MCR-ALS results - Contribution of the species for [a] Pt/CNF-HT [b] Pt/N-CNF [c] Pt/S-CNF [d] Pt/P-CNF [e] Pt/B-CNF.

The fitting of the EXAFS data revealed an increase in the Pt-Pt coordination number for all catalysts, consistent with the lower dispersion estimated by CO chemisorption in the catalysts after APR. Furthermore, Pt/P-CNF and Pt/B-CNF exhibited high Pt-Pt coordination numbers, reaching 9 and 10 respectively, which is in agreement with the large particles detected in the STEM images.

The catalysts that exhibited a positive shift in Pt^0 binding energy in XPS also demonstrated a reduction in the Pt-Pt bond distance, specifically noticeable in Pt/N-CNF and Pt/S-CNF. This bond contraction could be linked to metal-support interactions that induce electronic modifications in Pt atoms closely located to species with high electron density, such as N or S [183].

At APR conditions, Pt/N-CNF, Pt/CNF-HT and Pt/B-CNF exhibited a stable behavior with only a slight increase in the Pt^0 contribution along with a minor contribution identified as PtN or PtO, respectively. Pt/P-CNF, presented a decrease in Pt-P coordination number from 0.7 to 0.4 which may be due to a decrease in P content on the carbon support, as detected by XPS. In the case of Pt/S-CNF a minor additional presence of Pt^{+4} species (<2%) was detected.

4.3.4 Effect of carbon doping

The nature of the support plays a key role in altering the catalytic activity, connecting the conversion of polyols to bifunctional reactions involving both the support and the metal phase [184]. In the case of Pt-N/CNF the presence of basic sites alongside high platinum dispersion enhances the conversion towards H_2. The significant content of pyridinic N in the carbon surface, as detected by XPS (Figure 4-15[a]), could enhance water dissociation, promoting the WGS activity [164].

On the other hand, the presence of acidic functional groups on Pt/P-CNF and Pt/B-CNF favors dehydration of ethylene glycol, which lead to the production of alcohols and alkanes, as seen in Figure 4-16. Furthermore, they also encourage the desorption of intermediate species [185], resulting in rearrangement and formation of organic acids.

The low catalytic activity observed for Pt/P-CNF and Pt/B-CNF could be linked to two main factors: The presence of acid sites conferred by oxidized species on the carbon surface and the relatively low level of Pt dispersion. The acidic sites could hinder the adsorption of ethylene glycol by the increased hydrophilicity of the carbon surface, leading to competitive adsorption between water and ethylene glycol, as also observed by others [83,108]. A low dispersion would result in a lower number of active metal sites available for the reaction, thereby following alternative pathways promoted by the supports, such as dehydration reactions. In the case of Pt/S-CNF the reduced activity may be explained by the existence of metal-sulfur species that are catalytically inactive for EG reforming, identified during *in-situ* XAS.

4.3.5 Key findings

The various types of heteroatoms introduced on the supports impact the electronic density and dispersion of platinum on carbon nanofibers. By employing *in-situ* XAS to identify Pt-heteroatom species and Pt oxidation state during APR, correlating the platinum local coordination and electronic structure with the catalytic activity and selectivity throughout APR is enable. These results strengthen the concept that the performance of the catalyst is strongly influenced by the nature of the support, the active phase, and the interactions between them.

During APR of ethylene glycol, Pt/N-CNF was found to be the most promising catalyst for H_2 production associated with the high Pt dispersion and basic sites provided by the nitrogen species, resulting in enhanced activity for the water-gas shift reaction. On the other hand, Pt/P-CNF and Pt/B-CNF displayed lower platinum dispersion and less acid sites on the carbon surface, resulting in lower activity and higher production of liquid by-products and methane compared to Pt/N-CNF and Pt/CNF-HT.

In the following section, an alternative catalytic system is examined based on the findings from collaborative studies conducted within the BIKE project. The catalyst was developed at Johnson Matthey, and it is based on a PtNi system supported on TiO_2. To the best of our knowledge, a similar system has not been studied in the context of APR. Hence, the interaction between the components in the catalyst and the impact of the reaction conditions are evaluated.

4.4 Bimetallic interactions stabilizing Pt-Ni/TiO_2 catalysts in aqueous phase reforming of ethylene glycol

This section explores the aqueous phase reforming activity of a low metal loading (<1%wt) PtNi bimetallic catalyst supported on TiO_2. The catalyst was selected within the BIKE framework to study its stability under the hydrothermal reaction conditions exposed in APR and to gain a deeper understanding on how the catalyst performance is affected by changes in the reaction conditions. This investigation is discussed in Paper III, and it is subdivided in three sections:

1. Catalyst synthesis and characterization
2. Stability test in aqueous phase reforming of ethylene glycol
3. Kinetic studies

4.4.1 Catalyst synthesis and characterization

The catalyst was prepared by co-impregnating $Pt(NO_3)_4$ and $Ni(CH_3CO_2)_2{\cdot}4H_2O$ metal salts aiming for a Pt: Ni 1:1 molar ratio with loading of 1%wt Pt and 0.3wt% Ni. Following a drying step at 105 °C overnight, a reduction step at 250°C for two hours in 10%H_2/N_2 flow, and a passivation, exposing the catalyst to a 1% O_2/N_2 mixture at room temperature for 20 min.

The crystalline structure of the reduced and passivated catalyst was studied by XRD. The diffraction pattern presented the characteristic anatase-to-rutile ratio of P25 with no peaks attributed to Pt and Ni related to the low metal loading of the catalyst and the expected high dispersion of the nanoparticles.

To identify the initial chemical state of the platinum and nickel on TiO_2, *ex-situ* XPS was performed on the catalyst. The Pt 4f spectrum can be fitted by only one platinum specie at 71.5 eV, showing the significant contribution of metallic platinum on the surface of the catalyst [186]. The Ni $2p_{3/2}$ spectra have a low signal-to-noise ratio due to the low Ni content. However, two discernable peaks attributed to Ni(0) at 852 eV and Ni II or Ni(III) at 856 eV are observed [187], where it appears that the majority of the nickel species on the catalyst surface are in the oxidized state.

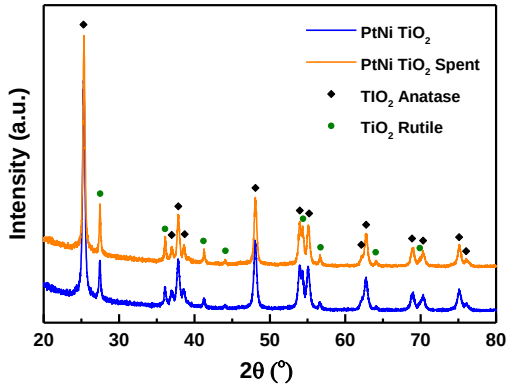

Figure 4-18. XRD patterns of $PtNi/TiO_2$ before and after aqueous phase reforming of 6%wt ethylene glycol solution at 225°C and 30 bars for 120 hours on stream (WHSV = $2h^{-1}$)

EXAFS analysis was used to obtain information about the structure of the bimetallic $PtNi/TiO_2$ catalyst. The Fourier transform (FT) of the k^2-weighted EXAFS spectrum collected at the Pt L_3 edge including the fitting results are presented in Figure 4-19 and Table 4-5. The fit of the Pt L_3 edge shows a Pt-Pt contribution with a coordination number of 7.51 at a bonding distance of 2.70 Å, which is similar to that in PtNi alloy (2.71Å) [188].

Furthermore, there is a Pt-Ni contribution with a coordination number of 0.82 at an interatomic distance of 2.65, larger than the Pt-Ni distance for the PtNi alloy (2.62 Å) but still within the expected range of contraction for Pt particles [189]. This result suggests the presence of bimetallic particles with much of the Ni located at near-surface region, in accordance with the indications from local density calculations, which reveal surface segregation of Ni [190]. Furthermore, the local composition of PtNi nanoparticles, estimated with the ratio $CN_{Pt\text{-}Ni}/CN_{Pt\text{-}Pt}$ of 1:0.11, indicates that only a fraction of the Ni atoms directly interacts with Pt. As suggested in XPS, the rest of the Ni may be present in oxide phases. A total coordination number of 6.84 is estimated considering a Pt fraction of 0.9 and Ni fraction of 0.1, providing an average particle size of 1.5 nm [191,192], in agreement with the particle size obtained from the analysis of the TEM images.

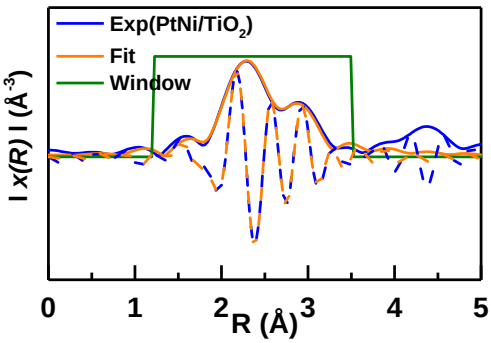

Figure 4-19. Pt L_3 edge EXAFS fitting curves of the reduced $PtNi/TiO_2$ catalyst in R space

Table 4-5. Coordination numbers (CN), radial distances (R) and Debye–Waller type factor (σ^2) determined by EXAFS fitting of the Pt L_3 edge on the reduced catalyst

$PtNi/TiO_2$ catalyst			
Shell	**CN**	**R (Å)**	**σ^2 (Å)**
Pt-Ni	0.82	2.65	0.0040
Pt-Pt	7.51	2.70	0.0039

R-factor 0.006
Estimated accuracy CN: ± 10-20%,
R: ± 0.02Å
Expected Pt-Ni distance 2.62 Å, Pt-Pt 2.71 for PtNi alloy [188]

Furthermore, TEM micrographs of the $PtNi/TiO_2$ catalyst (Figure 4-20) show the uniform distribution of the nanoparticles over the support and confirm the average nanoparticle size of 2. 1 ± 1.0 nm in the reduced catalyst, in agreement with EXAFS results.

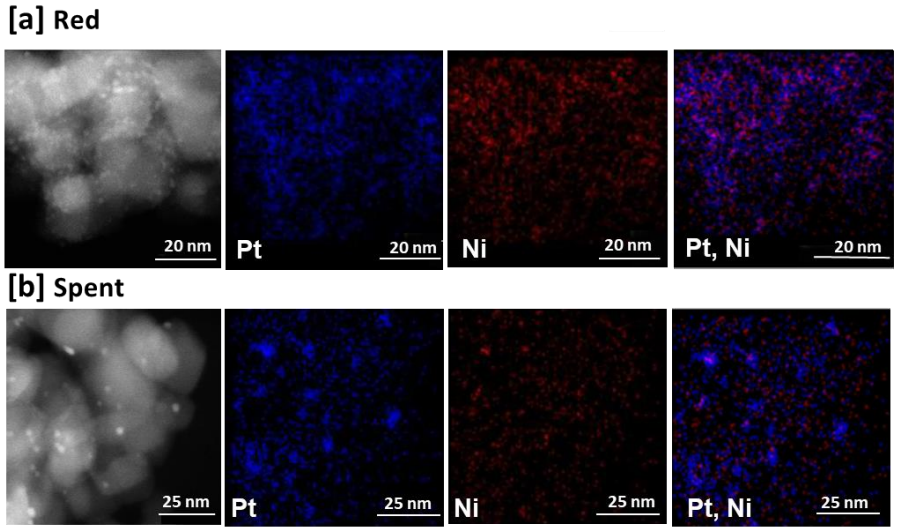

Figure 4-20. TEM micrographs and elemental map profiles of the $PtNi/TiO_2$ catalyst [a] reduced [b] spent after aqueous phase reforming of ethylene glycol (6%wt) at 225°C, 30 bar and WHSV=$2h^{-1}$, 120 hours on stream.

4.4.2 Stability test in aqueous phase reforming of ethylene glycol

A continuous flow setup (section 3.5.3) was used to conduct a 120-hour experiment to evaluate catalytic activity and stability. After the reaction, the catalyst was regenerated by flushing with DI water and subjected to the same reduction process used for the newly prepared catalyst. As can be seen from Figure 4-21, the catalyst exhibits stable catalytic activity after initial deactivation in the first 40 hours. A stable yield of H_2 and methane was obtained, including a preferential ethanol production in the liquid phase accompanied by methanol, acetaldehyde, acetic acid, and glycolic acid.

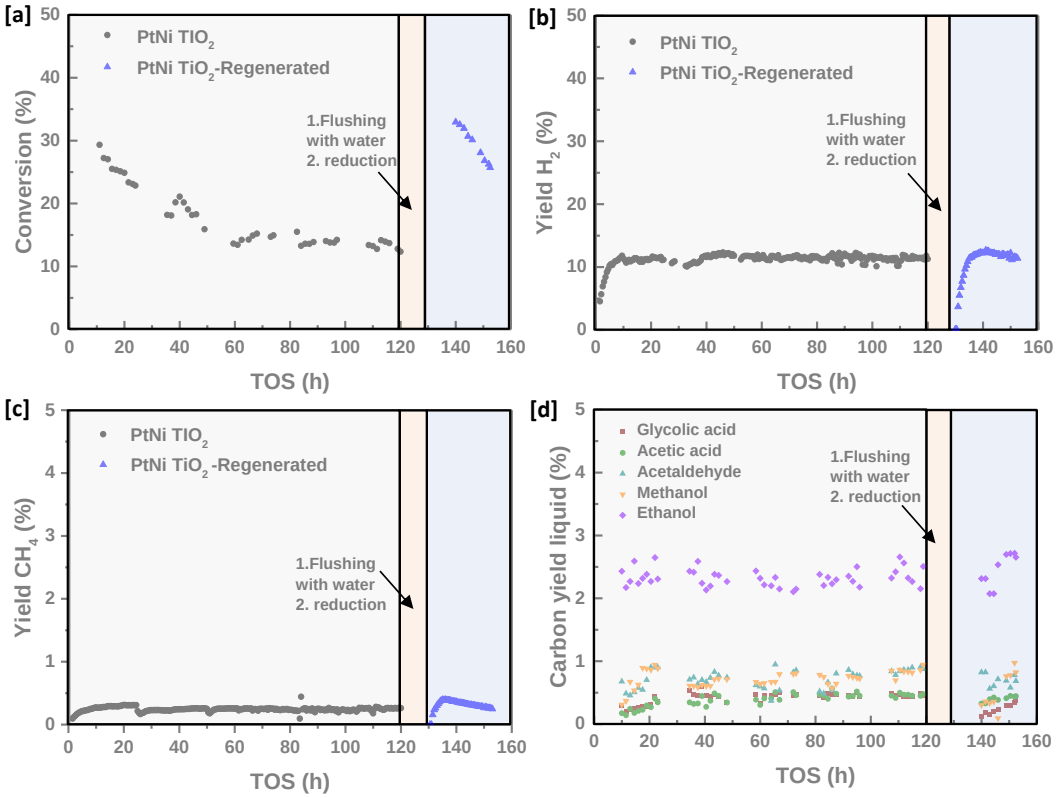

Figure 4-21. Aqueous phase reforming of ethylene glycol (6%wt) at 225°C, 30 bar and WHSV=2h^{-1}. Evolution of [a] Ethylene glycol conversion (%) [b] H_2 yield (%) [c] CH_4 yield [d] Carbon yield to liquid products (%) with time on stream (TOS). The mass balance closure shows a 10-20% error, with a higher error in the initial 40 hours on stream associated with back mixing and long residence time of the liquid phase.

These observations are consistent with previous studies including DFT calculations [193], where the decomposition of ethylene glycol over a monolayer of Ni atoms on top of a Pt(111) surface occurs initially by O-H cleavage, which can lead to the intermediates on the surface susceptible to form acetaldehyde and ethanol, as observed in the liquid product distribution. Furthermore, the hydrogen production rate in terms of grams of Pt present in the sample (16.0 ± 0.6 mmol/g_{Pt}·min) is slightly higher than values reported for catalyst with similar molar ratio 1:1 ($PtNi/Al_2O_3$); 13.3 mmol/g_{pt}·min [60].

After the stability test, the catalyst was characterized by XRD and TEM, and the metal content was determined by MP-AES. A phase transition could be detected from the X-ray diffraction pattern for the spent catalyst, an intensity decreases in anatase peaks at 25.3° and a rise in intensity for the rutile peaks (between 27.4 and 54.3°) was observed. From the Rietveld refinement, it was identified that the relative anatase phase composition decreases from 86% to 81%, while the rutile phase increases from 14% to 19%.

The TEM micrograph (Figure 4-20 [b]) revealed moderate sintering of the metal nanoparticles with an average particle size of 4.4 ± 1.0 nm after reaction. HR-TEM showed crystal lattices with d-spacing of 0.244 nm attributed to the (111) NiO plane and 0.23 nm linked to face-centered cubic Pt(111). Moreover, from the elemental analysis, 9% of Pt and 80% of Ni were estimated to leach out during APR. This significant degree of metal leaching, especially for Ni, could be associated with the formation of oxidized nickel species susceptible to leaching under hydrothermal conditions [73].

The catalyst exhibited stable activity for 120 hours on stream, despite experiencing irreversible deactivation mechanisms such as sintering and metal leaching, suggesting that the leached fractions of Ni and Pt in the catalyst were not in an active form for ethylene glycol conversion. Besides, after the catalyst regeneration, the initial high activity was regained. Hence, it seems that a reversible deactivation takes place during the initial stages of APR of ethylene glycol, observed by the decrease in conversion (Figure 4-21 [a]). The deactivation could be associated with competitive adsorption of reaction intermediates such as CO, as indicated in previous studies [60].

4.4.3 Kinetic studies

The reaction kinetics were studied at different temperatures (215-235°C) and EG feed concentrations (1-20%wt) in a semi-continuous reactor set-up, described in section 3.5.2. In the experiments carried out for the kinetic studies, the main products observed were H_2, CO_2 and a mixture of C1-C2 alkanes along with methanol and ethanol in the liquid

phase. Furthermore, the gas phase analysis revealed a minor concentration of carbon dioxide, as presented in Figure 4-22.

Due to limited knowledge of the reaction intermediates, and the low concentration of by-products, such as methane and CO, the pathway included in the considerations for the kinetic model was simplified to focus on ethylene glycol consumption and H_2 and CO_2 production. Equations 4.1 and 4.2 illustrate the reforming of ethylene glycol followed by the water-gas-shift reaction.

$$C_2H_6O_2 \rightarrow 2CO + 3H_2 \quad 4.1$$

$$CO + H_2O \leftrightarrow H_2 + CO_2 \quad 4.2$$

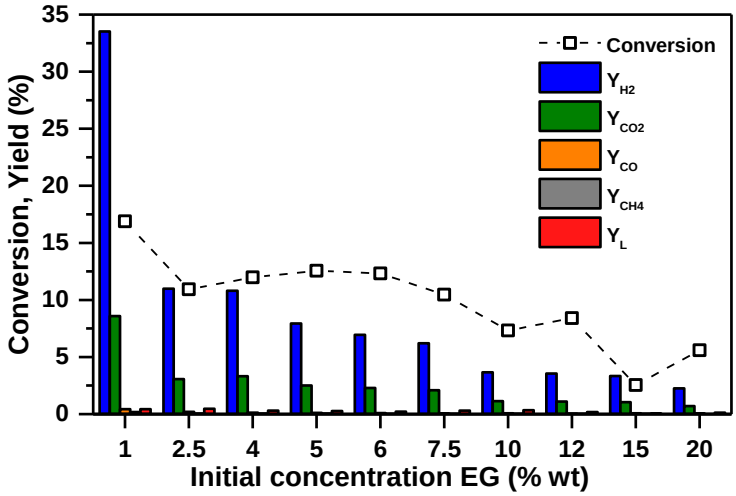

Figure 4-22. Total conversion of ethylene glycol (weight-based) and carbon-based yield of hydrogen (Y_{H2}), carbon dioxide (Y_{CO2}), carbon monoxide (Y_{CO}), methane (Y_{CH4}), and liquid products (Y_L) in aqueous phase reforming over $PtNi/TiO_2$ at 215°C and 40 bar.

The model proposed by Shabaker *et al.* [175] based on dehydrogenation of adsorbed ethylene glycol as the rate-determining step (rk_{rxn}) is used in this study. It is considered that the absorption of ethylene glycol, water, H_2 and CO_2 are quasi-equilibrated, the reforming reaction involves irreversible steps on the catalyst surface and that the WGS reaction was approximated to equilibrium. Hence, the rate expression was based on the most abundant species on the catalyst surface H*, CO*, $C_2O_6H_5$* and OH*, as presented in Equation 4.3 (* denotes surface sites)

$$r = \frac{k_{rxn} K_{EG} P_{EG}}{\left[1 + \sqrt{K_{H2} P_{H2}}\left(1 + \frac{k_{rxn} K_{EG} P_{EG}}{k_{WGS} K_{H2O} P_{H2O}}\right) + K_{EG} P_{EG} + \frac{K_{H2O} P_{H2O}}{\sqrt{K_{H2} P_{H2}}}\right]^2} \quad (4.3) \text{ [175]}$$

Further simplifications were implemented in the model following similar assumptions proposed by D'Angelo *et al.* [194]. The $K_{H2O} P_{H2O}$ is considered constant due to the low concentration of ethylene glycol, and the term $\frac{k_{rxn} K_{EG} P_{EG}}{k_{WGS} K_{H2O} P_{H2O}}$ is assumed to be significantly smaller than 1, and thus excluded from the model. Hence, a reduced model is presented in equation 4.4 based on the liquid phase concentrations of ethylene glycol and hydrogen.

$$r = \frac{k'_{rxn} C_{EG}^{liq}}{\left[1 + \sqrt{k'_{H2} C_{H2}^{liq}} + k'_{EG} C_{EG}^{liq} + + \frac{K''_{H2}}{\sqrt{C_{H2}^{liq}}}\right]^2} \quad (4.4) \text{ [194]}$$

rk'_{rxn} *kinetic parameter* $m^3/mol_{Pt}*s$

k'_{H2} *kinetic parameter* m^3/mol

k'_{EG} *kinetic parameter* m^3/mol

k''_{H2} *kinetic parameter* m^3/mol

C_{EG}^{liq} *Concentration EG in the liquid phase* $[mol/m^3]$

C_{H2}^{liq} *Concentration* H_2 *in the liquid phase*$[mol/m^3]$

To estimate the kinetic parameters, the objective function is minimized by the sum of squared residuals between the model predictions and the corresponding experimental data. Phyton version 3.1 using Broyden, Fletcher, Goldfarb, and Shanno (BFGS) optimization algorithm provided within the SciPy library was used for achieving the best possible fit.

Table 4-6 presents the estimated kinetic parameters. The large covariance obtained for the kinetic parameter k''_{H2} may be linked to the limited amount of experimental data and the low conversion levels obtained at the applied reaction conditions. Besides, a negative value for this parameter suggests that H_2 is consumed by side reactions not accounted for in the model, such as CO_2 methanation. To improve the statistical robustness of the model, a second kinetic model excluding the k''_{H2} was evaluated, obtaining lower correlations between the parameters, and leading to a more reliable statistical model.

Table 4-6. Estimated model parameters and sum of squared residuals.

Parameter	Model 4 parameters		Model 3 parameters	
	Value	Covariance	Value	Covariance
rk'_{rxn} $[m^3/mol_{Pt}s]$	2.91 x 10^{-4}	5.71 x 10-5	3.74	0.025
k'_{H2} $[m^3/mol]$	2.61	1.479	1.71 x 10^{4}	25.03
k'_{EG} $[m^3/mol]$	5.80 x 10^{-3}	0.0002	7.96 x 10^{-2}	0.1155
k''_{H2} $[m^3/mol]$	-1.35	218.43	-	-
Sum of squared residuals	0.0002			0.0005

Discrepancies were observed between the experimental reaction rate and the two simplified models at low and high values of ethylene glycol concentration within the evaluated range (Figure 4-23), underestimating the H_2 formation rate at the boundaries of the examined interval (0.05 mol/m^3 and 0.08 mol/m^3). Nonetheless. despite its simplicity, the model can describe the trend in H_2 formation rate during aqueous phase reforming of ethylene glycol over the PtNi/TiO_2 catalyst and emphasizes the impact of initial ethylene glycol concentration on the catalytic process.

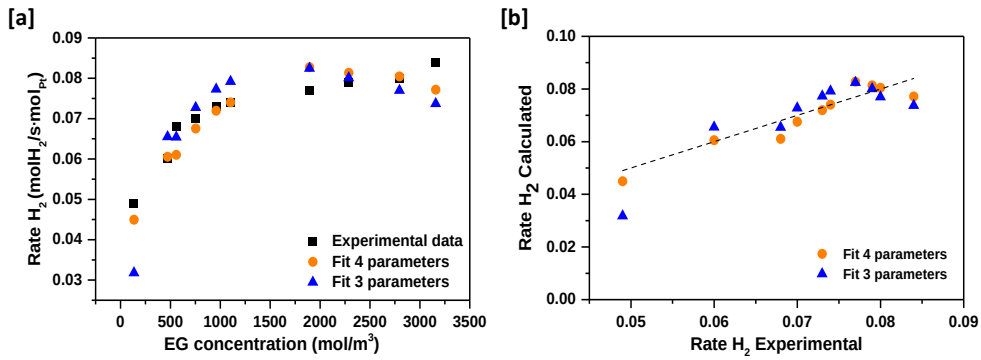

Figure 4-23. [a] Comparison of the calculated and experimental rate as function of ethylene glycol concentration [b] Parity plot of the reaction rate.

4.4.4 Key findings

The PtNi/TiO_2 catalyst with low noble metal content (<1%wt) exhibited highly dispersed nanoparticles on the support, and the presence of bimetallic particles confirmed by EXAFS analysis. The metal-metal interactions, along with a favorable support for the water-gas

shift reaction, demonstrate an effective combination that ensures stable activity for 120 hours of continuous operation, favoring activity and selectivity towards H_2 production. A partial phase transition from anatase to rutile TiO_2 was detected in the spent catalyst, suggesting that this transformation was induced by the elevated pressures and hydrothermal conditions to which the catalyst was exposed. After the stability test, metal leaching and a slight degree of sintering were detected. However, no direct effect on the catalytic performance was observed.

Furthermore, a simplified kinetic model was evaluated based on the liquid phase concentrations of ethylene glycol and H_2. The model is able to estimate to a certain extent the effect of variations in the concentration of ethylene glycol on the H_2 production rate at 215°C, but with limitations at very low concentrations of ethylene glycol (<0.05 mol/m^3).

Chapter 5: Conclusions and suggestions for future work

5.1 Concluding remarks

Aqueous phase reforming has been proposed as a strategic method for hydrogen production to valorize aqueous solutions containing oxygenates, mainly derived from biomass. The catalytic system is crucial for meeting the challenges associated with the demanding hydrothermal conditions and high feed functionalities that contribute to catalyst deactivation and numerous side reactions, and thus delaying industrial applications. This study approached different strategies to enhance the catalytic activity and selectivity towards hydrogen production of Pt-based catalysts in aqueous phase reforming of polyols.

Initially, the potential of improving the catalytic activity by introducing a second metal to the catalytic systems was demonstrated. The addition of Sn to Ni systems proved beneficial in promoting the activity of Ni-based catalysts supported on mixed oxides with moderate H_2 selectivity. Besides, adding Mn to a platinum-based catalyst supported on carbon nanofibers enhanced the catalytic performance by metal-metal interactions that decrease the electron density of Pt, promoting its activity in aqueous phase reforming of ethylene glycol.

After observing the relevance of the electronic properties of the metal on catalytic activity, modifications were made to the support to further evaluate the effect of these properties. Doped carbon nanofibers were studied to achieve high metal dispersion of the active phase leading to high activity and favoring H_2 selectivity due to electronic effects induced by the heteroatom in the support. It has been demonstrated that N-doped carbon nanofibers favor the formation of H_2 by providing a catalyst with high metal dispersion and basic surface groups, thus promoting the WGS activity.

Furthermore, *in-situ* XAS-XRD characterization allowed for identification of Pt-heteroatom species and Pt oxidation state in the context of aqueous phase reforming, establishing a connection between the local coordination and electronic structure of platinum and the catalytic performance.

Despite developments in catalyst design, issues associated with catalyst stability are still present, attributed predominantly to sintering and metal leaching. Therefore, utilizing component combinations that favor the metal-support interactions can help mitigate the

negative impact of exposing the catalyst to hydrothermal conditions and acidic streams, such as in aqueous phase reforming.

In view of this, it is evident that the synergy between metal-metal interactions, metal-support interactions, and supports promoting the water gas-shift reaction, demonstrates successful combinations to ensure stable catalytic performance, as observed for the bimetallic system PtMn supported on nitrogen-doped carbon nanofibers and PtNi supported on TiO_2. Hence, these findings reinforce the significant influence on the catalytic performance from the nature of the support, the selected monometallic or bimetallic system, and the mutual interactions.

5.2 Suggestions for future work

This investigation revealed that the stability of the catalyst during aqueous phase reforming is compromised, leading to sintering and metal leaching, mainly observed for base metals such as Ni and Mn in the bimetallic systems studied. Metal leaching is attributed to the oxidation of the metal phase that is more susceptible to dissolution into the aqueous media, and this oxidation can be promoted by the low pH obtained by the formation of side products such as organic acids during the reaction. In spite of metal leaching, for the catalytic system evaluated through the development of this research, PtMn/N-CNF and PtNi/TiO_2 seem to maintain their catalytic activity while losing a significant amount of the base metal during the reaction.

On this basis, future fundamental research should explore further the reasons behind the sustained catalytic activity despite metal leaching. This could support the observations on the retained electronic effects on Pt likely associated with structural effects on the nanoparticles, or that the leached species may originate from metal phases not active in aqueous phase reforming. Advanced characterization techniques such as high angle annular dark field scanning transmission electron microscopy, along with X-ray photoelectron spectroscopy (XPS) and *in-situ* X-ray absorption spectroscopy (XAS), can provide valuable insights into the state of the catalyst at the local level, allowing for more detailed visualization of what might take place at the catalyst atomic scale to relate it to the catalytic performance.

In relation to the doped-carbon supports, an aspect worth exploring in more detail is the interaction of the dopant on the carbon surface with the surrounding media. More

precisely, how the acidity/ basicity provided by the different surface groups on the carbon support affects the reaction rate in aqueous phase reforming of polyols. Some functional groups will facilitate the adsorption of reactants and products, acknowledging that the presence of water in the system can limit the surface reaction by competitive adsorption. Hence, a comprehensive characterization of the acidic/basic sites on the carbon surface is crucial for better understanding of the catalytic activity at these liquid-solid interphases.

A brief discussion into the effect of pH was introduced in the catalyst screening section, observing how the pH of the solution alter catalyst selectivity to enhance or detriment the formation of hydrogen. In this context, the exploitation of the reforming reaction towards valuable products in the liquid phase can be achieved by tuning the reaction conditions, as we observed that a higher pH favors the stability of a Ni-based catalyst and enhancing the carbon yield towards liquid phase products. Therefore, fundamental studies into the reaction pathways that take place at these different conditions would be useful to expand the applicability of aqueous phase reforming.

The ultimate goal in catalyst design is to tune the selectivity to the desired product while maintaining high activity and stability during the reaction. In the aqueous phase reforming context, an environment that favors high-metal dispersion to increase the number of active sites and to improve the stability of the catalyst is the final aim for promoting H_2 production. Thus, bimetallic particle formation, strong metal-support interactions, or mesoporous supports with high surface areas are promising strategies to obtain effective catalysts for aqueous phase reforming applications. The challenges associated with the variability and complexity of the feed still need to be addressed. Hence, studying the catalyst in potential wastewater streams for industrial integration is a natural way to continue improving the catalyst design where new challenges will emerge, such as poisoning, and eventually will be addressed, strengthening the catalyst applicability.

The study of aqueous phase reforming in realistic scenarios will allow to direct the research to supplementary issues associated with reactor design or catalyst mechanical strength. For example, the poor mechanical strength of pelletized carbon-based catalysts and the relatively low density are a concern in fixed-bed reactors. Overcoming these limitations will allow for successful implementation of carbon-based catalysts at a larger scale.

References

[1] IEA, World Energy Outlook 2022, Paris, 2022.
[2] European Commission, Joint Research Centre, K. Keramidas, F. Fosse, A. Diaz Rincon, P. Dowling, R. Garaffa, J. Ordonez, P. Russ, B. Schade, A. Schmitz, A. Soria Ramirez, T. Vandyck, M. Weitzel, Global Energy and Climate Outlook 2022 – Energy Trade in a Decarbonised World, Publications Office of the European Union, 2022.
[3] IEA, Global Energy Review: CO2 Emissions in 2021, Paris, 2022.
[4] IEA, CO2 Emissions in 2022, Paris, 2023.
[5] T. Serrano, S. Aparcana, F. Bakhtiari, A. Laurent, J. Ind. Ecol. 25 (2021) 1382–1397.
[6] B. Moore, C. Verfuerth, A.M. Minas, C. Tipping, S. Mander, I. Lorenzoni, C. Hoolohan, A.J. Jordan, L. Whitmarsh, WIREs Clim. Change 12 (2021) e738.
[7] EU, A Hydrogen Strategy for a Climate-Neutral Europe, 2020.
[8] IEA, Global Hydrogen Review 2022, Paris, 2022.
[9] G. Hu, C. Chen, H.T. Lu, Y. Wu, C. Liu, L. Tao, Y. Men, G. He, K.G. Li, Engineering 6 (2020) 1364–1380.
[10] R. Moliner, M.J. Lázaro, I. Suelves, Int. J. Hydrog. Energy 41 (2016) 19500–19508.
[11] F. Dawood, M. Anda, G.M. Shafiullah, Int. J. Hydrog. Energy 45 (2020) 3847–3869.
[12] P. Nikolaidis, A. Poullikkas, Renew. Sustain. Energy Rev. 67 (2017) 597–611.
[13] T. Lepage, M. Kammoun, Q. Schmetz, A. Richel, Biomass Bioenergy 144 (2021) 105920.
[14] N. Dahmen, I. Lewandowski, S. Zibek, A. Weidtmann, GCB Bioenergy 11 (2019) 107–117.
[15] P.R. Lanjekar, N.L. Panwar, C. Agrawal, Bioresour. Technol. Rep. 21 (2023) 101293.
[16] M. Buffi, M. Prussi, N. Scarlat, Biomass Bioenergy 165 (2022) 106556.
[17] D. Woolf, J.E. Amonette, F.A. Street-Perrott, J. Lehmann, S. Joseph, Nat. Commun. 1 (2010) 56.
[18] D. Glushkov, G. Nyashina, A. Shvets, A. Pereira, A. Ramanathan, Energies 14 (2021) 7541.
[19] G. Zoppi, G. Pipitone, C. Galletti, A.M. Rizzo, D. Chiaramonti, R. Pirone, S. Bensaid, Catal. Today 365 (2021) 206–213.
[20] L. Leng, W. Zhang, S. Leng, J. Chen, L. Yang, H. Li, S. Jiang, H. Huang, Sci. Total Environ. 748 (2020) 142383.
[21] F.J. Campanario, F.J. Gutiérrez Ortiz, Energy Convers. Manag. 154 (2017) 591–602.
[22] S.D. Davidson, J.A. Lopez-Ruiz, Y. Zhu, A.R. Cooper, K.O. Albrecht, R.A. Dagle, ACS Sustain. Chem. Eng. 7 (2019) 19889–19901.
[23] R.D. Cortright, R.R. Davda, J.A. Dumesic, Nature 418 (2002) 964–967.
[24] R.R. Davda, J.W. Shabaker, G.W. Huber, R.D. Cortright, J.A. Dumesic, Appl. Catal. B Environ. 43 (2003) 13–26.
[25] J. González-Arias, Z. Zhang, T.R. Reina, J.A. Odriozola, Environ. Chem. Lett. (2023).
[26] G. Zoppi, G. Pipitone, H. Gruber, G. Weber, A. Reichhold, R. Pirone, S. Bensaid, Catal. Today 367 (2021) 239–247.
[27] G. Bressanelli, M. Perona, N. Saccani, Int. J. Prod. Res. 57 (2019) 7395–7422.
[28] G.S. Simate, J. Cluett, S.E. Iyuke, E.T. Musapatika, S. Ndlovu, L.F. Walubita, A.E. Alvarez, Desalination 273 (2011) 235–247.
[29] B. Saenz de Miera, A.S. Oliveira, J.A. Baeza, L. Calvo, J.J. Rodriguez, M.A. Gilarranz, J. Clean. Prod. 252 (2020) 119849.
[30] J. Remón, L. García, J. Arauzo, Fuel Process. Technol. 154 (2016) 66–81.
[31] S. O-Thong, A. Hniman, P. Prasertsan, T. Imai, Int. J. Hydrog. Energy 36 (2011) 3409–3416.
[32] I.K. Kapdan, F. Kargi, Enzyme Microb. Technol. 38 (2006) 569–582.

[33] A.S. Oliveira, J.A. Baeza, L. Calvo, M.A. Gilarranz, Chem. Eng. J. 460 (2023) 141770.
[34] A. S. Oliveira, J. A. Baeza, L. Calvo, N. Alonso-Morales, F. Heras, J. Lemus, J. J. Rodriguez, M. A. Gilarranz, Environ. Sci. Water Res. Technol. 4 (2018) 1979–1987.
[35] C.H. Giang, A. Osatiashtiani, V.C. Dos Santos, A.F. Lee, D.R. Wilson, K.W. Waldron, K. Wilson, Catalysts 4 (2014) 414–426.
[36] F.R. Hartley, Chemistry of the Platinum Group Metals: Recent Developments, Elsevier, 2013.
[37] R.G. Cawthorn, Platin. Met. Rev. 54 (2010) 205–215.
[38] P.B. Kettler, Org. Process Res. Dev. 7 (2003) 342–354.
[39] H. Tang, Z. Peng, R. Tian, L. Ye, J. Zhang, M. Rao, G. Li, J. Environ. Chem. Eng. 11 (2023) 110237.
[40] Johnson Matthey Group, Platinum: A Sustainable Solution for the Energy Transition, UK, 2023.
[41] I. Directorate-General for Internal Market, M. Grohol, C. Veeh, Study on the Critical Raw Materials for the EU 2023: Final Report, Publications Office of the European Union, LU, 2023.
[42] Anglo American Platinum Limited, Climate Change Report 2021, South Africa, 2022.
[43] C. Hagelüken, Platin. Met. Rev. 56 (2012) 29–35.
[44] C. Saguru, S. Ndlovu, D. Moropeng, Hydrometallurgy 182 (2018) 44–56.
[45] B. El-Zahab, A. Chamaani, N. Chawla, M. Safa, Battery Cathodes for Improved Stability, US11588144B2, 2023.
[46] M.L. Personick, M.M. Montemore, E. Kaxiras, R.J. Madix, J. Biener, C.M. Friend, Philos. Trans. R. Soc. Math. Phys. Eng. Sci. 374 (2016) 20150077.
[47] J.W. Shabaker, G.W. Huber, J.A. Dumesic, J. Catal. 222 (2004) 180–191.
[48] R.R. Davda, J.W. Shabaker, G.W. Huber, R.D. Cortright, J.A. Dumesic, Appl. Catal. B Environ. 56 (2005) 171–186.
[49] I. Coronado, M. Stekrova, M. Reinikainen, P. Simell, L. Lefferts, J. Lehtonen, Int. J. Hydrog. Energy 41 (2016) 11003–11032.
[50] G.W. Huber, J.A. Dumesic, Catal. Today 111 (2006) 119–132.
[51] D.M. Alonso, S.G. Wettstein, J.A. Dumesic, Chem. Soc. Rev. 41 (2012) 8075–8098.
[52] R.D. Cortright, R.R. Davda, J.A. Dumesic, Nature 418 (2002) 964–967.
[53] R.R. Davda, J.W. Shabaker, G.W. Huber, R.D. Cortright, J.A. Dumesic, Appl. Catal. B Environ. 56 (2005) 171–186.
[54] T. van Haasterecht, C.C.I. Ludding, K.P. de Jong, J.H. Bitter, J. Energy Chem. 22 (2013) 257–269.
[55] M. Sankar, N. Dimitratos, P.J. Miedziak, P.P. Wells, C.J. Kiely, G.J. Hutchings, Chem. Soc. Rev. 41 (2012) 8099–8139.
[56] M.-C. Kim, T.-W. Kim, H.J. Kim, C.-U. Kim, J.W. Bae, Renew. Energy 95 (2016) 396–403.
[57] G.W. Huber, J.W. Shabaker, S.T. Evans, J.A. Dumesic, Appl. Catal. B Environ. 62 (2006) 226–235.
[58] P.J. Dietrich, R.J. Lobo-Lapidus, T. Wu, A. Sumer, M.C. Akatay, B.R. Fingland, N. Guo, J.A. Dumesic, C.L. Marshall, E. Stach, J. Jellinek, W.N. Delgass, F.H. Ribeiro, J.T. Miller, Top. Catal. 55 (2012) 53–69.
[59] G. Pipitone, G. Zoppi, R. Pirone, S. Bensaid, Int. J. Hydrog. Energy (2021) S0360319921037848.
[60] G.W. Huber, J.W. Shabaker, S.T. Evans, J.A. Dumesic, Appl. Catal. B Environ. 62 (2006) 226–235.
[61] M.-C. Kim, T.-W. Kim, H.J. Kim, C.-U. Kim, J.W. Bae, Renew. Energy 95 (2016) 396–403.
[62] M.M. Rahman, Catal. Lett. 150 (2020) 2674–2687.

[63] H.-D. Kim, H.J. Park, T.-W. Kim, K.-E. Jeong, H.-J. Chae, S.-Y. Jeong, C.-H. Lee, C.-U. Kim, Catal. Today 185 (2012) 73–80.
[64] Z. Wei, A. Karim, Y. Li, Y. Wang, ACS Catal. 5 (2015) 7312–7320.
[65] F. Bossola, X.I. Pereira-Hernández, C. Evangelisti, Y. Wang, V. Dal Santo, J. Catal. 349 (2017) 75–83.
[66] H.-D. Kim, H.J. Park, T.-W. Kim, K.-E. Jeong, H.-J. Chae, S.-Y. Jeong, C.-H. Lee, C.-U. Kim, Int. J. Hydrog. Energy 37 (2012) 8310–8317.
[67] M. Führer, T. van Haasterecht, J. H. Bitter, Catal. Sci. Technol. 10 (2020) 6089–6097.
[68] T. Soták, M. Hronec, I. Vávra, E. Dobročka, Int. J. Hydrog. Energy 41 (2016) 21936–21944.
[69] O.G. Marin-Flores, A.M. Karim, Y. Wang, Catal. Today 237 (2014) 118–124.
[70] V. Dal Santo, A. Gallo, A. Naldoni, M. Guidotti, R. Psaro, Catal. Today 197 (2012) 190–205.
[71] T. van Haasterecht, C.C.I. Ludding, K.P. de Jong, J.H. Bitter, J. Energy Chem. 22 (2013) 257–269.
[72] J.W. Shabaker, D.A. Simonetti, R.D. Cortright, J.A. Dumesic, J. Catal. 231 (2005) 67–76.
[73] T. van Haasterecht, C.C.I. Ludding, K.P. de Jong, J.H. Bitter, J. Catal. 319 (2014) 27–35.
[74] D.C. Grenoble, M.M. Estadt, D.F. Ollis, J. Catal. 67 (1981) 90–102.
[75] Y. Guo, M.U. Azmat, X. Liu, Y. Wang, G. Lu, Appl. Energy 92 (2012) 218–223.
[76] T. Sakamoto, T. Miyao, A. Yoshida, S. Naito, Int. J. Hydrog. Energy 35 (2010) 6203–6209.
[77] C. Pendem, B. Sarkar, N. Siddiqui, L.N.S. Konathala, C. Baskar, R. Bal, ACS Sustain. Chem. Eng. 6 (2018) 2122–2131.
[78] J.W. Shabaker, G.W. Huber, R.R. Davda, R.D. Cortright, J.A. Dumesic, Catal. Lett. 88 (2003) 1–8.
[79] B. Roy, K. Loganathan, H.N. Pham, A.K. Datye, C.A. Leclerc, Int. J. Hydrog. Energy 35 (2010) 11700–11708.
[80] A.V.-H. Soares, G. Perez, F.B. Passos, Appl. Catal. B Environ. 185 (2016) 77–87.
[81] D.Y. Murzin, S. Garcia, V. Russo, T. Kilpiö, L.I. Godina, A. V. Tokarev, A. V. Kirilin, I.L. Simakova, S. Poulston, D.A. Sladkovskiy, J. Wärnå, Ind. Eng. Chem. Res. 56 (2017) 13240–13253.
[82] B. Kaya, S. Irmak, A. Hasanoglu, O. Erbatur, Int. J. Hydrog. Energy 39 (2014) 10135–10140.
[83] X. Wang, N. Li, J.A. Webb, L.D. Pfefferle, G.L. Haller, Appl. Catal. B Environ. 101 (2010) 21–30.
[84] C. He, J. Zheng, K. Wang, H. Lin, J.-Y. Wang, Y. Yang, Appl. Catal. B Environ. 162 (2015) 401–411.
[85] T.-W. Kim, H.-D. Kim, K.-E. Jeong, H.-J. Chae, S.-Y. Jeong, C.-H. Lee, C.-U. Kim, Green Chem. 13 (2011) 1718–1728.
[86] A. Mohamed, in: S. Yaragalla, R. Mishra, S. Thomas, N. Kalarikkal, H.J. Maria (Eds.), Carbon-Based Nanofillers Their Rubber Nanocomposites, Elsevier, 2019, pp. 243–257.
[87] P. Serp, M. Corrias, P. Kalck, Appl. Catal. Gen. 253 (2003) 337–358.
[88] V. Jiménez, P. Panagiotopoulou, P. Sánchez, J.L. Valverde, A. Romero, Chem. Eng. J. 168 (2011) 947–954.
[89] C.F. Sanz-Navarro, P.-O. Åstrand, D. Chen, M. Rønning, A.C.T. van Duin, W.A.I. Goddard, J. Phys. Chem. C 114 (2010) 3522–3530.
[90] C.F. Sanz-Navarro, P.-O. Åstrand, D. Chen, M. Rønning, A.C.T. van Duin, T. Jacob, W.A. Goddard, J. Phys. Chem. A 112 (2008) 1392–1402.
[91] H. Cheng, I. Kvande, Y.-A. Zhu, N. Hammer, M. Rønning, J.C. Walmsley, P. Li, Z. Qi, X.-G. Zhou, D. Chen, J. Phys. Chem. C 122 (2018) 7166–7178.

[92] J.K. Chinthaginjala, K. Seshan, L. Lefferts, Ind. Eng. Chem. Res. 46 (2007) 3968–3978.
[93] E. Santillan-Jimenez, M. Perdu, R. Pace, T. Morgan, M. Crocker, Catalysts 5 (2015) 424–441.
[94] H. Jüntgen, Fuel 65 (1986) 1436–1446.
[95] H. Wang, Y. Shao, S. Mei, Y. Lu, M. Zhang, J. Sun, K. Matyjaszewski, M. Antonietti, J. Yuan, Chem. Rev. 120 (2020) 9363–9419.
[96] E. García-Bordejé, M.F.R. Pereira, M. Rönning, D. Chen, in: Catalysis, 2014, pp. 72–108.
[97] A.R. Deline, B.P. Frank, C.L. Smith, L.R. Sigmon, A.N. Wallace, M.J. Gallagher, D.G.Jr. Goodwin, D.P. Durkin, D.H. Fairbrother, Chem. Rev. 120 (2020) 11651–11697.
[98] Y. Rangraz, M. M. Heravi, RSC Adv. 11 (2021) 23725–23778.
[99] N.F. Sylla, N.M. Ndiaye, B.D. Ngom, B.K. Mutuma, D. Momodu, M. Chaker, N. Manyala, J. Colloid Interface Sci. 569 (2020) 332–345.
[100] G. Hasegawa, T. Deguchi, K. Kanamori, Y. Kobayashi, H. Kageyama, T. Abe, K. Nakanishi, Chem. Mater. 27 (2015) 4703–4712.
[101] F. Herold, T. Imhof, P. Roumeliotis, P. Schühle, M. Ledendecker, M. Rønning, Carbon 207 (2023) 207–218.
[102] P. Serp, J.L. Figueiredo, Carbon Materials for Catalysis, John Wiley & Sons, 2009.
[103] H. Wang, T. Maiyalagan, X. Wang, ACS Catal. 2 (2012) 781–794.
[104] F. Rodríguez-reinoso, Carbon 36 (1998) 159–175.
[105] M.L. Toebes, J.M.P. van Heeswijk, J.H. Bitter, A. Jos van Dillen, K.P. de Jong, Carbon 42 (2004) 307–315.
[106] K.A. Wepasnick, B.A. Smith, K.E. Schrote, H.K. Wilson, S.R. Diegelmann, D.H. Fairbrother, Carbon 49 (2011) 24–36.
[107] S. Kundu, Y. Wang, W. Xia, M. Muhler, J. Phys. Chem. C 112 (2008) 16869–16878.
[108] X. Wang, N. Li, L.D. Pfefferle, G.L. Haller, J. Phys. Chem. C 114 (2010) 16996–17002.
[109] W. Jun Lee, U. Narayan Maiti, J. Min Lee, J. Lim, T. Hee Han, S. Ouk Kim, Chem. Commun. 50 (2014) 6818–6830.
[110] S. van Dommele, A. Romero-Izquirdo, R. Brydson, K.P. de Jong, J.H. Bitter, Carbon 46 (2008) 138–148.
[111] M. Inagaki, M. Toyoda, Y. Soneda, T. Morishita, Carbon 132 (2018) 104–140.
[112] S. van Dommele, K.P. de Jong, J.H. Bitter, Chem. Commun. (2006) 4859–4861.
[113] L. Jia, D.A. Bulushev, O.Yu. Podyacheva, A.I. Boronin, L.S. Kibis, E.Yu. Gerasimov, S. Beloshapkin, I.A. Seryak, Z.R. Ismagilov, J.R.H. Ross, J. Catal. 307 (2013) 94–102.
[114] Y. Shao, J. Sui, G. Yin, Y. Gao, Appl. Catal. B Environ. 79 (2008) 89–99.
[115] A. García-Baldoví, L. Peng, A. Santiago-Portillo, A.M. Asiri, A. Primo, H. García, ACS Appl. Energy Mater. 5 (2022) 9173–9180.
[116] P. Gogoi, N. Kanna, P. Begum, R.C. Deka, S. C. V. V, T. Raja, ACS Catal. 10 (2020) 2489–2507.
[117] S. Ghosh, S. Barg, S.M. Jeong, K. (Ken) Ostrikov, Adv. Energy Mater. 10 (2020) 2001239.
[118] Q. Zhang, D. Zhang, Y. Zhou, J. Qian, X. Wen, P. Jiang, L. Ma, C. Lu, F. Feng, X. Li, ChemistrySelect 7 (2022) e202102581.
[119] X.-Y. Liu, M. Huang, H.-L. Ma, Z.-Q. Zhang, J.-M. Gao, Y.-L. Zhu, X.-J. Han, X.-Y. Guo, Molecules 15 (2010) 7188–7196.
[120] H. Ik Lee, S. Hoon Joo, J. Hoe Kim, D. Jong You, J. Man Kim, J.-N. Park, H. Chang, C. Pak, J. Mater. Chem. 19 (2009) 5934–5939.
[121] P. Yin, X. Luo, Y. Ma, S.-Q. Chu, S. Chen, X. Zheng, J. Lu, X.-J. Wu, H.-W. Liang, Nat. Commun. 12 (2021) 3135.
[122] J.K. Dunleavy, Platin. Met. Rev. 50 (2006) 110.
[123] F. Auer, D. Blaumeiser, T. Bauer, A. Bösmann, N. Szesni, J. Libuda, P. Wasserscheid, Catal. Sci. Technol. 9 (2019) 3537–3547.

[124] D.-S. Yang, D. Bhattacharjya, S. Inamdar, J. Park, J.-S. Yu, J. Am. Chem. Soc. 134 (2012) 16127–16130.
[125] A.M. Puziy, O.I. Poddubnaya, B. Gawdzik, J.M.D. Tascón, Carbon 157 (2020) 796–846.
[126] S. Campisi, F.J. Sanchez Trujillo, D. Motta, T.E. Davies, N. Dimitratos, A. Villa, C 4 (2018) 9.
[127] L. Wang, X. Dong, H. Jiang, G. Li, M. Zhang, Catal. Commun. 56 (2014) 164–167.
[128] Z. Liu, Q. Shi, F. Peng, H. Wang, H. Yu, J. Li, X. Wei, Catal. Commun. 22 (2012) 34–38.
[129] H. Chen, Y. Xiong, T. Yu, P. Zhu, X. Yan, Z. Wang, S. Guan, Carbon 113 (2017) 266–273.
[130] M.K. Ubhi, M. Kaur, J.K. Grewal, V.K. Sharma, Materials 16 (2023) 1155.
[131] C.K. Acharya, C.H. Turner, J. Phys. Chem. B 110 (2006) 17706–17710.
[132] C.K. Acharya, W. Li, Z. Liu, G. Kwon, C. Heath Turner, A.M. Lane, D. Nikles, T. Klein, M. Weaver, J. Power Sources 192 (2009) 324–329.
[133] J. Zhou, K. Wu, W. Wang, Z. Xu, H. Wan, S. Zheng, Appl. Catal. Gen. 470 (2014) 336–343.
[134] I. Esteve-Adell, B. Crapart, A. Primo, P. Serp, H. Garcia, Green Chem. 19 (2017) 3061–3068.
[135] W.-H. Chiang, G.-L. Chen, C.-Y. Hsieh, S.-C. Lo, RSC Adv. 5 (2015) 97579–97588.
[136] X. Chen, Z. Xu, F. Yang, H. Zhao, Proc. Combust. Inst. 37 (2019) 5499–5506.
[137] W.J. Stark, J.-D. Grunwaldt, M. Maciejewski, S.E. Pratsinis, A. Baiker, Chem. Mater. 17 (2005) 3352–3358.
[138] M. Minnermann, H.K. Grossmann, S. Pokhrel, K. Thiel, H. Hagelin-Weaver, M. Bäumer, L. Mädler, Catal. Today 214 (2013) 90–99.
[139] M. Tepluchin, M. Casapu, A. Boubnov, H. Lichtenberg, D. Wang, S. Kureti, J.-D. Grunwaldt, ChemCatChem 6 (2014) 1763–1773.
[140] S. Brunauer, P.H. Emmett, E. Teller, J. Am. Chem. Soc. 60 (1938) 309–319.
[141] M. Fadoni, L. Lucarelli, Stud. Surf. Sci. Catal. 120 (1999) 177–225.
[142] S. Gražulis, D. Chateigner, R.T. Downs, A.F.T. Yokochi, M. Quirós, L. Lutterotti, E. Manakova, J. Butkus, P. Moeck, A. Le Bail, J. Appl. Crystallogr. 42 (2009) 726–729.
[143] C.F. Holder, R.E. Schaak, ACS Nano 13 (2019) 7359–7365.
[144] D.A. Shirley, Phys. Rev. B 5 (1972) 4709–4714.
[145] P. Mallet-Ladeira, P. Puech, C. Toulouse, M. Cazayous, N. Ratel-Ramond, P. Weisbecker, G.L. Vignoles, M. Monthioux, Carbon 80 (2014) 629–639.
[146] C.H. Camp, J. Res. Natl. Inst. Stand. Technol. 124 (2019) 1–10.
[147] B. Ravel, M. Newville, J. Synchrotron Radiat. 12 (2005) 537–541.
[148] A. Zimina, K. Dardenne, M.A. Denecke, D.E. Doronkin, E. Huttel, H. Lichtenberg, S. Mangold, T. Pruessmann, J. Rothe, T. Spangenberg, R. Steininger, T. Vitova, H. Geckeis, J.-D. Grunwaldt, Rev. Sci. Instrum. 88 (2017) 113113.
[149] M. Loewert, M.-A. Serrer, T. Carambia, M. Stehle, A. Zimina, K. F. Kalz, H. Lichtenberg, E. Saraçi, P. Pfeifer, J.-D. Grunwaldt, React. Chem. Eng. 5 (2020) 1071–1082.
[150] H.-D. Kim, T.-W. Kim, H.J. Park, K.-E. Jeong, H.-J. Chae, S.-Y. Jeong, C.-H. Lee, C.-U. Kim, Int. J. Hydrog. Energy 37 (2012) 12187–12197.
[151] G.W. Huber, J.W. Shabaker, J.A. Dumesic, Science 300 (2003) 2075–2075.
[152] J.W. Shabaker, G.W. Huber, J.A. Dumesic, J. Catal. 222 (2004) 180–191.
[153] M. Stekrova, A. Rinta-Paavola, R. Karinen, Catal. Today 304 (2018) 143–152.
[154] J. Liu, B. Sun, J. Hu, Y. Pei, H. Li, M. Qiao, J. Catal. 274 (2010) 287–295.
[155] J. Tao, L. Hou, B. Yan, G. Chen, W. Li, H. Chen, Z. Cheng, F. Lin, Energy Fuels 34 (2020) 1153–1161.
[156] J. Liu, X. Chu, L. Zhu, J. Hu, R. Dai, S. Xie, Y. Pei, S. Yan, M. Qiao, K. Fan, ChemSusChem 3 (2010) 803–806.
[157] J. Remón, C. Jarauta-Córdoba, L. García, J. Arauzo, Appl. Catal. B Environ. 219 (2017) 362–371.

[158] B.N. Zope, D.D. Hibbitts, M. Neurock, R.J. Davis, Science 330 (2010) 74–78.
[159] C. Chiu, A. Genest, N. Rösch, Top. Catal. 56 (2013) 874–884.
[160] E. Pitzalis, R. Psaro, C. Evangelisti, Inorganica Chim. Acta 533 (2022) 120782.
[161] L. Calvillo, M. Gangeri, S. Perathoner, G. Centi, R. Moliner, M.J. Lázaro, J. Power Sources 192 (2009) 144–150.
[162] P. Li, T.-J. Zhao, J.-H. Zhou, Z.-J. Sui, Y.-C. Dai, W.-K. Yuan, Carbon 43 (2005) 2701–2710.
[163] K.P. De Jong, J.W. Geus, Catal. Rev. 42 (2000) 481–510.
[164] Y. Guo, M.U. Azmat, X. Liu, Y. Wang, G. Lu, Appl. Energy 92 (2012) 218–223.
[165] H. Kim, Y.-H. Lee, H. Lee, J.-C. Seo, K. Lee, Catalysts 10 (2020) 828.
[166] Z. Alipour, M. Rezaei, F. Meshkani, J. Energy Chem. 23 (2014) 633–638.
[167] A.J. Plomp, D.S. Su, K.P. de Jong, J.H. Bitter, J. Phys. Chem. C 113 (2009) 9865–9869.
[168] F. Herold, J. Gläsel, B.J.M. Etzold, M. Rønning, Chem. Mater. 34 (2022) 8490–8516.
[169] S.K. Jain, E.M. Crabb, L.E. Smart, D. Thompsett, A.M. Steele, Appl. Catal. B Environ. 89 (2009) 349–355.
[170] L.P.L. Gonçalves, M. Meledina, A. Meledin, D.Y. Petrovykh, J.P.S. Sousa, O.S.G.P. Soares, Y.V. Kolen'ko, M.F.R. Pereira, Carbon 195 (2022) 35–43.
[171] O.Yu. Podyacheva, A.S. Lisitsyn, L.S. Kibis, A.I. Stadnichenko, A.I. Boronin, E.M. Slavinskaya, O.A. Stonkus, S.A. Yashnik, Z.R. Ismagilov, Catal. Today 301 (2018) 125–133.
[172] K. Jiang, X.-Y. Ma, S. Back, J. Zhao, F. Jiang, X. Qin, J. Zhang, W.-B. Cai, CCS Chem. 3 (2021) 241–251.
[173] Y.-H. Li, T.-H. Hung, C.-W. Chen, Carbon 47 (2009) 850–855.
[174] Z. Wu, B.C. Bukowski, Z. Li, C. Milligan, L. Zhou, T. Ma, Y. Wu, Y. Ren, F.H. Ribeiro, W.N. Delgass, J. Greeley, G. Zhang, J.T. Miller, J. Am. Chem. Soc. 140 (2018) 14870–14877.
[175] J.W. Shabaker, J.A. Dumesic, Ind. Eng. Chem. Res. 43 (2004) 3105–3112.
[176] D.J.M. de Vlieger, B.L. Mojet, L. Lefferts, K. Seshan, J. Catal. 292 (2012) 239–245.
[177] J. Zhu, T. Zhao, I. Kvande, D. Chen, X. Zhou, W. Yuan, Chin. J. Catal. 29 (2008) 1145–1151.
[178] P. Song, L. Zhu, X. Bo, A. Wang, G. Wang, L. Guo, Electrochimica Acta 127 (2014) 307–314.
[179] L.-X. Ding, A.-L. Wang, G.-R. Li, Z.-Q. Liu, W.-X. Zhao, C.-Y. Su, Y.-X. Tong, J. Am. Chem. Soc. 134 (2012) 5730–5733.
[180] L. Vanyorek, R. Meszaros, S. Barany, Colloids Surf. Physicochem. Eng. Asp. 448 (2014) 140–146.
[181] H. Hu, A. Yu, E. Kim, B. Zhao, M.E. Itkis, E. Bekyarova, R.C. Haddon, J. Phys. Chem. B 109 (2005) 11520–11524.
[182] T.W. van Deelen, C. Hernández Mejía, K.P. de Jong, Nat. Catal. 2 (2019) 955–970.
[183] Y. Zhang, M.L. Toebes, A. van der Eerden, W.E. O'Grady, K.P. de Jong, D.C. Koningsberger, J. Phys. Chem. B 108 (2004) 18509–18519.
[184] A. Wawrzetz, B. Peng, A. Hrabar, A. Jentys, A.A. Lemonidou, J.A. Lercher, J. Catal. 269 (2010) 411–420.
[185] M. Führer, T. van Haasterecht, N. Masoud, D.H. Barrett, T. Verhoeven, E. Hensen, M. Tromp, C.B. Rodella, H. Bitter, ChemCatChem 14 (2022) e202200493.
[186] O. Fontelles-Carceller, M.J. Muñoz-Batista, E. Rodríguez-Castellón, J.C. Conesa, M. Fernández-García, A. Kubacka, J. Catal. 347 (2017) 157–169.
[187] M. El Doukkali, A. Iriondo, J.F. Cambra, I. Gandarias, L. Jalowiecki-Duhamel, F. Dumeignil, P.L. Arias, Appl. Catal. Gen. 472 (2014) 80–91.
[188] A. Jain, S.P. Ong, G. Hautier, W. Chen, W.D. Richards, S. Dacek, S. Cholia, D. Gunter, D. Skinner, G. Ceder, K.A. Persson, APL Mater. 1 (2013) 011002.
[189] Y. Lei, J. Jelic, L.C. Nitsche, R. Meyer, J. Miller, Top. Catal. 54 (2011) 334–348.
[190] I.A. Abrikosov, A.V. Ruban, H.L. Skriver, B. Johansson, Phys. Rev. B 50 (1994) 2039–2042.

[191] N.S. Marinkovic, K. Sasaki, R.R. Adzic, J. Electrochem. Soc. 165 (2018) J3222.
[192] A. Frenkel, Z. Für Krist. - Cryst. Mater. 222 (2007) 605–611.
[193] O. Skoplyak, M.A. Barteau, J.G. Chen, Surf. Sci. 602 (2008) 3578–3587.
[194] M.F.N. D'Angelo, J.C. Schouten, J. van der Schaaf, T.A. Nijhuis, Ind. Eng. Chem. Res. 53 (2014) 13892–13902.

Appendix A: Paper I

Nitrogen-containing carbon nanofibers as supports for bimetallic Pt-Mn catalysts in aqueous phase reforming of ethylene glycol

Published in Catalysis Today, March 2023.

Catalysis Today 418 (2023) 114066

Contents lists available at ScienceDirect

Catalysis Today

journal homepage: www.elsevier.com/locate/cattod

Nitrogen-containing carbon nanofibers as supports for bimetallic Pt-Mn catalysts in aqueous phase reforming of ethylene glycol

Monica Pazos Urrea, Felix Herold, De Chen, Magnus Rønning *

Department of Chemical Engineering, Norwegian University of Science and Technology, 7491 Trondheim, Norway

ARTICLE INFO

Keywords:
Aqueous phase reforming
Carbon nanofibers
Nitrogen doping
Bimetallic catalyst

ABSTRACT

Aqueous phase reforming (APR) of ethylene glycol was performed at 225 °C and 30 bar in batch and continuous reaction conditions. The effect on the APR performance by functionalizing carbon supports with nitrogen and adding Mn to Pt-based catalysts was investigated. The presence of nitrogen species on the carbon surface and Mn-addition (PtMn) improved the catalytic activity and promoted H_2 production. XPS results suggest that the enhancement of the catalytic activity may be attributed to charge transfer from platinum to the nitrogen groups and Mn. Pt-based catalysts were stable under the studied reaction conditions, while up to 97 % of the manganese leached into the liquid solution during APR. However, the catalytic activity was maintained even with such significant decrease in Mn content, indicating that only a small amount of Mn is necessary to maintain the promotional effect on Pt during APR.

1. Introduction

Aqueous phase reforming (APR), a process proposed by Dumesic and co-workers, utilizes biomass-derived wastewater streams to produce H_2 at relatively mild reaction conditions [1]. The APR process offers favorable conditions to obtain a H_2-rich stream with low CO content through the water-gas shift reaction (WGS). However, side reactions are also promoted, such as methanation and Fisher-Tropsch synthesis reactions, leading to formation of undesirable alkanes.

Sustainable H_2-rich streams can be used for fuel cell applications, the production of ammonia and synthetic liquid fuels, aiding to mitigate the intermittent nature of renewable energy [2]. However, the activity and stability of the catalyst during APR are compromised by the hydrothermal conditions in the presence of oxygenates at 200–270 °C and 20–60 bars, leading to deactivation through sintering, coke deposition, metal phase oxidation, and metal leaching.

APR catalysts must withstand severe hydrothermal conditions and exhibit strong metal-support interactions to minimize catalyst deactivation. Thus, the nature of the catalyst support plays a key role in the catalytic APR performance. Oxide supports such as TiO_2, ZrO_2, MgO, Al_2O_3 and SiO_2 suffer pore degradation and phase transformation under hydrothermal conditions leading to catalyst deactivation [3–6]. Carbon materials, including carbon black, carbon nanotubes, carbon nanofibers and mesoporous carbons demonstrate their high hydrothermal stability, resistance to acidic media and tunable chemical properties when studied in APR [7–10]. Nonetheless, the broad distribution of pore sizes, high microporosity and irregular pore structure of some carbon materials limit their applicability for APR, influencing the diffusion of the reactants and products throughout the structure of the catalyst [11].

Carbon nanofibers (CNF) are suitable as support material for APR due to their unique structural and textural properties that can be tuned according to the synthesis conditions. Various ratios of edge/basal atoms in the carbon structure lead to different CNF structures [12]. Platelet carbon nanofibers have their graphite sheets stacked perpendicularly to the fiber axis, thus exposing predominantly carbon edge sites [13]. These edge sites can be used as anchoring sites for metal particles on the carbon support giving stronger metal-support interactions [12,14–16], a desirable feature to enhance catalyst stability at APR conditions.

Pt is the most studied metal for APR since it is highly active and selective towards hydrogen production [17]. However, it has been demonstrated that using bimetallic catalyst such as Pt-Ni [18] Pt-Re [19] Pt-Co [20] and Pt-Mn [11] promotes the catalytic activity. For example, Re and Co are known for favoring the WGS reaction by tuning the electronic properties of the catalyst and modifying the biding energies of CO [21,22]. However, base metals are affected by the hydrothermal conditions in APR. Van Haasterecht et al. [7] studied cobalt, nickel, copper and platinum supported on CNF in APR of ethylene glycol and observed leaching of the base metal catalyst due to oxidation in the

* Corresponding author.
E-mail address: magnus.ronning@ntnu.no (M. Rønning).

https://doi.org/10.1016/j.cattod.2023.114066
Received 31 October 2022; Received in revised form 21 February 2023; Accepted 26 February 2023
Available online 1 March 2023

acidic media. A similar pattern is observed for Mn where most of the metal leached out during APR [9].

Thus, to promote the interaction between the metal particles and the support, functionalization of the carbon surface is proposed as a promising route. It has previously been observed that nitrogen-doping of carbon supports has a positive effect in liquid phase reactions. It is shown to be advantageous for the distribution of meal particles on the support, enhance the metal-support interaction, as well as modifying the electronic structure of the metal particles [23–26]. Gogoi et al. [23] observed that the nitrogen on the support not only aids in anchoring of Ru particles on the surface but also decreases the reduction temperature of Ru nanoparticles. This decrease is attributed to interactions between electron-rich nitrogen atoms present on the carbon surface and the Ru species, leading to a higher fraction of metallic Ru during APR of glycerol.

In this work we evaluate the promoting effect of nitrogen surface functionalization of a platelet CNF support on Pt and Pt-Mn based catalyst by evaluating the catalytic activity, selectivity and stability in APR of ethylene glycol (EG). Mn, a known unstable promoter at APR conditions, was selected to evaluate if the surface modification of the support in addition to the interaction with Pt is sufficient to stabilize Mn during APR. The role played by the support and the properties introduced to stabilize the metals on the support are discussed.

2. Experimental section

2.1. Catalyst synthesis

2.1.1. Carbon nanofiber synthesis

The preparation of platelet carbon nanofibers (CNF) has been described in detail elsewhere [27]. In short, carbon nanofibers were synthetized by chemical vapor deposition in a tubular quartz reactor using a Fe_3O_4 catalyst. About 100 mg of catalyst was reduced in 25 % H_2/Ar (100 mL/min) at 600 °C for 6 h (heating rate 5 °C/min), followed by flushing with Ar for 30 min. A synthesis mixture of CO/H_2 (50/12.5 mL/min) was introduced to grow CNF at 600 °C for 46 h.

2.1.2. Functionalization of CNF

To remove the Fe_3O_4 CNF growth catalyst contained in the fibers and to introduce surface functional oxygen groups, the as-synthetized CNF were treated in concentrated nitric acid (70 %) under reflux conditions for 3 h at 90 °C. Subsequently, the suspension was filtered, washed with deionized water until pH 7 was reached, and dried overnight at 100 °C. The acid treated CNF are denoted CNF-ox.

Heat treatment of CNF-ox was carried out in a quartz reactor inside a vertical tubular furnace. The CNF-ox were subjected to heat treatment in argon (100 mL/min) for 2 h at 700 °C to remove unstable oxygen groups introduced to the carbon surface during the acid treatment. The heat-treated CNF are denoted CNF-HT.

A gasification-assisted heteroatom doping method was utilized for nitrogen-doping of CNF-ox (N-CNF). The method consists of generating defects on the carbon surface with the aid of a gasification agent (H_2O) in the presence of a gaseous nitrogen source at high temperature. Nitrogen will occupy the new sites created by the gasification of carbon.

A vertical tubular furnace with a quartz reactor was used for the N-doping with ethylene diamine as the nitrogen source. First, 365 mg of CNF-ox were loaded into the reactor and heated to 875 °C at a heating rate of 10 °C/min in N_2 atmosphere (200 mL/min). Once the system reached the desired temperature, the nitrogen stream was saturated by flowing through a sparger with 1:1.5 (mol: mol) ethylene diamine/water solution and fed into the reactor for 90 min. Then, the system was cooled down in N_2 atmosphere (100 mL/min). A schematic drawing of the experimental setup is provided in Fig. S1.

2.1.3. Catalyst synthesis

Platinum (nominal loading 3 %wt) was introduced to the CNF by incipient wetness impregnation using chloroplatinic acid hexahydrate H_2PtCl_6 x$6H_2O$ (Sigma-Aldrich, > 37 % Pt basis) as metal precursor and acetone (Sigma Aldrich, 99.9 %) as solvent. The support material was mixed dropwise with the Pt solution and kept at room temperature overnight, followed by drying at 100 °C for 20 h. Subsequently, the prepared catalyst was heat-treated in N_2 atmosphere (100 mL/min) at 320 °C (heating rate 3 °C/min) for 2 h to decompose the precursors from the synthesis.

A similar procedure was followed for the bimetallic Pt-Mn catalysts using manganese (II) nitrate hydrate $Mn(NO_3)_2{\cdot}xH_2O$ (Sigma Aldrich, 98 %) as Mn precursor and acetone as solvent. Pt and Mn solutions were added to the CNF support by co-impregnation (nominal loading 3 %wt and 0.8 %wt), followed by drying and decomposition using the same conditions as for the monometallic catalysts.

2.2. Catalyst characterization

Textural properties of the carbon supports were measured by N_2 physisorption at − 196 °C using a Micromeritics Tristar 3000 instrument. About 100 mg of the samples were degassed overnight at 200 °C prior the analysis. The specific surface area was calculated by the BET method [28].

CO chemisorption was carried out in a Micromeritics ASAP 2020 instrument. 100 mg of the sample was reduced *in situ* for 1 h in pure H_2 at 300 °C with a heating rate of 5 °C/min. After the reduction, the system was purged in helium at 120 °C for 30 min before cooling down to 35 °C for the chemisorption analysis. Pt dispersion was evaluated assuming a Pt/CO adsorption stoichiometry of 1 [29]. The error in the chemisorption measurements is obtained from repeated measurements assumed to be in the range of 1–2.5 %, giving a standard deviation in the dispersion values of + /- 1.

The particle size (d) in nm was estimated assuming spherical shape from Eq. (1).

$$D = \frac{6M}{\rho d N_a S_a} \tag{1}$$

Where D is the metal dispersion (%) obtained by CO chemisorption, M is the atomic weight, N_a is Avogadro's number, S_a the area of each surface atom and $\rho$the density of Pt ($21.45 g/cm^3$).

X-ray diffraction was carried out in a Bruker D8 A25 DaVinci X-ray diffractometer using Cu Kα radiation and a LynxEye detector. Diffractograms were acquired in the 2θ range 10–80° with a step size of 0.044°. Peak identification was conducted by comparing it to the crystallography open database [30]. The Scherrer equation was used to estimate the Pt average crystallite size from the XRD pattern. The Scherrer constant d was assumed as 0.89 [31].

Metal loading was determined by microwave plasma atomic emission spectroscopy (Agilent 4210 MP-AES optical emission spectrometer). The samples were prepared by microwave assisted digestion using a speedwave XPERT (Berghof) instrument. The digestion was carried out in two steps, initially heating up to 170 °C, remaining at this temperature for 10 min followed by an increase in temperature to 210 °C for 20 min with a power of 2 × 800 W in 10 mL HCl/HNO_3 mixture (1:4, vol:vol). Then, the samples were transferred to a 100 mL volumetric flask, adjusting the volume with Millipore Milli-Q water, and filtered with a syringe filter (0.2 μm) before the analysis. External calibration with Pt and Mn standards for ICP (Sigma-Aldrich, 1000 mg/L) was carried out before every measurement.

X-ray photoelectron spectroscopy (XPS) was performed at ambient temperature under ultra-high vacuum (UHV). The measurements were conducted in a Kratos Analytical Axis Ultra DLD spectrometer using monochromatic Al Kα radiation (1486.6 eV) operating the anode at 10 kV with an aperture of 700 × 300 μm. For each sample, a survey spectrum was measured with a pass energy of 160 eV, while high-resolution spectra were recorded with a pass energy of 20 eV. The

binding energy scale of the system was calibrated to the C1s contribution of sp^2 carbon at 284.6 eV. The peaks were deconvoluted after Shirley background subtraction [32] and fitted to linear combinations of Gaussian and Lorentzian functions. The full set of band assignments as well as fitting parameters are listed in Table S1.

Samples for scanning transmission electron microscopy (STEM) were prepared by ultrasonic dispersion in n-hexane followed by drop-casting on carbon coated copper grids. STEM micrographs were obtained on a Hitachi SU9000 electron microscope operating at an accelerating voltage of 30 kV. Energy-dispersive X-ray spectroscopy (EDS) was performed at an accelerating voltage of 30 kV using an Oxford Ultim Extreme 100 mm^2 windowless detector.

2.3. Catalytic testing in aqueous phase reforming

2.3.1. Batch reactor testing

Aqueous phase reforming of ethylene glycol was carried out in a 160 mL stainless-steel mini bench reactor (Parr 4592 model) equipped with a magnetic driver stirrer and PID temperature controller (Parr Instruments Co., USA). A quartz reactor was employed for the *ex-situ* catalyst reduction in a vertical tubular furnace. Typically, the catalyst was reduced *ex-situ* at 300 °C for 1 h in 5 % H_2/N_2 flow (100 mL/min, heating rate 5 °C/min).

The pre-reduced catalyst (200 mg) and 30 mL of 6 %wt aqueous ethylene glycol solution were loaded into the vessel. The reactor was thoroughly purged with nitrogen and pressurized to an initial pressure of 20 bar, which served as an internal standard for the final quantification of the products present in the gas phase. The mixture was subsequently stirred at 500 rpm and heated to 225 °C. After 2 h at 225 °C, the reactor was quenched to room temperature in an ice water bath. Gaseous products were collected in a multilayer foil gas sampling bag (Supelco). After depressurization, the liquid products were collected and filtered with a 0.2 μm PTFE filter. The spent catalyst was recovered by filtration, washed with DI water, and dried overnight at 60 °C.

Gas phase products were analyzed by gas chromatography (Agilent 7820 A) equipped with a thermal conductivity detector (TCD) and a flame ionization detector (FID). H_2, CO, CO_2, N_2 and CH_4 were detected by TCD using a Porapak-Q GS-Q and CP-Molsieve 5 Å columns. Hydrocarbons were detected by the FID detector using a HP-Plot Al_2O_3 KCl column.

The liquid phase was analyzed by high-performance liquid chromatography (1260 Infinity II LC System, Agilent technologies) equipped with a refractive index detector. The separation of the products was carried out in an Agilent Hi-Plex H ion exclusion column (300 mm × 7.7 mm) with diluted sulfuric acid (5 mM) as the mobile phase at a flow rate of 0.6 mL/min and a temperature of 60 °C. External standard calibration with all foreseen reaction products was used.

The equations applied to evaluate the catalyst performance during aqueous phase reforming in batch conditions are shown in Table S2.

2.3.2. Continuous reactor testing

Aqueous phase reforming of ethylene glycol was conducted in continuous flow in a stainless-steel tubular reactor (internal diameter =15 mm; length = 385 mm). About 0.3 g of catalyst was sieved (125–250 μm) diluted with SiC (125–250 μm, 1:1 dilution in weight) and held in place with a stainless-steel frit and quartz wool plugs. Before the reaction, the catalyst was reduced *in situ* at 300 °C (heating rate 5 °C/min) in 10 % H_2/N_2 flow (100 mL/min) for 1 h. Then, N_2 was used to pressurize the system to 30 bars, and to regulate the pressure at a flow of 25 mL/min using a back pressure regulator. A 6 wt% ethylene glycol solution was introduced at 0.17 mL/min (2.0 h^{-1} weight hourly space velocity WHSV) in an up-flow configuration. The reaction was carried out at 225 °C. The evolution of the reaction products was monitored by an on-line gas chromatograph (Agilent 8890) equipped with a thermal conductivity detector (TCD) and a flame ionization detector (FID) using CP-Sil 5 CB, CP-Molsieve 5 Å and Haysep-A columns for separation of the components. Samples of the liquid phase were taken every hour and analyzed by an offline HPLC (described in Section 2.3.1). A schematic diagram of the experimental setup is provided in Fig. S2.

The equations used to quantify the catalyst performance during continuous operation are summarized in Table S3.

3. Results and discussion

3.1. Catalyst characterization

Textural characterization of the CNF was carried out to observe the differences in the CNF subjected to various surface treatments. The surface morphology of the as-synthesized catalysts is presented in Fig. S3, indicating the graphite layered structure perpendicular to the fiber axis, typical of platelet carbon nanofibers. The BET specific surface areas are summarized in Table 1, including carbon, oxygen and nitrogen content determined by XPS (at%).

The carbon supports are mainly mesoporous, with only minor differences in surface area. The oxidized carbon nanofibers (CNF-ox) show a higher surface area that decreases with the subsequent heat treatment or nitrogen functionalization of the carbon support. The most notable variation is a 15 % decrease in surface area after nitrogen functionalization of the carbon nanofibers.

The chemical composition and Pt dispersion of the synthesized catalysts are presented in Table 2. For the monometallic samples, Pt dispersion is relatively high and comparable for the different CNF supports. Similar results can be observed for the bimetallic samples, although introducing Mn lower the CO uptake of the catalyst, which is reflected in the values of dispersion. A possible explanation is that this lower CO uptake is a result of a physical blockage, where Mn covers the platinum atoms, as it was suggested by Jain et al. [33].

The XRD patterns of the catalysts are presented in Fig. 1. All samples showed the characteristic high-intensity graphite (002) peak at $2\theta = 26.2°$, which is associated with the graphitic structure of the carbon nanofibers (Fig. S5). Characteristic diffraction peaks of the Pt fcc structure were mainly observed in the catalyst with CNF-ox as support. No Pt diffraction peaks were detected in the N-CNF samples, indicating that the nanoparticles are well dispersed on this support.

From the STEM images (Fig. 2) a bimodal particle size distribution can be seen for the catalysts supported on CNF-HT. A large fraction of the Pt is finely dispersed on the surface, but a significant fraction of larger particles can also be observed in the images. The bimodal particle size distribution can be related to the discrepancy observed in the estimation of average crystallite size from XRD and chemisorption, which can be explained by the size detection limit of XRD. Only the large particles are detected by XRD, whereas the finely dispersed Pt fraction leads to relatively high dispersion values (35–50 %).

These observations indicate that the deposition of Pt by impregnation is affected by the surface functionalization of the carbon support, leading to larger aggregation of Pt nanoparticles when there is a high content of surface oxygen groups.

Several reports [10,34,35] have suggested that electrostatic interaction between the metal precursor and the heteroatoms present on the carbon surface have an effect on the dispersion of the nanoparticles during preparation of the catalyst. For impregnation, it is reported that oxygen-containing groups on the surface can be used as anchoring sites for the metal particles, preventing aggregation. However, when using an

Table 1
Textural properties and elemental composition of the functionalized CNF.

Support	BET surface area (m^2/g)	C (at%)	O (at%)	N (at%)
CNF	197	-	-	-
CNF-ox	209	95.0	5.0	-
CNF-HT	195	96.4	3.5	-
N-CNF	174	96.4	1.7	1.9

Table 2
Pt dispersion, metal loading and average particle size determined by CO chemisorption, MP-AES and XRD.

Catalyst	CO uptake (μmol g^{-1})[a]	Pt dispersion (+/- 1)[a]	Metal loading (±0.1 %)[b]		Pt particle size (nm)[a]	Crystallite size (nm)[c]
			Pt	Mn		
Pt CNF-ox	48.5	39	2.9		3	27
Pt CNF-HT	72.4	50	2.8	-	2	7
Pt N-CNF	52.1	40	2.5	-	3	-
PtMn CNF-ox	47.3	37	2.9	0.8	3	22
PtMn CNF-HT	45.9	34	2.6	0.8	3	16
PtMn N-CNF	46.0	35	2.6	0.8	3	-

[a] CO chemisorption.
[b] MP-AES.
[c] XRD using the Scherrer equation.

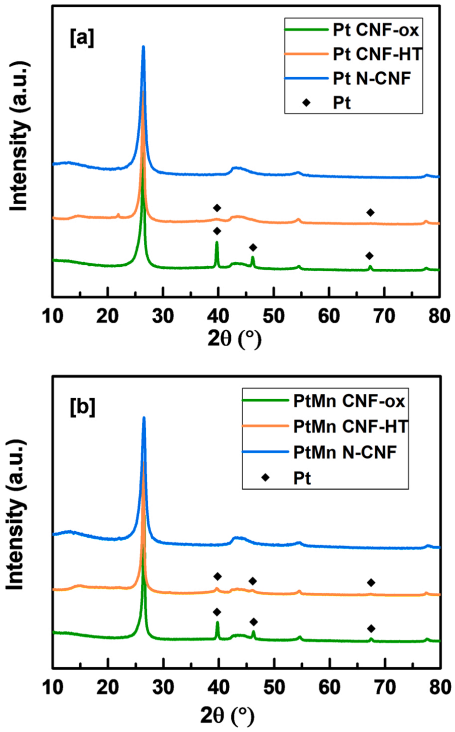

Fig. 1. [a] XRD patterns of monometallic catalysts (Pt). [b] XRD patterns of bimetallic catalysts (PtMn) supported on CNF-ox, CNF-HT, and N-CNF. The diffraction peaks of Pt metal are indicated in the figure.

anionic precursor such as $Pt(Cl_6)^{-2}$, the negatively charged ions could be repelled from the surface by acidic oxygen functional groups (such as carboxylic acids), favoring aggregation of Pt particles [10]. Thus, the formation of larger particles can be facilitated in CNF-ox and CNF-HT during impregnation. And it is suggested that the aggregation of the particles increases with the amount of oxygen content on the carbon surface, observing larger particles for the CNF-ox catalyst with 1.5 %at more oxygen than CNF-HT.

Detailed XPS characterization of the N-doped sample allowed for determination of the nitrogen species on the carbon surface. The XPS of the N-CNF support in the N 1 s region (Fig. 3[a]) indicates the presence of oxidized nitrogen species (402.7 eV), quaternary nitrogen species (401 eV), pyrrolic nitrogen (399.5 eV) and pyridinic nitrogen (398.4 eV) [36], in which the pyridinic functional groups were found to be the most abundant species on the surface (41.8 %). The concentration of individual nitrogen species on the surface of the catalyst is summarized in Table S4. Pyridinic nitrogen is known to be an electron acceptor when it is located on carbon vacancy sites [37,38]. It has been suggested that this nitrogen species have a strong donor-acceptor interaction with Pt nanoparticles by decreasing the electron density of Pt [39].

The N 1 s spectrum of Pt N-CNF (Fig. 3 [b]) shows a decrease in the fraction of pyridinic nitrogen groups (12.6 %) as well as an apparent drop in the overall N content (from 1.9 at% in N-CNF to 1.5 at% in Pt N-CNF) on the surface of the catalyst after deposition of Pt on the support. The loss in N content and specifically that of pyridinic N can be attributed to a preferential anchoring of the Pt nanoparticles on these sites, as has been observed in previous studies for other metals [40,41]. For the bimetallic catalyst (PtMn N-CNF in Fig. 3[c]), it is observed that the fraction of pyridinic nitrogen does not change significantly (44 %), while the overall N content drops from 1.9 %at for N-CNF to 1.4 %at for PtMn N-CNF. This finding indicates that Mn might not be selectively deposited on the pyridinic sites but randomly on all the functional N sites of the carbon.

XPS measurements were carried out to investigate the chemical valence of the Pt phase. The analysis was performed on the reduced catalysts before and after APR. This means that the catalysts were exposed to air when transported to the XPS chamber. The Pt in the catalysts is however still predominantly in the reduced state (*ca.* 80 %, see Table 3). It is thus assumed that the state of Pt in the catalysts is representative for the active state during reaction.

The binding energy of Pt species in the reduced samples is summarized in Table 3 and Fig. 4. From the deconvolution of the Pt regional spectra (Fig. S6), no apparent shift of the binding energy of Pt is observed when comparing Pt N-CNF with Pt CNF-HT. These results indicate that there is no change of the Pt electronic state due to the presence of nitrogen groups on the carbon surface. Previously, it has been observed that the typical binding energy of metallic platinum at Pt 4 $f_{7/2}$ (71.1 eV) is exceeded when platinum is supported on N-containing carbon, and that the Pt binding energy increases with higher content of N groups on the carbon surface [24,42]. Podyacheva et al. [41] reported a shift in Pt binding energies to 72 eV and 72.4 eV for Pt supported on carbon containing 3 at% and 7.5 at% of N, respectively. In this context, electron-withdrawing nitrogen species on the CNF surface may explain an increase in the Pt binding energy by withdrawing electrons from Pt, leading to a decrease in the electron density on the Pt particles. As a result, the Pt nanoparticles are stabilized by strong metal-support interactions leading to higher catalytic activity compared to Pt supported on non-doped carbons [15,34,43]. For the monometallic catalyst in this study, the nitrogen content is most likely too low (1.9 at%) to give a significant effect on the electronic density of Pt. However, a higher Pt^0/Pt^{2+} ratio can be observed for both catalysts supported on N-CNF, suggesting that the presence of nitrogen in the support increases the degree of reduction of Pt metal particles, as was observed for Ru catalysts studied by Gogoi et al. [23].

From Fig. 4 it can be seen that the bimetallic catalysts PtMn CNF-HT and PtMn N-CNF present a shift to higher binding energies for the Pt species. However, the most significant effect is observed in the bimetallic catalyst supported on N-doped CNF, with a shift of approximately 1.5 eV compared to Pt CNF-HT. These results indicate that not only the

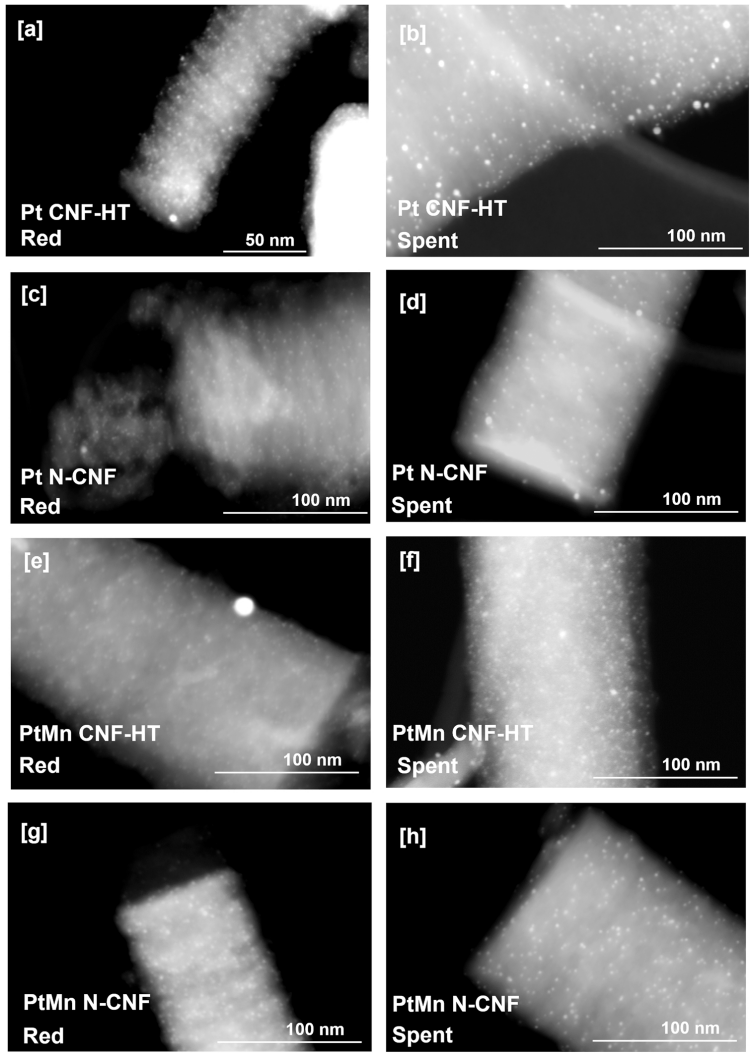

Fig. 2. STEM images of the reduced and spent catalysts after APR of ethylene glycol for 20 h at 225 °C, 30 bar. [a] Pt CNF-HT reduced [b] Pt CNF-HT spent [c] Pt N-CNF reduced [d] Pt N-CNF spent [e] PtMn CNF-HT reduced [f] PtMn CNF-HT spent [g] PtMn N-CNF reduced [h] PtMn N-CNF spent. Note that the scale bar is 50 nm for Fig. 4 [a] and 100 nm for all the other images.

presence of Mn affects the electronic state of Pt [44], but also nitrogen groups present on the surface of the carbon support are further decreasing the electron density on Pt.

Evaluating heat-treated PtMn CNF-HT with no nitrogen groups on the CNF surface and nitrogen-containing PtMn N-CNF allowed to distinguish sources of binding energy shifts in the Pt 4 f region spectra. PtMn CNF-HT shows a shift of 0.8 eV to higher binding energies compared to Pt CNF-HT, which can be attributed to the presence of oxidized Mn species. The XPS Pt 4 f spectrum of PtMn N-CNF shows the combined influence of the presence of Mn as well as electron withdrawing nitrogen groups on the carbon supports, which amounts to an overall shift of 1.5 eV.

In addition, XPS measurements of Mn $2p_{3/2}$ spectra suggested that Mn should be predominantly in oxidized state, although these results must be interpreted with cation due to the low signal to noise ratio (Fig. S7). The presence of oxidize manganese is consistent with earlier observations from Bossola et al. [9], attributing the activation of glycerol in reforming reactions to strong Lewis sites formed by $Mn^{\delta+}$ oxide, leading to higher H_2 production rates.

3.2. APR of ethylene glycol in batch reactor

Screening of the catalysts in APR of 6 %wt ethylene glycol solution at 225 °C was carried out in a batch reactor with an initial pressure of

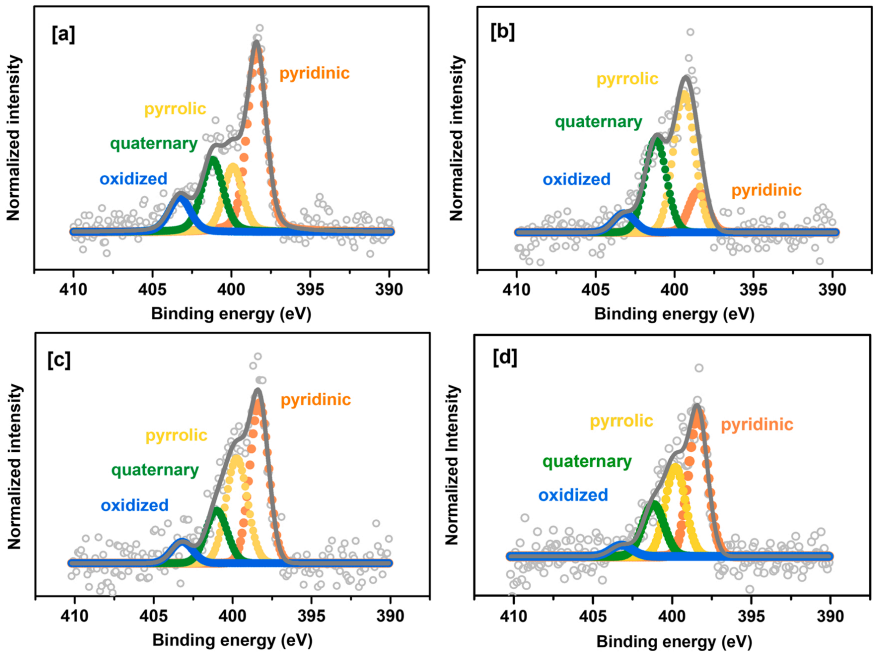

Fig. 3. N1s spectra of [a] N-CNF (1.9 at% nitrogen content) [b] Pt N-CNF (1.5 at% nitrogen content) [c] PtMn N-CNF (1.4 at% nitrogen content) [d] Spent PtMn N-CNF after APR (1.2 at% nitrogen content).

Table 3
Pt 4f7/2 binding energies of Pt species and fractions of Pt species for the reduced catalysts Pt CNF-HT, Pt N-CNF, PtMn CNF-HT, PtMn N-CNF.

	Pt^0 (4 $f_{7/2}$) Binding energy [eV]	Pt^{2+} (4 $f_{7/2}$) Binding energy [eV]	Pt^0 Fraction (+/- 0.01)	Pt^{2+} Fraction (+/- 0.01)	Pt^0/ Pt^{2+} ratio
Pt CNF-HT	70.90	72.68	0.79	0.21	3.8
Pt N-CNF	70.95	72.79	0.82	0.18	4.9
PtMn CNF-HT	71.71	73.20	0.74	0.26	3.2
PtMn N-CNF	72.42	74.18	0.82	0.18	4.9
PtMn CNF-HT spent	72.04	73.99	0.80	0.20	4.0
PtMn N-CNF spent	71.99	73.67	0.77	0.23	3.3

20 bar. Control experiments with CNF-ox, CNF-HT, and N-CNF presented negligible conversion of EG, indicating that the remaining growth catalyst (Fe_3O_4) in the carbon structure (Fe content 0.02–0.1 % wt) did not influence the APR experiments.

The catalytic activity and carbon yield to liquid products of the Pt and PtMn catalysts on the functionalized CNF supports are presented in Figs. 5 and 6. The main products in the gas phase were H_2, CO_2 and CH_4, whereas methanol, ethanol, acetic acid and glycolic acid dominated in the liquid phase. The monometallic samples do not show significant difference in activity and selectivity towards H_2 production for the various surface functionalization of the CNF. A common trend among the catalysts is high H_2 selectivity (>80 %) and low alkane formation (<5 %). The production of acetic acid is suppressed in the presence of N groups on the support. Small organic acids, such as acetic acid, are produced by the rearrangement of glycolic aldehyde, an intermediate product produced by the dehydrogenation of ethylene glycol [1,7]. Thus, it is likely that dehydrogenation of ethylene glycol is less favorable in the presence of N groups on the carbon surface.

In terms of catalytic activity of the monometallic catalysts, van Haasterecht et al. [7] have shown that Pt supported on CNF shows a higher ethylene glycol conversion than Pt supported on alumina in aqueous phase reforming. In addition, it has been demonstrated that the interaction between Pt and CNF results in a positive effect on the catalytic performance of several reactions [15,34,45]. Chen et al. [15] observed a higher Pt binding energy when supported on platelet CNF compared to other carbon supports, attributing the catalytic performance in ammonia borane hydrolysis to electron-deficient Pt particles. In APR, the change in the electronic properties of Pt nanoparticles could decrease the heat of absorption of CO and H_2, which are commonly strongly adsorbed species that block the active sites, thus having more available sites for ethylene glycol conversion [21].

The promoting effect of the N-doping can be clearly observed in the bimetallic samples, with high H_2 selectivity (85.8 %) and H_2 site time yield (22 min^{-1}) obtained for the N-doped catalyst (Table S5). As the mean particle size for all samples is comparable, the effect of nitrogen-doping of the carbon support could be confirmed.

Several lines of observations in previous literature suggest possible reasons for the improved catalytic activity of Pt supported on N-doped carbon. Nitrogen groups on the carbon surface could enable strong metal-support interactions by charge transfer from Pt to the nitrogen groups, as has been observed for pyridinic N [46]. Additional active sites may be formed on the metal-support interface by creating additional

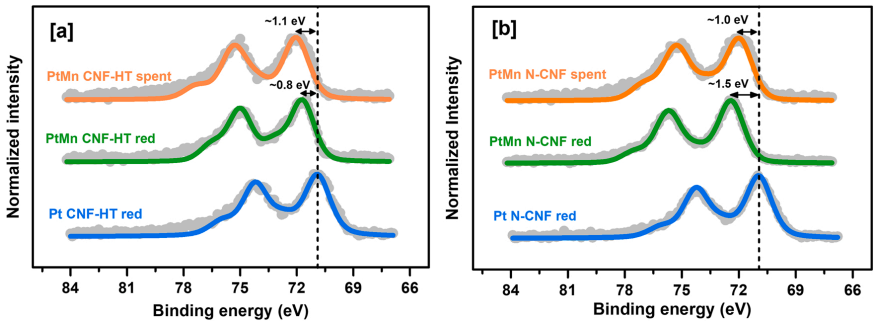

Fig. 4. Pt 4 $f_{7/2}$ spectra of [a] Pt CNF-HT, PtMn CNF-HT catalysts after reduction ex situ and spent PtMn CNF-HT after APR [b] Pt N-CNF, and PtMn N-CNF catalysts after reduction ex situ and spent PtMn N-CNF-HT after APR.

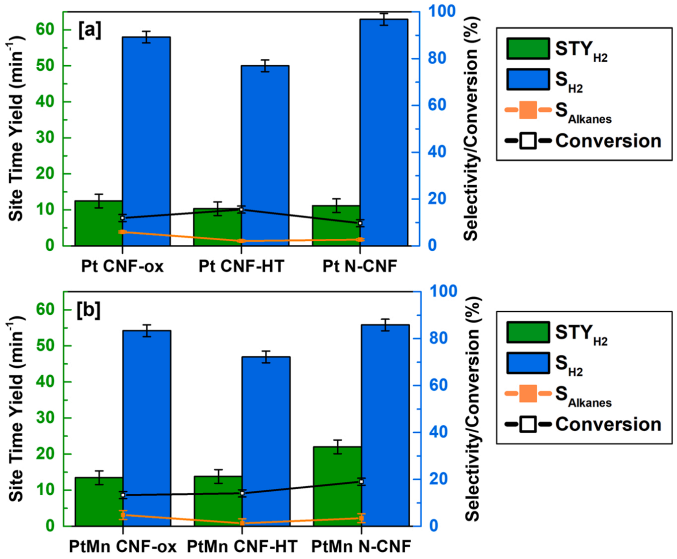

Fig. 5. APR of 6 %wt ethylene glycol (EG) aqueous solution at 225 °C and 20 bar initial pressure obtained in batch reactor. Catalytic conversion of EG, H_2 site time yield ($STYH_2$), H_2 and alkane selectivities for the [a] monometallic Pt catalysts. [b] bimetallic PtMn catalysts. The error bars represent the standard deviation of the experiments.

defects on the carbon surface by incorporation of nitrogen in the carbon structure [41]. N-doped carbon facilitates high dispersion and stability of the metal nanoparticles on the support, with N surface groups acting as anchoring sites for the nanoparticles on the carbon [39,41,47].

In this study, enhancement of the catalytic activity can not only be attributed to the surface functional groups on the carbon support. The addition of Mn promotes the formation of H_2, resulting in higher H_2 site time yield when compared to the monometallic catalyst. From the STEM-EDX maps of our catalyst (Fig. S8), a homogenous distribution of the two metals in on the surface can be observed, suggesting direct interaction between the two metals. As noted by Kim et al., [11] alloy formation between Pt and Mn may be responsible for enhancement of the catalytic activity, increasing H_2 selectivity and improving the stability of the catalyst. In the present study the electronic interaction between PtMn and the N groups contained on the surface of the CNF was confirmed by the XPS analysis (Table 2). Hence, the higher catalytic activity of PtMn N-CNF can be attributed to electron-deficient Pt present on the surface of the CNF.

Harsh hydrothermal conditions are characteristic of aqueous phase reforming and lead to the formation of organic acids in the liquid phase, which lowers the pH of the solution from nearly neutral to pH 3–4. Such conditions increase the risk of metal leaching by oxidation of the active metal phase. Metal leaching of the catalysts was examined by comparing the metal loading of the spent catalysts with the freshly reduced samples. For the bimetallic catalysts, a significant loss of Mn was observed (Table 4). Between 95 % and 97 % of the Mn was lost during 2 h of APR, demonstrating that the functionalization of the carbon support was not sufficient to stabilize the Mn species. However, for both bimetallic and monometallic catalysts, Pt nanoparticles were stable with no significant leaching (<1 %).

Due to the high degree of Mn leaching, the accumulation of soluble Mn species in the reaction media during batch operation may influence

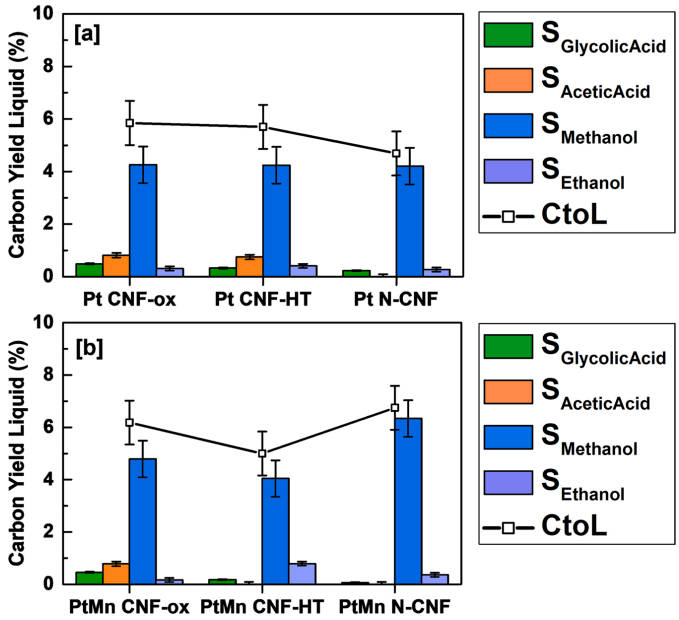

Fig. 6. APR in batch reactor of 6 %wt ethylene glycol (EG) aqueous solution at 225 °C and 20 bar initial pressure. Carbon yield to main liquid products and total conversion of carbon to liquids (CtoL) of the [a] monometallic Pt catalysts [b] bimetallic PtMn catalysts. The error bars represent the standard deviation of the experiments.

Table 4
Metal leaching of the spent catalyst determined by MP-AES.

Catalyst	Metal leaching (±0.1 %)	
	Pt	Mn
Pt CNF-ox	1.0	
Pt CNF-HT	0.0	-
Pt N-CNF	0.0	-
PtMn CNF-ox	0.3	96.3
PtMn CNF-HT	0.0	97.6
PtMn N-CNF	0.0	95.6

the outcome of the APR of EG. Therefore, a control experiment containing soluble Mn species ($Mn(NO_3)_2$ x H_2O) representing the total amount of Mn contained in the catalysts (~ 400 ppm) was carried out. No discernible conversion of ethylene glycol was detected in the batch experiment with the soluble Mn species.

Previous studies on aqueous phase reforming have reported high degrees of metal leaching from the catalyst matrix in similar systems (Pt-Ni, Pt-Mn, Pt-Co) [7,9,18,48]. In some cases, it has been demonstrated that although more that 50 % of the secondary metal is leaching out from the catalyst, the catalyst maintained the activity [49].

3.3. APR of ethylene glycol in continuous flow conditions

It is challenging to evaluate the stability of the catalysts in batch reaction. Accumulation of the products during reaction may favor conditions for deactivation of the catalyst, such as lower pH that can induce leaching of the active phase. Thus, the most active catalysts from the batch tests were studied in a continuous APR setup to further study the catalytic activity and stability. In the limiting case of the highest reaction rate the Weisz-Prater criterion was evaluated to confirm absence of intraparticle mass-transfer limitations (see SI).

Fig. 7 shows the catalytic activity of the catalysts supported on CNF-HT and N-CNF during time on stream expressed by EG conversion, H_2 site time yield (STY), methane selectivity and carbon yield. The reaction conditions were maintained for at least 20 h to reach steady-state performance. As can be seen from conversion and STY_{H2}, the catalyst reached steady-state after approximately 15 h of time on stream.

The main products in the gas phase during APR of ethylene glycol are H_2, CO_2, CO, methane, and ethane. Higher hydrocarbons were not detected in the GC analysis during continuous flow operation. From the gas phase selectivities (Table S6), it can be seen that all samples follow a general trend with low concentrations of CO and methane that decrease with time on stream. The STY_{H2} of all catalysts increased with TOS until reaching steady-state, except for the bimetallic catalyst supported on N-doped carbon which even after 20 h of reaction showed increasing production of hydrogen, which can be associated to lower rates on side-reactions consuming H_2, such as methanation and Fischer–Tropsch synthesis. The catalysts supported on nitrogen-doped CNF showed high H_2 selectivity (90 %), with the highest H_2 selectivity measured for the bimetallic PtMn N-CNF catalyst (96 %).

After 20 h of reaction, the most active catalysts are the PtMn-based catalysts, in which PtMn N-CNF displays the highest H_2 site time yield (15.8 min^{-1}) with the lowest production of alkanes among the catalysts. These results are in agreement with comparable studies where Pt-based catalysts are investigated. Huber et al. [21] studied the effects of addition of a second metal to Pd and Pt-based catalysts supported on alumina: They noticed that most of the bimetallic catalysts (PtNi, PtCo, PtFe) displayed higher turnover frequencies for H_2 production than the monometallic counterparts in aqueous phase reforming of ethylene glycol, showing TOF_{H2} values in the range 7–11 min^{-1}. Bossola et al. [9] studied aqueous phase reforming of glycerol over Pt and PtMn catalysts supported on carbon with TOF_{H2} values between 13 and 17 min^{-1}.

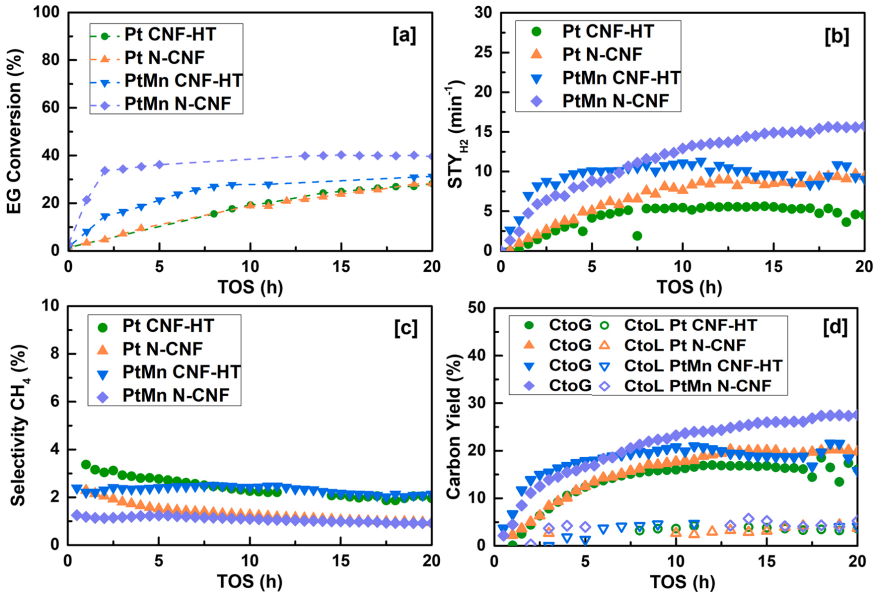

Fig. 7. APR of ethylene glycol (6 %wt) at 225 °C, 30 bar and WHSV= 2 h^{-1}. Evolution of [a] Ethylene glycol conversion (%) [b] H_2 site time yield (min^{-1}) [c] Selectivity to CH_4 [d] Carbon yield to liquid phase and gas phase (%) with time on stream (TOS).

Hence, the observed catalytic activity presented in Fig. 7 is in line with previous observations reported in literature.

The selectivity towards liquid phase products is comparable for the tested catalysts. Organic acids mainly produced during APR by ethylene glycol dehydrogenation followed by molecular rearrangement, such as organic acids [50] are not detected, in contrast to the results from the batch reactor. Methanol and ethanol are still the main by-products in the liquid phase, with ethanol being the most significant component. Ethanol is formed by ethylene glycol dehydration at the catalyst surface followed by hydrogenation [50]. The carbon yield towards liquid products was relatively low, with only between 3 % and 6 % of the carbon present in the feedstock converted to liquid products (Fig. 7 [d]).

All catalysts presented in this study follow similar trends in the selectivity towards gas and liquid phase products, suggesting that the addition of Mn and heteroatoms on the surface of the catalyst support only have minor impact on the product distribution. However, enhancement in the catalytic activity is observed when Mn and N are present in the Pt-based catalysts. These similarities in the composition of the by-products show that APR of ethylene glycol over CNF-supported catalysts correlates with the reaction pathways published previously, initially reported by Dumesic et al. favoring C-C bond cleavage over C-O bond cleavage, resulting in high H_2 selectivities [1,50–52] as presented

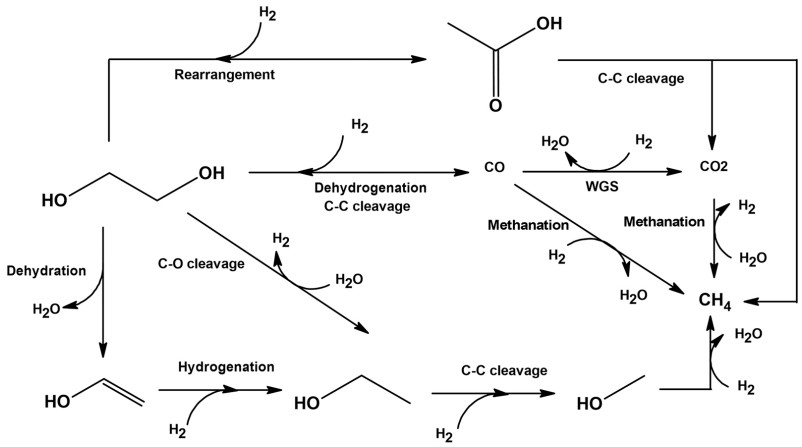

Fig. 8. Reaction scheme for aqueous phase reforming of ethylene glycol.

in the following reaction scheme (Fig. 8).

3.4. Characterization of spent catalysts

To understand the possible role of deactivation due to metal oxidation, leaching and sintering, the spent catalysts were analyzed after being exposed to APR. In continuous operation, significant metal leaching was detected after 20 h of reaction for the Mn-containing samples (Table S7). For PtMn CNF-HT, 97.1 ± 0.1 % of the Mn was lost during APR, while for PtMn N-CNF, the Mn leaching was estimated to be slightly lower at 89.0 ± 0.1 %. This indicates that functionalizing the carbon surface with N-containing groups may help stabilize some of the Mn present in the catalyst. In the case of Pt, no significant leaching was detected (<0.01 %) (Table S7).

In the current study, STEM-EDX analysis revealed the presence of Pt and Mn in the catalysts and evidence of the proximity between Mn and Pt in the reduced catalysts (Figs. S8 and S9).

Furthermore, from the STEM images in Fig. 4, the particles seem homogeneously distributed on the carbon support for all the samples, and no significant changes are observed for the spent catalysts. However, a slight decrease in the dispersion after reaction (Table 5) is observed, suggesting minor sintering of the metal particles caused by the harsh hydrothermal conditions in APR.

XPS characterization of the spent N-doped bimetallic catalyst after APR was carried out, and the results are presented in Figs. 3 and 4. The N 1 s spectrum of the spent PtMn N-CNF (Fig. 3 [d]) shows similar fractions of oxidized, quaternary, pyrrolic, and pyridinic nitrogen functional groups with an overall N content of 1.2 %at. The N content is comparable to the catalyst after reduction, indicating that the nitrogen species located on the surface of the CNF are sufficiently stable to withstand the hydrothermal conditions of APR.

Despite the substantial loss of Mn during the reaction (Fig. S9) the catalytic activity of the samples is maintained as can be seen in Fig. 7 and from the Pt 4 $f_{7/2}$ spectra of the spent bimetallic catalyst after APR (Table 4) it still can be seen a shift to higher binding energies of approximately 1.0 eV for Pt when compared to the monometallic catalyst. Therefore, it seems that the leached Mn species from the catalyst surface have a negligible impact on catalyst activity. Bossola *et al.* [9] observed similar results, where only 5 % of the Mn was retained on the catalyst after APR. It was suggested that Pt was alloyed with the small amount of Mn still present in the sample, generating a promoting effect. The minor fraction of Mn in the catalyst positively impacts the catalytic activity toward H_2 production. Thus, it can be considered that the remaining Pt particles expose a larger fraction of low coordination surface atoms after Mn leaching. These low coordination surface atoms can be preferential sites for aqueous phase reforming of ethylene glycol.

4. Conclusions

The activity, selectivity, and stability of Pt-based catalysts for hydrogen production by APR of ethylene glycol were evaluated, initially by screening the catalyst in a batch setup, followed by further experiments in continuous flow conditions. It is observed that the activity of the catalysts was influenced by the nitrogen contained in the surface of the CNF support and promotion with manganese. In this context, it was demonstrated that bimetallic catalysts such as PtMn supported on N-doped carbon nanofibers are active and selective catalysts in aqueous phase reforming of ethylene glycol, with H_2 site time yield of 15.8 min^{-1} at 225 °C and 30 bar pressure. The enhancement in catalytic activity could be attributed to metal-support interactions between PtMn and N-doped carbon nanofibers, decreasing the electron density on Pt and promoting H_2 formation. The addition of Mn to the Pt-based catalysts further decreased the electron density of Pt by metal-metal interaction and enhancing the catalytic activity.

After 20 h of continuous-flow APR, up to 97 ± 0.1 % of Mn was lost to leaching. N-doping of the support was able to slightly suppress the metal leaching, with 89 ± 0.1 % of Mn lost. However, it was found that Mn leaching does not negatively affect the catalytic activity, indicating that a small fraction of Mn is sufficient to improve the catalytic activity of Pt.

Table 5
Metal dispersion and average Pt particle size by CO chemisorption of reduced and spent catalyst.

Catalyst	Pt dispersion (+/- 1 %)		Pt particle size (nm)	
	Reduced	Spent	Reduced	Spent
Pt CNF-HT	50	44	2	3
Pt N-CNF	40	35	3	3
PtMn CNF-HT	34	35	3	3
PtMn N-CNF	35	31	3	4

CRediT authorship contribution statement

Monica Pazos Urrea: Conceptualization, Methodology, Validation, Formal analysis, Investigation, Writing – original draft, Writing – review & editing, Visualization. **Felix Herold:** Conceptualization, Validation, Formal analysis, Investigation, Resources, Writing – review & editing, Visualization. **De Chen:** Conceptualization, Validation, Supervision. **Magnus Rønning**: Conceptualization, Validation, Writing – review & editing, Supervision, Project administration, Funding acquisition.

Declaration of Competing Interest

The authors declare that they have no known competing financial interests or personal relationships that could have appeared to influence the work reported in this paper.

Data availability

Data will be made available on request.

Acknowledgements

This work was financially supported by the European Union's Horizon 2020 Research and Innovation Program under the Marie Skłodowska-Curie Actions−Innovative Training Networks (MSCA-ITN) BIKE project, Grant Agreement 813748. FH acknowledges a fellowship within the Walter-Benjamin-program of the Deutsche Forschungsgemeinschaft (DFG, German Research Foundation, project number 471263729). The Research Council of Norway is acknowledged for the support to the Norwegian Micro- and Nano-Fabrication Facility, NorFab (project number 295864), and the national infrastructure NorBioLab (project number 270038). Trung Dung Tran at Johnson Matthey is acknowledged for performing the TEM study.

Appendix A. Supporting information

Additional results of XPS, STEM, catalytic testing and detailed experimental procedures concerning XPS. Supplementary data associated with this article can be found in the online version at doi:10.1016/j.cattod.2023.114066.

References

[1] R.D. Cortright, R.R. Davda, J.A. Dumesic, Nature 418 (2002) 964–967.
[2] K. Oshiro, S. Fujimori, Appl. Energy 313 (2022), 118803.
[3] B. Roy, K. Loganathan, H.N. Pham, A.K. Datye, C.A. Leclerc, Int. J. Hydrog. Energy 35 (2010) 11700–11708.
[4] A.V.-H. Soares, G. Perez, F.B. Passos, Appl. Catal. B Environ. 185 (2016) 77–87.
[5] A.O. Menezes, M.T. Rodrigues, A. Zimmaro, L.E.P. Borges, M.A. Fraga, Renew. Energy 36 (2011) 595–599.
[6] J.W. Shabaker, G.W. Huber, R.R. Davda, R.D. Cortright, J.A. Dumesic, Catal. Lett. 88 (2003) 1–8.

[7] T. van Haasterecht, C.C.I. Ludding, K.P. de Jong, J.H. Bitter, J. Energy Chem. 22 (2013) 257–269.
[8] M.-C. Kim, T.-W. Kim, H.J. Kim, C.-U. Kim, J.W. Bae, Renew. Energy 95 (2016) 396–403.
[9] F. Bossola, X.I. Pereira-Hernández, C. Evangelisti, Y. Wang, V. Dal Santo, J. Catal. 349 (2017) 75–83.
[10] A. Volynkin, M. Rønning, E.A. Blekkan, Top. Catal. 58 (2015) 854–865.
[11] H.-D. Kim, H.J. Park, T.-W. Kim, K.-E. Jeong, H.-J. Chae, S.-Y. Jeong, C.-H. Lee, C.-U. Kim, Int. J. Hydrog. Energy 37 (2012) 8310–8317.
[12] J. Gan, Z. Huang, W. Luo, W. Chen, Y. Cao, G. Qian, X. Zhou, X. Duan, J. Energy Chem. 52 (2021) 33–40.
[13] R. Zheng, Y. Zhao, H. Liu, C. Liang, G. Cheng, Carbon 44 (2006) 742–746.
[14] I. Kvande, D. Chen, T.-J. Zhao, I.M. Skoe, J.C. Walmsley, M. Rønning, Top. Catal. 52 (2009) 664–674.
[15] W. Chen, S. Chen, G. Qian, L. Song, D. Chen, X. Zhou, X. Duan, J. Catal. 389 (2020) 492–501.
[16] C.F. Sanz-Navarro, P.-O. Åstrand, D. Chen, M. Rønning, A.C.T. van Duin, T. Jacob, W.A. Goddard, J. Phys. Chem. A 112 (2008) 1392–1402.
[17] G. Pipitone, G. Zoppi, R. Pirone, S. Bensaid, Int. J. Hydrog. Energy (2021). S0360319921037848.
[18] M. El Doukkali, A. Iriondo, J.F. Cambra, I. Gandarias, L. Jalowiecki-Duhamel, F. Dumeignil, P.L. Arias, Appl. Catal. Gen. 472 (2014) 80–91.
[19] D.L. King, L. Zhang, G. Xia, A.M. Karim, D.J. Heldebrant, X. Wang, T. Peterson, Y. Wang, Appl. Catal. B Environ. 99 (2010) 206–213.
[20] X. Wang, N. Li, L.D. Pfefferle, G.L. Haller, Catal. Today 146 (2009) 160–165.
[21] G.W. Huber, J.W. Shabaker, S.T. Evans, J.A. Dumesic, Appl. Catal. B Environ. 62 (2006) 226–235.
[22] L.I. Godina, A.V. Kirilin, A.V. Tokarev, I.L. Simakova, D.Y. Murzin, Ind. Eng. Chem. Res. 57 (2018) 2050–2067.
[23] P. Gogoi, N. Kanna, P. Begum, R.C. Deka, S.C.V. V, T. Raja, ACS Catal. 10 (2020) 2489–2507.
[24] K. Jiang, X.-Y. Ma, S. Back, J. Zhao, F. Jiang, X. Qin, J. Zhang, W.-B. Cai, CCS Chem. 3 (2021) 241–251.
[25] A. García-Baldoví, L. Peng, A. Santiago-Portillo, A.M. Asiri, A. Primo, H. García, ACS Appl. Energy Mater. 5 (2022) 9173–9180.
[26] Z. Zheng, Y. Fang, J. Yang, L. Ma, Q. Meng, X. Lin, Y. Liu, Q. Zhang, T. Wang, Int. J. Hydrog. Energy 47 (2022) 950–961.
[27] D. Chen, K.O. Christensen, E. Ochoa-Fernández, Z. Yu, B. Tøtdal, N. Latorre, A. Monzón, A. Holmen, J. Catal. 229 (2005) 82–96.
[28] S. Brunauer, P.H. Emmett, E. Teller, J. Am. Chem. Soc. 60 (1938) 309–319.
[29] M. Fadoni, L. Lucarelli, Stud. Surf. Sci. Catal. 120 (1999) 177–225.
[30] S. Gražulis, D. Chateigner, R.T. Downs, A.F.T. Yokochi, M. Quirós, L. Lutterotti, E. Manakova, J. Butkus, P. Moeck, A. Le Bail, J. Appl. Crystallogr. 42 (2009) 726–729.
[31] C.F. Holder, R.E. Schaak, ACS Nano 13 (2019) 7359–7365.
[32] D.A. Shirley, Phys. Rev. B 5 (1972) 4709–4714.
[33] S.K. Jain, E.M. Crabb, L.E. Smart, D. Thompsett, A.M. Steele, Appl. Catal. B Environ. 89 (2009) 349–355.
[34] N. Muthuswamy, J.L.G. de la Fuente, P. Ochal, R. Giri, S. Raaen, S. Sunde, M. Rønning, D. Chen, Phys. Chem. Chem. Phys. 15 (2013) 3803–3813.
[35] C. Prado-Burguete, A. Linares-Solano, F. Rodríguez-Reinoso, C.S.-M. de Lecea, J. Catal. 115 (1989) 98–106.
[36] K. Friedel Ortega, R. Arrigo, B. Frank, R. Schlögl, A. Trunschke, Chem. Mater. 28 (2016) 6826–6839.
[37] M. Zhao, Y. Xia, J.P. Lewis, R. Zhang, J. Appl. Phys. 94 (2003) 2398–2402.
[38] T. Kondo, S. Casolo, T. Suzuki, T. Shikano, M. Sakurai, Y. Harada, M. Saito, M. Oshima, M.I. Trioni, G.F. Tantardini, J. Nakamura, Phys. Rev. B 86 (2012), 035436.
[39] L. Jia, D.A. Bulushev, O.Yu Podyacheva, A.I. Boronin, L.S. Kibis, E.Yu Gerasimov, S. Beloshapkin, I.A. Seryak, Z.R. Ismagilov, J.R.H. Ross, J. Catal. 307 (2013) 94–102.
[40] L.P.L. Gonçalves, M. Meledina, A. Meledin, D.Y. Petrovykh, J.P.S. Sousa, O.S.G. P. Soares, Y.V. Kolen'ko, M.F.R. Pereira, Carbon 195 (2022) 35–43.
[41] O.Yu Podyacheva, A.S. Lisitsyn, L.S. Kibis, A.I. Stadnichenko, A.I. Boronin, E. M. Slavinskaya, O.A. Stonkus, S.A. Yashnik, Z.R. Ismagilov, Catal. Today 301 (2018) 125–133.
[42] J. Zhao, C. Fu, K. Ye, Z. Liang, F. Jiang, S. Shen, X. Zhao, L. Ma, Z. Shadike, X. Wang, J. Zhang, K. Jiang, Nat. Commun. 13 (2022) 685.
[43] Y.-H. Li, T.-H. Hung, C.-W. Chen, Carbon 47 (2009) 850–855.
[44] Z. Wu, B.C. Bukowski, Z. Li, C. Milligan, L. Zhou, T. Ma, Y. Wu, Y. Ren, F. H. Ribeiro, W.N. Delgass, J. Greeley, G. Zhang, J.T. Miller, J. Am. Chem. Soc. 140 (2018) 14870–14877.
[45] L. Calvillo, M. Gangeri, S. Perathoner, G. Centi, R. Moliner, M.J. Lázaro, J. Power, Sources 192 (2009) 144–150.
[46] D.A. Bulushev, M. Zacharska, A.S. Lisitsyn, O.Yu Podyacheva, F.S. Hage, Q. M. Ramasse, U. Bangert, L.G. Bulusheva, ACS Catal. 6 (2016) 3442–3451.
[47] T. Maiyalagan, B. Viswanathan, U.V. Varadaraju, Electrochem. Commun. 7 (2005) 905–912.
[48] P.J. Dietrich, F.G. Sollberger, M.C. Akatay, E.A. Stach, W.N. Delgass, J.T. Miller, F. H. Ribeiro, Appl. Catal. B Environ. 156–157 (2014) 236–248.
[49] Z. Wei, A. Karim, Y. Li, Y. Wang, ACS Catal. 5 (2015) 7312–7320.
[50] J.W. Shabaker, J.A. Dumesic, Ind. Eng. Chem. Res. 43 (2004) 3105–3112.
[51] R.R. Davda, J.W. Shabaker, G.W. Huber, R.D. Cortright, J.A. Dumesic, Appl. Catal. B Environ. 56 (2005) 171–186.
[52] D.J.M. de Vlieger, B.L. Mojet, L. Lefferts, K. Seshan, J. Catal. 292 (2012) 239–245.

Nitrogen-containing carbon nanofibers as supports for bimetallic Pt-Mn catalysts in aqueous phase reforming of ethylene glycol

Supplementary Information

Monica Pazos Urrea, Felix Herold, De Chen, Magnus Rønning*

Department of Chemical Engineering, Norwegian University of Science and Technology

7491Trondheim, Norway

*Corresponding Author: Magnus Rønning, Email: magnus.ronning@ntnu.no

EXPERIMENTAL

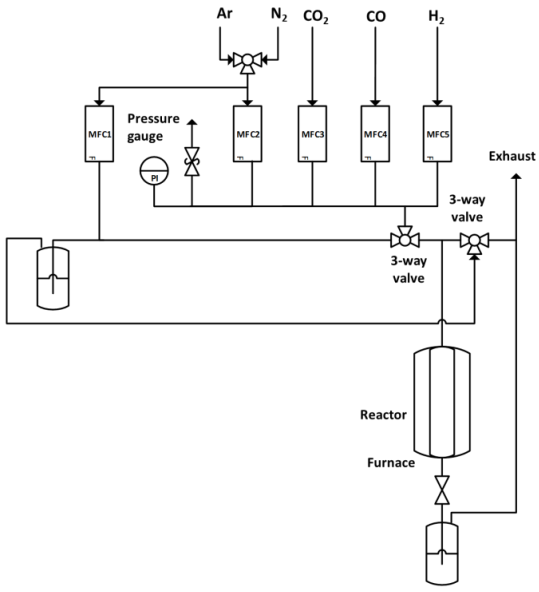

Figure S 1. Schematic diagram of the setup utilized for gasification-assisted nitrogen doping of carbon nanofibers (CNF).

XPS fitting

For the analysis of Pt species, the distance between the spin-orbit splitting is set to 3.3 eV to represent $4f_{7/2}$ and $4f_{5/2}$, and the intensity ratio was constrained to 0.8 [1]. FWHM of Pt 4f was set to be equal for all the functions during the fitting.

For the analysis of Mn species, Mn $2p_{3/2}$ (639± 0.4) contribution was fitted with doublets of two profiles with a fixed intensity ratio of 0.35, with the distance between the two spin-orbit splitting set to 11.7 eV to represent $2p_{3/2}$ and $2p_{1/2}$ [1]. FWHM of Mn $2p_{3/2}$ was set to be equal for all the functions during the fitting.

Table S 1. Band assignments and fitting parameters of XPS analysis

Species	Binding energy (eV)	Full width at half-maximum (FWHM)				
		N-CNF	Pt CNF-HT	Pt N-CNF	PtMn CNF-HT	PtMn N-CNF
Oxidized N	403.4 ± 0.2	0.8	0.8	0.8	0.8	0.8
Quaternary N	401.0 ± 0.2	0.8	0.8	0.8	0.8	0.8
Pyrrolic N	399.7 ± 0.2	0.8	0.8	0.8	0.8	0.8
Pyridinic N	398.3 ± 0.2	0.7	0.7	0.7	0.7	0.7
Pt $4f_{7/2}$ - Pt^{o}	71.2 ± 0.2	-	0.8	0.8	0.7	0.8
Pt $4f_{7/2}$ - Pt^{+2}	72.4 ± 0.2	-	0.8	0.8	0.7	0.8
MnO_x $2p_{3/2}$	641.4 ± 0.2	-	-	-	1.0	1.0
MnO_x $2p_{3/2}$	643.2 ± 0.2	-	-	-	1.0	1.0

Table S 2. Parameters and equations applied to evaluate APR batch performance

Equation	Parameter	Formula
1	Conversion	$X_{EG}(\%) = \frac{mol_{EG\ initial} - mol_{EG\ final}}{mol_{EG\ initial}}$
2	Hydrogen selectivity – Carbon based	$S_{H2}(\%) = \frac{mol\ H_{2\ produced}}{{C_{total,g}}^{a}}\ x\frac{1}{R^{b}}x100$
3	Carbon based selectivity	$S_{i,g}\ (\%) = \frac{{C_{i,g}}^{c}}{{C_{total,g}}^{a}}\ x\ 100$
4	Hydrogen site time yield	$STY_{H2}(min^{-1}) = \frac{{H_{2\ production\ rate}}^{d}\ {Mw_{Pt}}^{e}}{{D_{Pt}}^{f}{W_{cat}}^{g}{X_m}^{h}}$
5	Carbon yield to liquid products	$C_{i,L}\ (\%) = \frac{{C_{i,L}}^{j}}{{C_{EG\ inital}}^{k}}\ x\ 100$
6	Carbon yield to gaseous products	$C_{i,g}\ (\%) = \frac{{C_{i,g}}^{c}}{{C_{EG\ inital}}^{k}}\ x\ 100$

[a] Total carbon present in the gas phase
[b] Stoichiometric reforming ratio for EG $R = H_2/CO_2 = 5/2$
[c] Total carbon in each gaseous product (i)
[d] Moles of H_2 produced divided by the duration of the experiment (120 min)
[e] Molecular weight of Pt
[f] Pt dispersion estimated by CO chemisorption (%)
[g] Amount of catalyst (g)
[h] Weight fraction of Pt in the catalyst (wt%)
[j] Total carbon in each liquid product (i)
[k] Total carbon contained in the feed stream

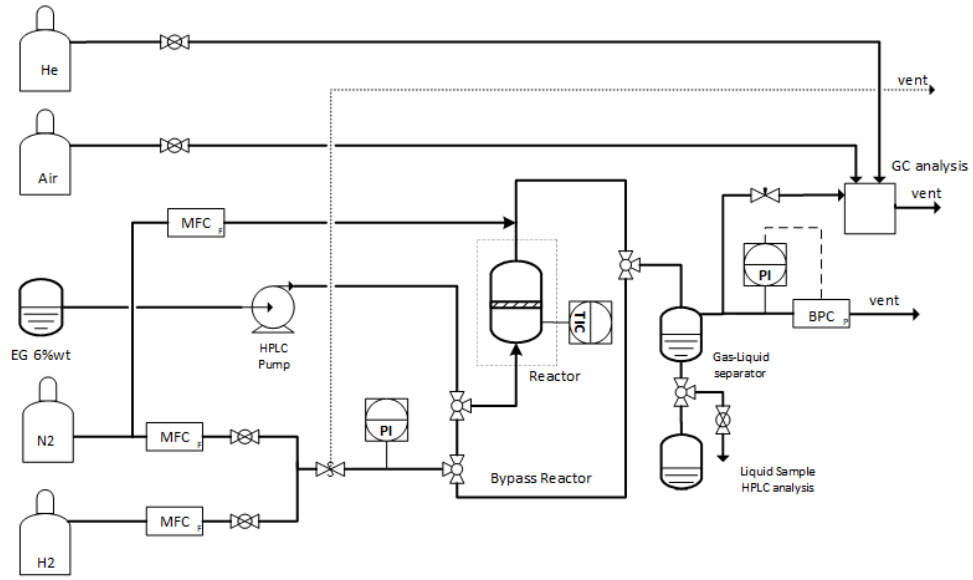

Figure S 2. Schematic diagram of the continuous setup utilized for aqueous phase reforming of ethylene glycol.

Table S 3. Parameters and formulas applied to evaluate APR continuous setup performance

Equation	Parameter	Formula
1	Conversion	$X_{EG}(\%) = \frac{F_{EGin}(mol/min) - F_{EGout}(mol/min)}{F_{EGin}(mol/min)}$
2	Hydrogen selectivity (%) – Carbon based	$S_{H2}(\%) = \frac{F_{H2\,produced}(mol/min)}{FC_{total,g}{}^{a}} x \frac{1}{R^b} x100$
3	Carbon based selectivity (%)	$S_{i,g}(\%) = \frac{FC_{i,g}{}^{c}}{FC_{total,g}{}^{a}} x\,100$
4	Hydrogen site time yield (min^{-1})	$STY_{H2}(min^{-1}) = \frac{F_{H2produced}(mol/min)\ Mw_{Pt}{}^{d}}{D_{Pt}{}^{e} W_{cat}{}^{f} X_m{}^{g}}$
5	Carbon yield to liquid products	$FC_{i,L}(\%) = \frac{FC_{i,L}{}^{h}}{FC_{EGin}{}^{j}} x\,100$
6	Carbon yield to gaseous products	$C_{i,g}(\%) = \frac{FC_{i,g}{}^{c}}{FC_{EGin}{}^{j}} x\,100$

[a] Total flow of carbon present in the gas phase (mol/min)
[b] Stoichiometric reforming ratio for EG $R = H_2/CO_2 = 5/2$
[c] Total flow of carbon in each gaseous product (i) (mol/min) – Estimated by the N_2 flow used as internal standard.
[d] Molecular weight of Pt (g/mol)
[e] Pt dispersion estimated by CO chemisorption
[f] Amount of catalyst (g)
[g] Weight fraction of Pt in the catalyst (%wt)
[h] Total flow of carbon present in each liquid product (i)
[j] Total inlet flow of carbon contained in the feed stream

A nitrogen flow of 25 mL/min is used as an internal standard to calculate the outlet flow rate of gaseous products based on the measured composition of each component by gas chromatography. Thus, the gas phase flow rate is estimated using the ideal gas law, assuming room temperature of 25°C (298.15 K).

Since the APR in continuous flow were performed in up-flow configuration, with diluted ethylene glycol feed and at moderate conversion levels, the outlet liquid flow rate was assumed to be equal to the inlet flow.

RESULTS AND DISCUSSION

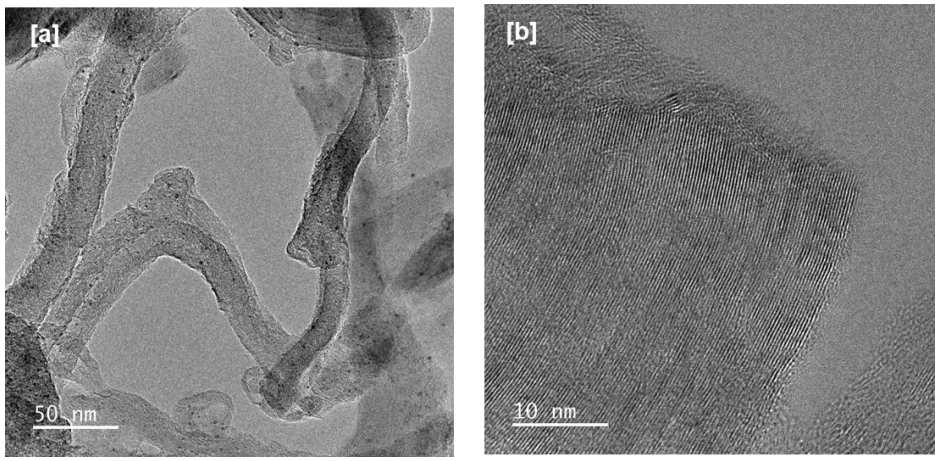

Figure S 3. TEM images of PtMn CNF-HT revealing the platelet morphology of the CNF used as catalyst support. [a] Low magnification image indicating the typical size of the platelet fibers. [b] High-resolution image showing the platelet structure.

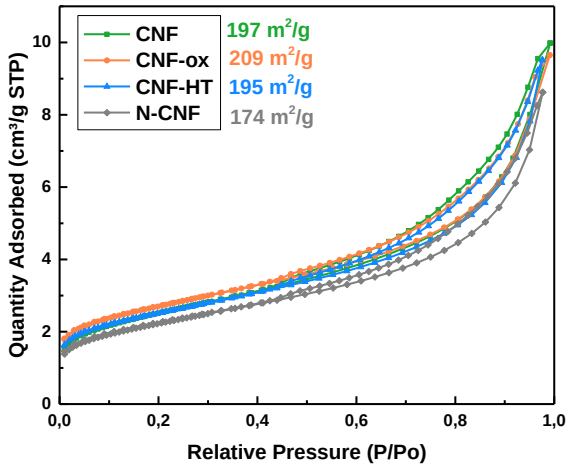

Figure S 4. N_2 physisorption isotherms and specific surface area (BET) of CNF, CNF-ox, CNF-HT, and N-CNF.

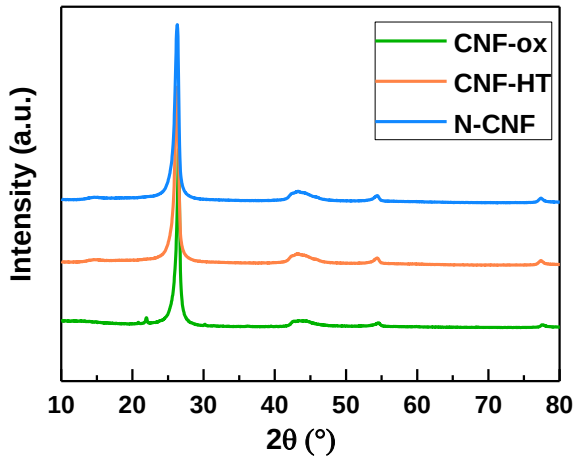

Figure S 5. XRD patterns of functionalized carbon nanofibers

Table S 4. Relative atomic percentage (at%) of carbon, oxygen, and nitrogen. Including the fraction of oxidized nitrogen species, quaternary nitrogen species, pyrrolic nitrogen, and pyridinic nitrogen as quantified by XPS analysis.

Catalyst	Relative atomic percentage (at%)			N species fraction (%)			
	C	O	N	Oxidized nitrogen	quaternary nitrogen	pyrrolic nitrogen	pyridinic nitrogen
N-CNF	96.4	1.7	1.9	10.6	22.1	17.9	49.3
Pt N-CNF	96.7	1.8	1.5	6.7	32.7	48.1	12.6
PtMn N-CNF	97.4	1.2	1.4	6.6	16.5	32.8	44.0
PtMn N-CNF spent	97.7	1,1	1.2	4.1	19.1	30.6	46.2

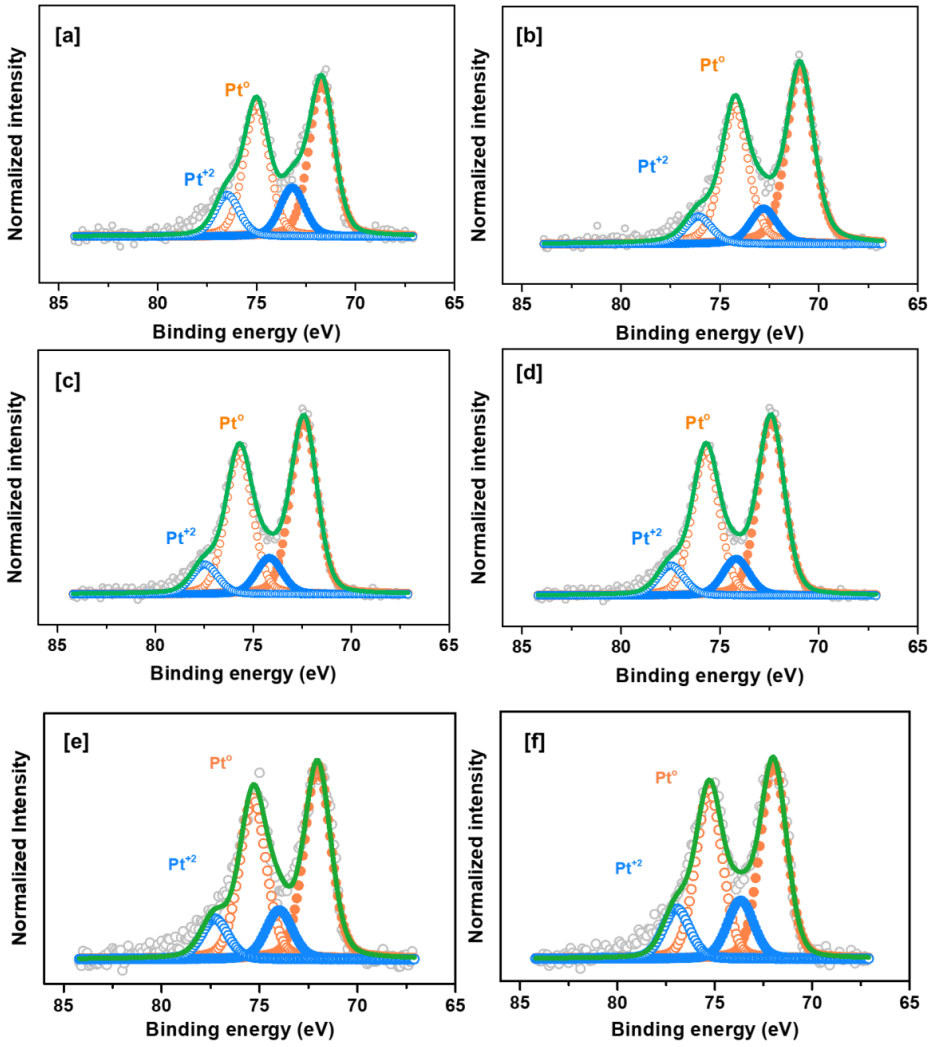

Figure S 6. XPS high resolution Pt 4f spectra of [a] Pt CNF-HT [b] Pt N-CNF [c] PtMn CNF-HT [d] PtMn N-CNF catalysts after reduction ex situ.[e] Spent PtMn CNF-HT and [f] Spent PtMn N-CNF catalysts after APR.

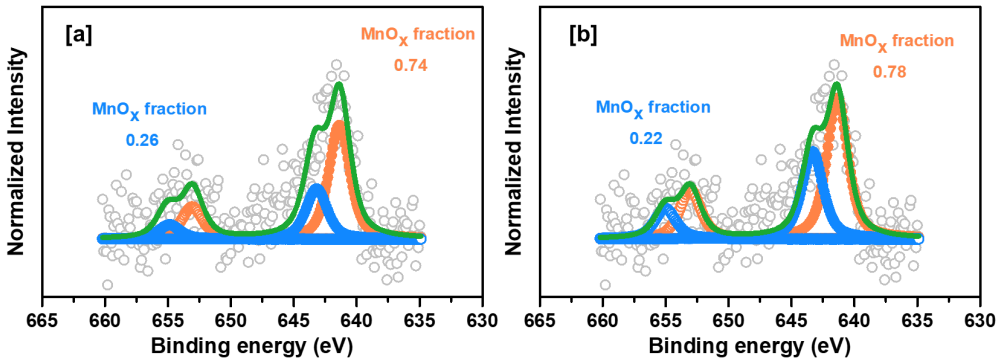

Figure S 7. XPS high resolution Mn $2p_{3/2}$ spectra of [a] PtMn CNF-HT [b] PtMn N-CNF

Table S 5. APR of ethylene glycol (6%wt) at 225°C and 20bar initial pressure for 2h at batch conditions. The carbon balance was confirmed to a degree of 88-100% for all measurements.

Catalyst	Conversion (±1.5%)	H_2 Site time yield (± 1.7 min^{-1})	Carbon Yield to liquid (±0.8%)	Gas phase selectivity (Carbon-based, %)			
				H_2 (±2.5%)	CO (±0.01%)	CO_2 (±0.5%)	Alkanes (±0.2%)
Pt CNF-ox	11.9	12.5	4.3	89.2	0.3	93.8	5.9
Pt CNF-HT	15.5	10.3	5.8	76.9	3.2	94.7	2.1
Pt N-CNF	9.7	11.2	5.7	96.7	1.0	96.3	2.7
PtMn CNF-ox	13.3	13.5	6.2	83.4	0.3	94.9	4.8
PtMn CNF-HT	14.0	13.7	5.0	72.2	2.7	96.0	1.3
PtMn N-CNF	19.0	22.0	6.7	85.8	1.4	95.2	3.4

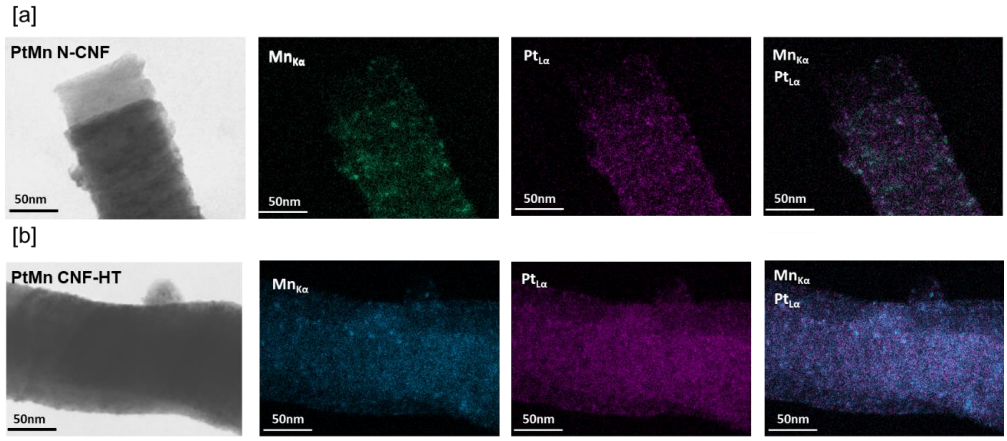

Figure S 8. STEM images and EDX elemental maps of the reduced samples; (A) PtMn N-CNF and (B) PtMn CNF-HT. EDX-maps of Mn (edge Kα), Pt (edge Lα) and the overlay of both element signals.

Weisz-Prater criterion (Φ_{WP})

The Weisz-Prater criterion (Φ_{WP}) was calculated to confirm the absence of internal mass-transfer limitations [2].

$$\Phi_{WP} = \frac{r_{obs}\rho_{cat}{r_p}^2}{C_s D_e} \quad (1)$$

The criterion is dependent on the reaction order. For zero order reaction the modulus should be below six ($\Phi_{WP} < 6$) and for first order reaction $\Phi_{WP} < 1$. For APR of ethylene glycol, the reaction order has been estimated below 1 [3]. The worst-case scenario was selected in terms of particle size, reactant concentration and reaction rate. The radius of the catalyst particle was selected from the largest sieve fraction ($r_p = 0.0125cm$). The catalyst density was estimated according to the platinum loading and density of commercial CNF ($\rho_{cat} = 3.94\ g/cm^3$). The surface feed concentration is considered to be equal to the bulk concentration ($C_s = 9.7x10^{-4}\ mol/cm^3$).

For the effective diffusion coefficient $D_e[cm^2/s]$ estimation (Equation 2), the ratio between porosity (ξ) and tortuosity (χ) was assumed to be 0.1) and the Wilke-Chang expression [4] (Equation 3) was used for the calculation of the diffusion coefficient $D\ [cm^2/s]$

$$D_e = D\frac{\xi}{\chi} \quad (2)$$

$$D = 2.98\ x\ 10^{-7}{V_A}^{-0.5473}{\eta_w}^{-1.026}T \quad (3)$$

The molar volume of ethylene glycol at normal boiling temperature was estimated by the Tyn-Calus relation $V_A = 70.04\ cm^3/mol$ [5,6] and the water dynamic viscosity at APR conditions is estimated to be 0.1188 cP [7]. In the limiting case for the highest reaction rate ($r_{obs}\ [mol/s.g_{cat}]$) Φ_{WP} was estimated to 0.29, confirming the absence of intraparticle mass-transfer limitations.

Table S 6. Continuous flow APR of ethylene glycol (6%wt) at 225°C, 30 bar and WHSV=2h^{-1}. Carbon-based gas phase selectivity evaluated at 20h of time on stream (TOS)

Catalyst	Conversion (%)	Carbon Yield (%)		Gas phase selectivity (Carbon-based, %)			
		Gas products	Liquid products	H_2	CO	CO_2	Alkanes
Pt CNF-HT	27.0	18.5	3.5	87.2	0.3	97.1	2.6
Pt N-CNF	28.5	20.2	4.4	86.3	0.3	98.4	1.3
PtMn CNF-HT	31.3	21.5	4.1	85.8	0.4	96.6	3.0
PtMn N-CNF	39.6	27.5	5.3	96.5	0.4	98.3	1.3

Table S 7. Metal leaching of the spent catalyst after continuous flow APR of ethylene glycol (6%wt) at 225°C, 30 bar and WHSV=2 h^{-1} obtained by MP-AES.

Catalyst	Metal leaching (%)	
	Pt (± 0.1%)	**Mn (**± 0.1%)
Pt CNF-HT	0.0	-
Pt N-CNF	0.0	-
PtMn CNF-HT	0.0	97.1
PtMn N-CNF	0.0	89.0

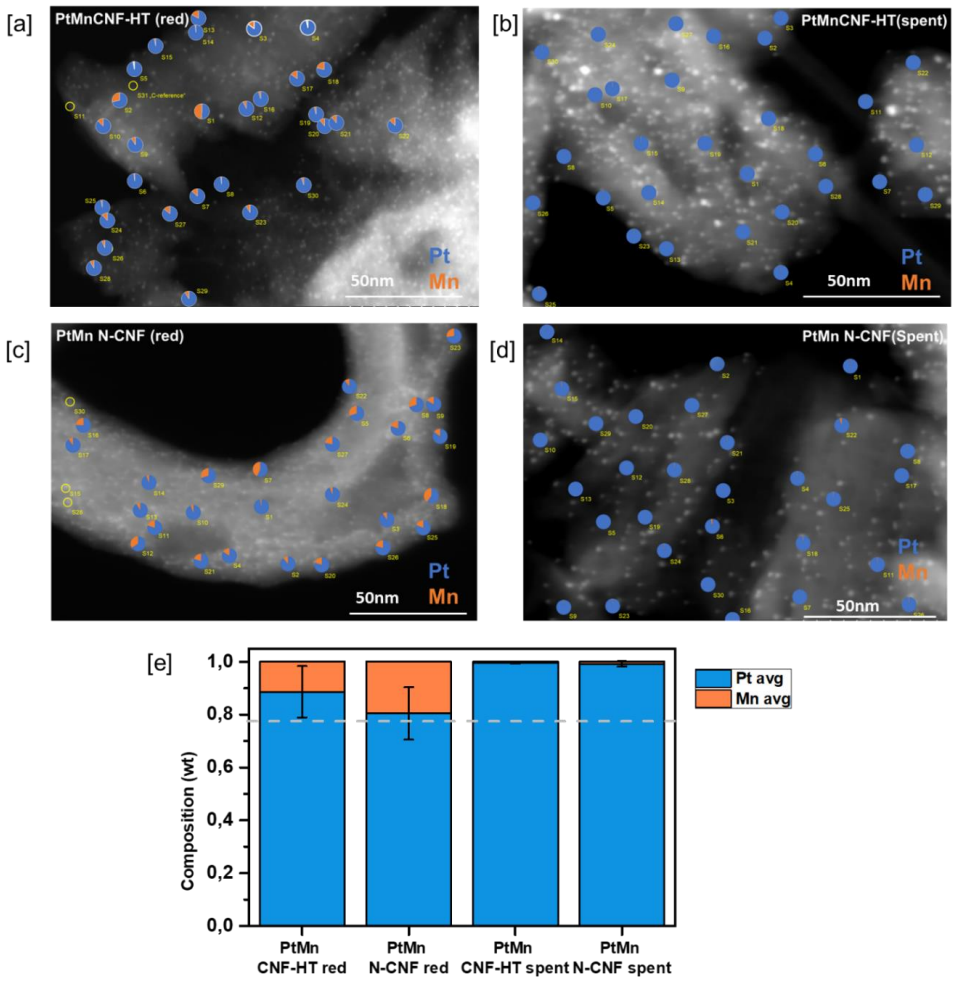

Figure S 9. STEM-EDX analysis of the Pt and Mn weight fractions of individual metal nanoparticles [a] PtMn CNF-HT reduced [b] PtMn CNF-HT spent [c] PtMn N-CNF reduced [d] PtMn N-CNF spent. [e] Average distribution of the weight fraction of Pt and Mn in the metal particles on the catalysts before and after APR, as determined by STEM-EDX analysis of 30 metal particles. The horizontal dashed line represents the theoretical weight fraction of Pt (0.78) assuming a 1:1 Pt:Mn molar ratio which was targeted during catalyst synthesis.

References

[1] J.F. Moulder, J. Chastain, Handbook of X-Ray Photoelectron Spectroscopy: A Reference Book of Standard Spectra for Identification and Interpretation of XPS Data, Physical Electronics Division, Perkin-Elmer Corporation, 1992.

[2] P.B. Weisz, C.D. Prater, in: W.G. Frankenburg, V.I. Komarewsky, E.K. Rideal (Eds.), Adv. Catal., Academic Press, 1954, pp. 143–196.
[3] S. Kandoi, J. Greeley, D. Simonetti, J. Shabaker, J.A. Dumesic, M. Mavrikakis, J. Phys. Chem. C 115 (2011) 961–971.
[4] C.R. Wilke, P. Chang, AIChE J. 1 (1955) 264–270.
[5] J.P.S. Aniceto, B. Zêzere, C.M. Silva, Materials 14 (2021) 542.
[6] M. Tyn, W. Calus, Processing 21 (1975) 16–17.
[7] L.I. Godina, A.V. Kirilin, A.V. Tokarev, I.L. Simakova, D.Y. Murzin, Ind. Eng. Chem. Res. 57 (2018) 2050–2067.

Appendix B: Paper II

Aqueous phase reforming over platinum catalysts on doped carbon supports: Exploring platinum-heteroatom interactions

Manuscript in preparation.

This paper is not yet published and is therefore not included.

Appendix C: Paper III

Bimetallic interactions stabilising Pt-Ni/TiO2 catalysts in aqueous phase reforming of ethylene glycol

Manuscript in preparation.

This paper is not yet published and is therefore not included.

ISBN 978-82-326-7502-9 (printed ver.)
ISBN 978-82-326-7501-2 (electronic ver.)
ISSN 1503-8181 (printed ver.)
ISSN 2703-8084 (online ver.)

NTNU

Norwegian University of
Science and Technology